UNIVERSITY OF SOUTHAMPTON

Understanding and modelling the formation, growth, and failure of woody debris jams at bridge piers

by

Diego Panici

A thesis submitted in partial fulfillment for the
degree of Doctor of Philosophy

in the
Faculty of Engineering and Physical Sciences
Civil, Maritime and Environmental Engineering and Science Unit

18th October 2019

UNIVERSITY OF SOUTHAMPTON

ABSTRACT

FACULTY OF ENGINEERING AND PHYSICAL SCIENCES
CIVIL, MARITIME AND ENVIRONMENTAL ENGINEERING AND SCIENCE UNIT

Doctor of Philosophy

by Diego Panici

The accumulation of large wood debris at bridge piers obstructs the flow, producing increased upstream water levels, large horizontal structural loadings, and exacerbated scour. These effects have frequently been held responsible for the failure of a large number of bridges around the world, as well as for increased risk of flooding of adjacent areas. Yet, little is known about the formation and growth of these debris piles. This thesis is aimed at deciphering the whole life of debris accumulations through an exhaustive set of 732 experiments in which debris elements were individually introduced into a flume and accumulated at a pier model downstream. In all experiments the growth of debris accumulations was observed to stop at a critical stage, after which the jam is removed from the pier by the flow. This condition typically coincides with the time when the dimensions of the accumulations are maxima. The values of the jam maximum size display a clear dependence on flow characteristics and debris length distribution, whilst other variables (such as pier diameter, debris diameter, debris density, water depth, pier shape) have shown much weaker effects. For a given debris length, accumulations are wide, shallow, and long at low flow velocities but become narrower, deeper, and shorter with increasing velocities. A comparison of accumulations formed with debris of uniform and non-uniform size distributions has revealed that the former can be up to 2.5 times wider than the latter. The effect of the shape of debris pieces was also studied by using cylindrical dowels, unbranched sticks and single-branched sticks. The maximum size of debris piles formed by idealised cylindrical debris is smaller than that of jams formed by natural wood of irregular shape. Experiments with branched debris resulted in jams significantly smaller and less stable than those with non-branched sticks. On the base of the experimental results, a mechanistic theoretical model of idealised jam geometry and a reduced set of dynamic actions was developed through conservation of angular momentum. The resulting system of ODEs was studied in the phase plane, which revealed that the failure of the accumulation depends on both planar asymmetry and ratio between the length of the jam and the extension downstream of the pier, defined as tail. The former is necessary for any jam to fail, and higher asymmetries lead to less stable jams; the latter provides stability for large tails and small lengths, but yields instability when the ratio is reduced. Results from this thesis will pave the way for practical applications in bridge engineering and flood risk assessments, and inform future research about debris jams at bridge piers.

Contents

List of Figures

List of Tables

Nomenclature

B	Width of the channel
C_{Dd}	Coefficient of drag of the debris accumulation
d	Diameter of individual debris elements
D	Pier diameter
Fr	Froude number
Fr_L	Debris Froude number
g	acceleration of gravity
h	Water depth
H	Height of the debris jam
H^c	Height of the debris jam at the critical phase
K	Length of the debris jam
K^c	Length of the debris jam at the critical phase
L	Length of individual debris elements
Re	Reynolds number
S	Bridge span length
v	Cross-section averaged velocity
W	Width of the debris jam
W^c	Width of the debris jam at the critical phase
W_{max}	Maximum value between W_R and W_L
W_{min}	Minimum value between W_R and W_L
W_L	Semi-width of the debris jam on the left of the pier
W_R	Semi-width of the debris jam on the right of the pier
α	Ratio between W and K
β	Ratio between K and ΔK
ΔK	Tail of the jam
η	Dimensionless height of the debris jam
η^c	Dimensionless height of the debris jam at the critical phase
θ	Angle of rotation of the debris jam
κ	Dimensionless length of the debris jam
κ^c	Dimensionless length of the debris jam at the critical phase
μ	Dynamic viscosity of water
ρ	Water density

ρ_L	Density of debris elements
σ	Span capacity factor
ϕ	Asymmetry factor based on the ratio W_L/W_R
ψ	Asymmetry factor based on the ratio W_{max}/W_{min}
ω	Dimensionless width of the debris jam
ω^c	Dimensionless width of the debris jam at the critical phase

Declaration of Authorship

I, Diego Panici, declare that this thesis and the work presented in it are my own and has been generated by me as the result of my own original research.

Understanding and modelling the formation, growth, and failure of woody debris jams at bridge piers.

I confirm that:

1. This work was done wholly or mainly while in candidature for a research degree at this University;
2. Where any part of this thesis has previously been submitted for a degree or any other qualification at this University or any other institution, this has been clearly stated;
3. Where I have consulted the published work of others, this is always clearly attributed;
4. Where I have quoted from the work of others, the source is always given. With the exception of such quotations, this thesis is entirely my own work;
5. I have acknowledged all main sources of help;
6. Where the thesis is based on work done by myself jointly with others, I have made clear exactly what was done by others and what I have contributed myself;
7. Parts of this work have been published as: Panici and de Almeida (2017), Panici and de Almeida (2018), and Panici and de Almeida (2019).

Signed: .....

Date: 18th October 2019

Acknowledgements

This thesis and the papers that have been published (or on the way for publication) have been the result of a long journey started several years ago. My first and biggest acknowledgement goes to my supervisor, Gustavo, who guided me through many difficult situations over the years and gave me advice for many situations, although he never put any pressure on me that was exceeding my possibilities. I feel myself to be extremely lucky and grateful for this opportunity and if I can think about my future as a researcher a big part of it is thanks to him. A sincere acknowledgement goes to Prof. Paul Kemp and the people involved with the CDT in Sustainable Infrastructure Systems. Without them, I could have not carried out this doctorate, and their support (both administrative and logistical) has always been outstanding. Another big thanks is necessary for the staff in the hydraulics laboratory, Toru and Karl. Without their material help and advice I would have not been able to carry out such a large number of experiments and with all these instruments. Thanks also to the students who helped me out during these years, Fiona, Pierre, Matthew, Adam, Matthew, Alex, Marco. Last, but not least, this research would have not been possible without the financial help of the EPSRC, which funded this doctoral study through the grant EP/L01582X/1.

I am also grateful to all the other people who have been on my side during the years of my doctorate: my parents Ambra and Antonio, my sisters Chiara and Elisa, my grandma Amalia, and my little niece Giulia, for which I had the honour and blessing to be her Godfather. It has been a long and hard journey, many things happened over the time of this doctorate. Some people left, whilst some other people arrived in my life and have helped to make it a wonderful adventure. I am happy of all the good moments and I have learnt a lesson from the least good. This PhD has not only been a degree, but also forged the person I am today, and I will always be grateful for that.

Et ostendit mihi fluvium aquae vitae splendidum tamquam crystallum, procedentem de throno Dei et Agni.

Chapter 1

Introduction

1.1 Background

The intricate interplay between bridges and rivers has long been a challenge to scientists and engineers. The complexity of the problem, as well as the dramatic effects often observed, have encouraged researchers to pursue an in-depth understanding about the multiple issues that this interaction entails. Bridge piers in rivers alter the flow field, inducing increased upstream water levels (frequently referred to as afflux) and affect the flood risk of the adjacent areas. Flooding are among the most costly and damaging hazard to the human society, with 5 million people exposed to this risk only in England (Environment Agency, 2009) and flooding-related costs forecast to dramatically increase in the next decades (Sayers et al., 2016). Furthermore, bridge piers cause localised scour and hydraulic loadings, which together can be responsible of pier displacement and potentially leading to bridge collapse.

The aforementioned effects can be dramatically exacerbated when a pier is affected by the accumulation of large wood debris (LWD). In a river (especially during flooding events) numerous fallen trees, branches and trunks are recruited and mobilised by different mechanisms (Sedell et al., 1988; Diehl, 1997). Debris elements are then conveyed along the channel until being entrapped by a pier, which initiates a build-up process (Manners et al., 2007; Lagasse et al., 2010). The upshot of this process is the formation of an LWD jam, which obstructs a significant portion of the flow area and induces a substantial afflux (Diehl, 1997; Lagasse et al., 2010; Benn, 2013). Woody debris jams have also historically been a primary cause of bridge failure (e.g. Charles' Bridge in Prague in Czech Republic during the 1890 flooding event shown in Figure 1.1), although this phenomenon still frequently occurs in contemporary ages. For example, it is estimated that more than 30% of bridge failures in the United States are correlated to woody debris jams (Diehl, 1997) while similar numbers are found in the UK (Benn, 2013).

1.2 Motivation

Research about dynamics and effects of debris accumulations at bridge piers is still in its infancy. Most of the existing knowledge about debris jams is based on in-situ individual observations (e.g. Diehl, 1997; Lyn et al., 2007; Lagasse et al., 2010). A few experimental studies attempted to describe LWD effects on flow and scour, although showing important limitations about the understanding of woody debris jams formation (e.g. use of idealised or arbitrary accumulation shape and size), which resulted in inaccurate findings. In addition, current bridge design guidelines (e.g. Diehl, 1997; Da Deppo et al., 2004) are often ambiguous and do not consistently include adequate methodologies in order to account for debris jams. As a result, accurate approaches to estimate the size of LWD jams are yet to be included into standard engineering practice. Developing predictive models for woody debris accumulations could provide a substantially more robust approach towards flood risk assessment and bridge design than currently available.

This work is aimed at bridging the gap between debris formation phenomena and engineering

FIGURE 1.1: Charles' Bridge failure occurred during 1890 flooding. Source: Museum of Prague.

applications, providing a detailed analysis of the LWD accumulation process. Experimental and theoretical analysis are developed together with the tools for predicting the main characteristics of debris jams in a broad range of conditions. The application of the findings of this project will be highly beneficial for river and structural engineering practice, since it will provide a solid knowledge on how to estimate the risk of debris-related hazards, as well as a robust understanding to inform the design of debris resilient infrastructures.

1.3 Aims and Objectives

Existing knowledge about LWD jams formation processes is inadequate to assess the crucial role played by these accumulations in the bridge-river interactions with regards to flooding and bridge failure. The overarching aim of this study is to investigate the processes responsible for the formation and growth of woody debris jams and to develop a reliable model for engineering design purposes. The detailed aims of this study are:

- To analyse the process of woody debris jams growth through experimental analysis, identifying relevant trends and general patterns.
- To evaluate and quantify the potential maximum size that a jam can achieve under given conditions of flow and wood supplied.
- To develop a predictive functional relationship that can be used to estimate afflux and pier loadings, as well as to inform next generation scour experiments.
- To develop a theoretical mechanistic model describing key processes of the woody debris accumulation phenomenon.

1.4 Thesis Outline

This chapter has introduced the relevance of woody debris jams at bridge piers, the thesis motivation and the proposed aims and objectives. The remaining chapters of the thesis are structured as follows:

- Chapter 2 provides an in-depth analysis on the current knowledge about the large wood debris accumulations at bridge piers. At first, mechanisms that are responsible for recruitment and transport of the debris are identified. Then, previous studies of LWD entrapment and growth (either conceptualised or based on different problems) are examined, identifying possible biases and knowledge gaps. Finally, an overview of the effects of debris jams on local scour and flow field is presented.

- Chapter 3 describes the methodology that has been adopted for the experimental work of this study. Here a dimensional analysis is performed, which introduces the main variables supposedly affecting woody debris accumulations. This paves the way for the development of a functional relationship among the different dimensionless groups defined by the analysis. This is followed by the description of the experimental procedure along with the facilities and measurement equipment used.

- Chapter 4 contains all the experimental results and corresponding analysis. Results show a qualitative time-growth description of different phases of these jams. In addition, the maximum jam size is presented as a function of flow conditions, debris, and pier characteristics. Based on experimental observations, a regression analysis is then proposed.

- Chapter 5 proposes a theoretical/mechanistic model inspired by the experimental observations. The model of the jam failure is proposed and approached as a stability analysis problem. A system of ordinary differential equations (ODE) based on conservation of angular momentum is developed, which is then analysed in the phase plane. This analysis is used to propose a theoretical explanation to the failure of debris accumulations observed in all experiments.

- Chapter 6 provides an overview of the main findings provided in this thesis.

- Chapter 7 discusses the limitations encountered in this thesis and provides insights for further research.

Chapter 2

Literature Review

2.1 Large Wood in Rivers

Large Wood Debris (LWD), Coarse Wood Debris (CWD), drift or large wood are some of the names typically used to describe fallen trees, trunks and large branches that are found within riverine areas and undergo processes of transport and deposition. This material is believed to provide beneficial effects on fish and micro organisms stabilisation (Gregory et al., 1993; Abbe and Montgomery, 1996; Gippel et al., 1996b; Gurnell et al., 2002; Lagasse et al., 2010). Furthermore, in the last decades woody debris have often been reintroduced in streams for flood management and channel stability purposes (Gurnell et al., 2002), with the aim to positively influence river geomorphology (Gregory et al., 1993; Gurnell et al., 2002). As a result, interest around woody debris is high with multiple applications, even though the vast majority of debris-related knowledge is based on biological and geomorphological studies.

2.1.1 Properties of Large Wood

The characteristics of LWD in rivers (e.g. amount, size, density) are the result of a natural process that depends on several factors, mostly the characteristics of upstream forested areas (Diehl, 1997; Lagasse et al., 2010) and fluvial processes (Gurnell et al., 2002). For example, the botanical features of the tree population affects the size of large wood, especially those in floodplains and riparian forests, since LWD recruitment typically occurs in these areas (Sheeder and Johnson, 2008; Lagasse et al., 2010; Lucía et al., 2015). On the other hand, debris size and shape can be influenced by the river in which they are conveyed (Pfister et al., 2013). Gradient, discharge, and channel geometry may affect the debris features for a given reach (Diehl, 1997; Bradley et al., 2005), as the processes of transport and deposition can alter the characteristics of the debris elements, e.g. by breaking them into smaller pieces.

Wood pieces with diameter $\geq$10 cm and length $\geq$1 m are generally classified as Large Wood Debris (Gippel et al., 1996a; Máčka et al., 2011), even though alternative definitions can be found in the literature. Smaller wood pieces can be categorised as Small Wood Debris (SWD) (Manners et al., 2007). Another classification according to Bradley et al. (2005) defines debris *small* when formed by limbs or sticks, *medium* when debris are tree limbs or large sticks and *large* when these are proper trees or logs, yet it is not clear how to correctly quantify the difference between two classes. Therefore, the first definition is generally widely more accepted.

Debris transported by rivers may display highly variable diameters (Máčka et al., 2011), irregular density and shape (Sedell et al., 1988; Lagasse et al., 2010; Máčka et al., 2011). Additionally, LWD frequently include rootstock (especially if originated from bank erosion), branches, and leaves (Diehl, 1997; Lagasse et al., 2010) resulting in highly irregular shapes (Diehl, 1997; Lassettre and Kondolf, 2012). Figure 2.1 shows a sketch of a debris trunk with some of the variables that can be observed. For practical purposes, LWD have previously been typically idealised as regular cylinders, simplifying the log geometry to its two main variables: length and diameter.

Debris diameters are seldom constant and perfect circular cross-sections in trunks are rarely observed, resulting in a difficult definition for a representative measure of the trunk diameter (Máčka et al., 2011). The total length of a debris element is given by either an entire tree fallen into the channel or part of it breaking into smaller pieces (Lagasse et al., 2010). Diehl (1997) proposed a model in which the maximum expected debris length in a river is given by the smallest value between: *a.* the smallest width of the channel upstream of a point in the river (e.g. the cross-section highlighted in Figure 2.2), *b.* the maximum length of sturdy logs, *c.* 9 m plus one quarter of the upstream width. Although this model is based on intensive field observations, the approach shows some limitations. At first, point *a.* is true only if trees are transported normal to the flow direction and in a straight reach of the channel, but this is in contrast with Diehl's (1997) own observations that debris typically travel on the water surface in correspondence of the thalweg and parallel to the flow. This point is also criticised by Lagasse et al. (2010), since

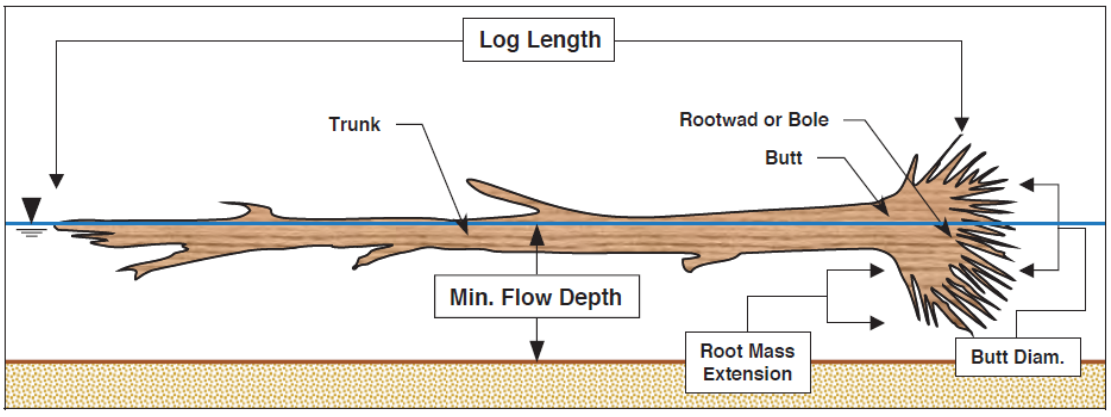

FIGURE 2.1: Sketch of an LWD in a river and its characteristics. Source: Lagasse et al. (2010).

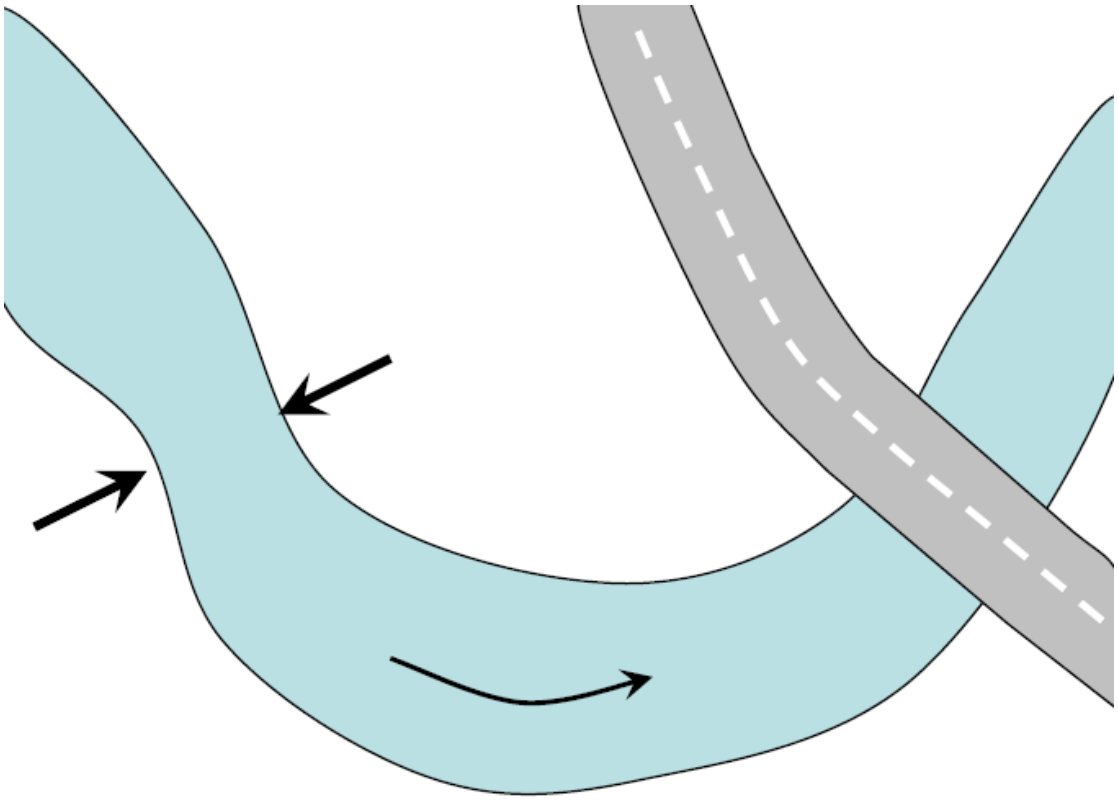

FIGURE 2.2: Narrowest cross-section in a river reach upstream of a bridge. Source: Bradley et al. (2005).

pieces larger than the narrowest cross-section were found in numerous North-American rivers. Furthermore, Diehl's (1997) point *c.* is foremost applicable to US rivers, while in other geographical areas trees characteristics might be substantially different (e.g. Central Europe and Great Britain (Linstead and Gurnell, 1999; Máčka et al., 2011)).

The distribution of the size of debris elements in rivers may be highly varied (Pfister et al., 2013), although most debris are significantly smaller than the largest tree that can be introduced in a river reach (Lyn et al., 2003; Blersch and Kangas, 2014). The large majority of debris size distributions is typically non-normally distributed (Gippel et al., 1996a; Blersch and Kangas, 2014). The frequency of occurrences is highest for small debris pieces, whereas with increasing size the number of debris observed declines. Therefore, a high amount of debris belongs to a lower-mid class of sizes. This general trend can be observed in numerous situations, despite the fact that each river has a peculiar distribution depending on the characteristics of the forested area, such as forests that are pristine or harvested, old-growth or young-growth (Sedell et al., 1988). Several site observations in North-America (Sedell et al., 1988; Hess, 2007; Cadol and Wohl, 2010), Europe (Van Sickle and Gregory, 1990; MacVicar and Piégay, 2012; Lucía et al., 2015; De Cicco et al., 2016) and Central America (Cadol and Wohl, 2010) indicated that the highest number of observations of woody debris is for those pieces of length typically between 10% and 20% of the longest elements.

2.1.2 Recruitment

Woody debris can be recruited by the flow through multiple mechanisms. Previous studies suggested that the principal processes of LWD introduction in river channels are bank erosion (Diehl, 1997; Lyn et al., 2003) and banks mass-wasting, accounting for a 73% of the total wood load (Lagasse et al., 2010). Other phenomena causing trees to fall are: dead plants, logging, windthrow, collapse from ice or snow, and mass soil movement (Sedell et al., 1988; Diehl, 1997; Gurnell et al., 2002; Sheeder and Johnson, 2008; Lagasse et al., 2010; Pfister et al., 2013). Sedell et al. (1988) performed intensive in-situ surveys during flood events, observing that debris recruitment is the highest under these conditions. This also corresponds to the moment when bank erosion is maximum, indirectly confirming the main recruitment process, although floodplain flow during flood events may also be sufficient to mobilise trees that have fallen over time. Therefore, trees location and position on the banks is of primary importance for debris recruiting. Almost all debris are originated by riparian forests (Sheeder and Johnson, 2008; Lagasse et al., 2010) and floodplains (Lucía et al., 2015) closest to the river. Robison and Beschta (1990); Lagasse et al. (2010) proposed a conceptualised model (although supporting evidence is not provided) sketched in Figure 2.3 for elements recruited through bank erosion, in which the probability of a tree falling into the stream is proportional to the ratio between the arch of the projected tree height over the channel (i.e. the *AD* arc in Figure 2.3) and the total circle originated by the tree height (i.e. $2\pi H_e$).

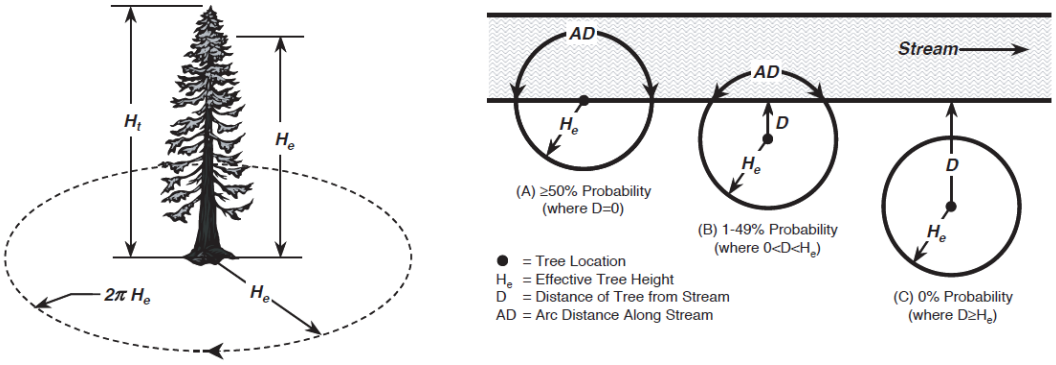

FIGURE 2.3: Sketch of catchment area for a tree falling into a channel. Source: Lagasse et al. (2010).

On the other hand, debris already fallen and lying on the floodplains or deposited on the channel bed during low-flow conditions (Sheeder and Johnson, 2008) are subject to a period of dormancy, until favourable conditions arise and a high concentrated transport develops (Sedell et al., 1988; Lyn et al., 2007). These conditions are achieved when stage begins to rise and debris are mobilised by flotation (Diehl, 1997; Lagasse et al., 2010) and drag force (Braudrick and Grant, 2000; Crosato et al., 2013) against friction, which tends to prevent debris mobilisation (Braudrick and Grant, 2000)[1]. Other factors that affect LWD mobilisation are the orientation of

[1] Although buoyancy can be perpendicular to friction and drag, friction force depends on the resultant force normal to the channel bed, which includes buoyancy.

debris pieces (Braudrick and Grant, 2000; Wilcox and Wohl, 2006; Lagasse et al., 2010; Crosato et al., 2013) and debris length and diameter (Braudrick and Grant, 2000; Curran, 2010; Lagasse et al., 2010; Crosato et al., 2013) as these determine the amount of surface exposed to the flow (hence, the drag force applied).

2.1.3 Transport

Floating debris are transported approximately at the same velocity of the current on the surface (Bradley et al., 2005; Sheeder and Johnson, 2008), parallel to the flow direction (Diehl, 1997). Debris are usually observed within a small portion of the channel (Diehl, 1997; Bradley et al., 2005; Sheeder and Johnson, 2008), which often coincides with the point on the water surface where the depth is highest (Lyn et al., 2003; Sheeder and Johnson, 2008). In addition, transport of debris elements in these channel portions are likely to occur again at similar flow conditions (Sheeder and Johnson, 2008). Reasons for this well-marked debris pattern are still unknown. Diehl (1997), followed by Bradley et al. (2005); Lagasse et al. (2010), hypothesised that debris position is driven by secondary currents (i.e. the velocity cells formed by velocity components normal to the streamwise direction) to the points of convergence on the water surface. Figure 2.4 displays the velocity cells and the convergence points, that are the centreline (in a straight reach) and close to the outer bank (in a channel bend). A few experiments appeared to confirm a preferential pattern for both straight channel (Bocchiola et al., 2006) and curved reach (Schmocker and Weitbrecht, 2013). Nonetheless, there is no direct evidence confirming Diehl's (1997) theory.

The transport of LWD elements has been conceptually classified in three different modes according to Braudrick et al. (1997):

- **Uncongested transport** Debris are free to move along the channel, interactions among debris are null or very limited. Single elements can rotate or roll independently;
- **Congested transport** Bursts of woody debris are moving as a single mass, with very limited individual movements;
- **Semi-congested transport** An intermediate condition between congested and uncongested.

Field studies revealed that transport of large masses are rare, whereas a high number of debris is conveyed as individual element (Bradley et al., 2005; Lyn et al., 2007; Sheeder and Johnson, 2008; Lagasse et al., 2010), therefore suggesting that the *uncongested transport* is the predominant process (Lyn et al., 2003). Moreover, turbulence or strikes with obstacles can easily break debris clusters (Lagasse et al., 2010), resulting in a generally short-lived *congested transport*.

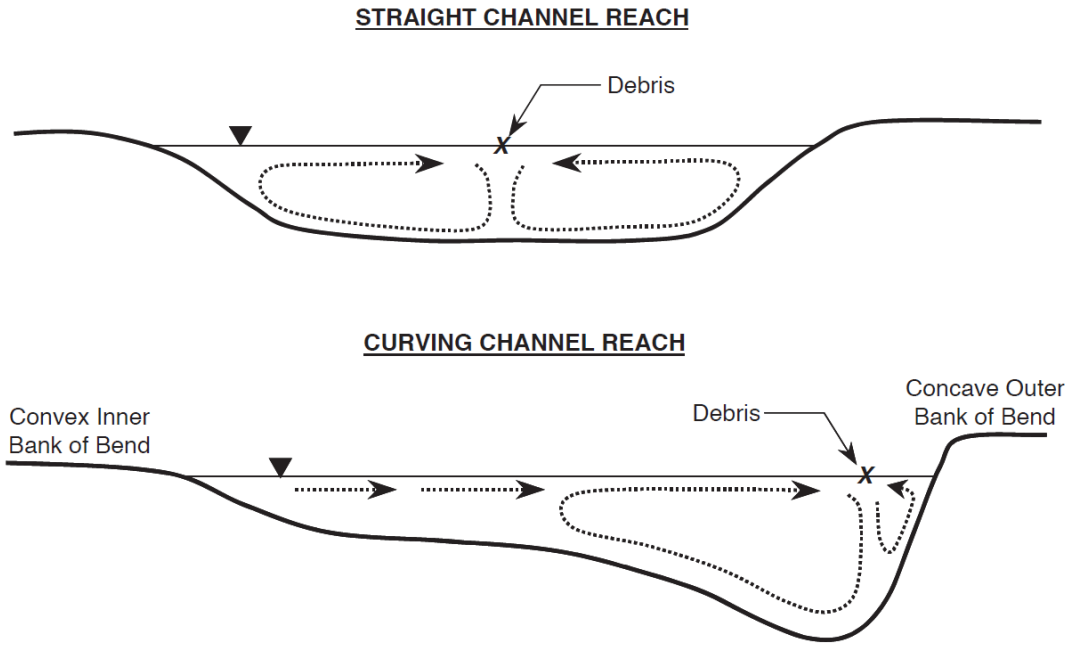

FIGURE 2.4: Conceptual model for debris patterns due to secondary cells according to Diehl (1997). Source: Lagasse et al. (2010).

2.2 Debris Accumulations

Large wood accumulations begin when elements get trapped at an obstacle (e.g. a sandbar or a pier) or are deposited during low flow conditions, which then initiate a self-assembly process. The understanding of these phenomena is key for the development of predictive models for the formation of a debris jam at a bridge pier.

2.2.1 Initiation of Accumulations by Debris Entrapment

The accumulation of woody debris jams at a bridge pier typically begins when one or more debris elements hit the upstream nose of the pier and remains entrapped. Several factors may affect this debris recruitment.

The location of the pier and alignment to the flow affect the debris likelihood of entrapment (Diehl, 1997; Bradley et al., 2005; Sheeder and Johnson, 2008). From a simplistic theoretical consideration, a stable anchoring is possible when the point of contact between a debris element and an obstacle is close to the centroid of the area normal to flow of the former, preventing any torque from destabilising the debris piece (Bocchiola et al., 2006). When this does not occur, a debris element hits the pier and then is immediately removed (or trapped for a short period and then escaped) (Lyn et al., 2003).

The shape of a pier nose has also been cited as an additional important factor (Diehl, 1997; Lagasse et al., 2010; De Cicco et al., 2016). Diehl (1997) suggested that round-nose piers offer the lowest likelihood of debris entrapment, although there was no evidence in support of this observation. A recent laboratory experiment by De Cicco et al. (2016) investigated the role of different pier shapes in retaining woody debris. Results showed that differences in the probability of entrapment were minimal among different shapes except for flat sections (e.g. square or rectangular), which are more prone to entrap debris. It is also important to note that these experiments were performed under a limited range of flow conditions and influenced by other unaccounted external factors (e.g. the lateral walls of the 300 mm-wide flume), providing only preliminary insights into the problem.

Debris characteristics and imperfections (e.g. roughness, attached branches) are believed to substantially contribute in increasing the probability of entrapment (Lyn et al., 2003). Although little research has been carried out about bridge piers, it has been previously observed that branches and root-wads dramatically influence interaction with other structures (Abbe and Montgomery, 2003; Schmocker and Hager, 2011; Pfister et al., 2013). For instance, Schmocker and Hager (2011) experimentally reproduced a flooding event in Switzerland, testing small trunks (branched and unbranched) interacting with a bridge deck. As expected, branched trunks were more prone to be anchored at the bridge deck. Similarly, Pfister et al. (2013) performed a series of experiments on the probability of obstruction of piano-key weirs by instream wood and concluded that branched logs had a higher probability in clogging these structures. These experiments based on bridge decks or weirs would indicate that a similar outcome could be expected for bridge piers and should be further investigated.

Flow velocity also plays a fundamental role for the likelihood of debris entrapment. Bocchiola et al. (2008) experimentally studied the motion of debris elements (modelled using cylindrical dowels) through an array of 156 randomly distributed static vertical rods. Results showed that the debris entrapment likelihood at these obstacles decreases with increasing the debris Froude number (i.e. a Froude number in which the debris diameter is its characteristic length). This result is not surprising, as Fr increases with velocity and consequently augmenting the drag force (which quadratically depends on velocity) applied to the debris.

2.2.2 Growth of Accumulations by Self-Assembly of Debris Pieces

The self-assembly process of woody debris begins after that some elements get anchored at the pier. This initial raft that forms at the pier then recruits more pieces and significantly widens the potential trapping area of the obstruction, which leads to further accumulation. Figure 2.5 displays (in plan view) a conceptualised debris pile growth according to Lagasse et al. (2010). In general, debris accumulations (whether at a bridge pier or not) supposedly begin by the entrapment of a key-element, i.e. a large and stable log (Diehl, 1997; Bradley et al., 2005; Lagasse

et al., 2010). The key-element then recruits smaller elements, sometimes classified as *racked*, according to Abbe and Montgomery's (2003) notation, forming a framework of medium/large size debris (Manners and Doyle, 2008). Nevertheless, this conceptualised process would seem too idealised, since any debris could get trapped by an obstacle (and then a larger incoming piece may get trapped at a later stage). On the other hand, the entrapment likelihood increases with the debris length (Bocchiola et al., 2008). Therefore, this suggests that it is more likely that an accumulation is initiated by a large or key element rather than a small debris piece, although the latter cannot be ruled out.

A few studies suggested that the debris pile formation starts at the water surface and then grows downwards (Bradley et al., 2005; Lagasse et al., 2010). As the jam growth progresses, the formed framework is able to entrap finer debris (i.e. *loose* elements) and even non-woody debris (Parola et al., 2000; Lagasse et al., 2010; Lassettre and Kondolf, 2012). Manners and Doyle (2008) proposed a conceptualised model of the formation of woody debris jams in rivers based on three in-situ surveys. In this model, a jam formation is supposedly initiated by a key-element trapped by obstacles or lateral banks. Then, a *framework* phase develops, in which other pieces are recruited and the total volume of debris and the drag force exerted on the jam increases at a fast pace. Finally, the *accumulation* and *complete jam* phases (characterised by modest or no changes) define the final features of a jam (e.g. size, porosity) which can last indefinitely. However, this model does not explain whether this configuration is definitive or other changes may occur and is not consistent with other site observations. For instance, some 'chronic' (i.e. long-lasting) accumulations can be observed in rivers (Diehl, 1997; Lyn et al., 2007), although their growth is not a continuous process (Lyn et al., 2007) and may occur ahead of a flood peak (Lyn et al., 2003). Lyn et al. (2007) carried out a series of site surveys to study the evolution of LWD accumulations at the same sites between different flow conditions. The study revealed that drift piles grew or receded between two observations even if no flooding events occurred. It was also noted that a few accumulations disappeared at some point, and in one case the authors proposed that the debris jam could have been disengaged from the pier and then transported and accumulated again downstream at another bridge pier.

Mature (i.e. at a relatively stable phase) LWD accumulations observed in field studies form shapes that are typically comparable to an inverted half-cone (Diehl, 1997; Lagasse et al., 2010) or a pointing arrow (Abbe and Montgomery, 1996), in which the maximum height is at the pier close to the riverbed and the maximum width is at the pier on the water surface (Diehl, 1997). Nonetheless, some other (less frequent) shapes/configurations (e.g. rectangular) were also observed in natural environments (Lagasse et al., 2010).

Diehl (1997) suggested (based on field observations) that in wide channels and with large span bridges the length of the key-element corresponds to the maximum width of a debris accumulation, supposedly supporting the jam against adverse forces (Lagasse et al., 2010). Scarce

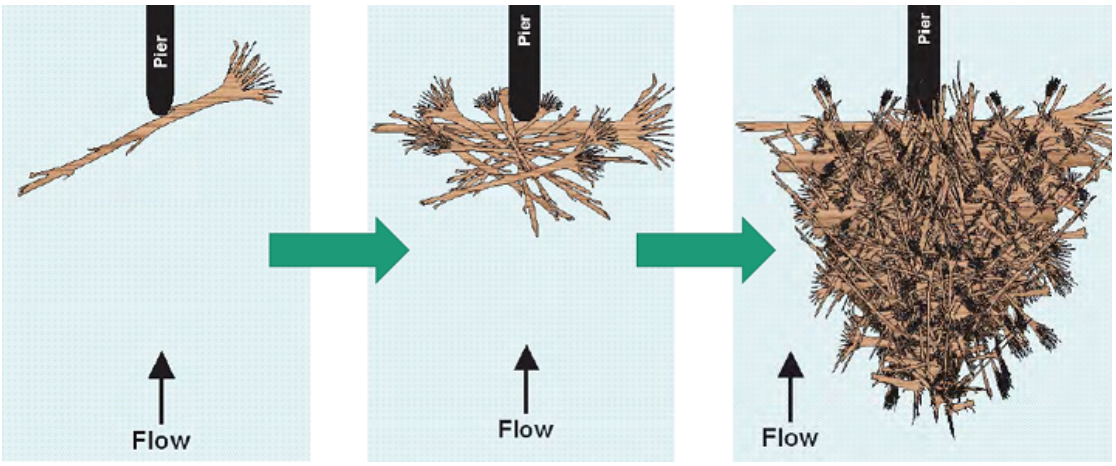

FIGURE 2.5: Sketch of typical accumulation accretion process on a plan view. The process is initiated by a key-element, then built-up by racked members and finally filled by loose pieces. Adapted from Lagasse et al. (2010).

frequency of long debris with respect to the key members can explain this predominant role assumed by key-elements. Short bridge spans or a small river section could lead to a more severe blocking. When this happens, a bridging effect takes place (Diehl, 1997) leading to large, wide and stable accumulations. This bridging effect can also be observed when jams at two adjacent piers are joined together. Figure 2.6 shows a typical example in which a large accumulation was formed by bridging two or more adjacent accumulations. Regarding the vertical dimension, only the riverbed could limit an accumulation growth (Diehl, 1997) and this may occur mainly during recession of a flood, i.e. with descending water level. When the riverbed is reached, the degree of freedom of the jam is limited (Bradley et al., 2005; Lagasse et al., 2010) and could stabilise the debris pile (Lyn et al., 2003), promoting further accumulation (Lagasse et al., 2010), although this is yet to be confirmed. Another factor influencing the self-assembly of jams is believed to be flow velocity. Lyn et al. (2003) experimentally studied at laboratory scale the effects of flow velocity on debris jams. They observed that at low velocities LWD accumulations are wide and also that water depth played a negligible role in the jam growth process. On the other hand, at increasing velocities debris piles become narrower and influenced by water depth. In fact, at low depths but high velocities the formed jams were interacting with the channel bed, while this was not observed when depths were sufficiently high to avoid any interaction. This can be reasonably explained by considering that drag force is responsible for the vertical accumulation size, as it depends on the square of velocity (Elliot et al., 2012). Nonetheless, experiments by Lyn et al. (2003) only explored a small range of flow velocities and these conclusions, albeit interesting, need to be taken with caution.

2.2.3 Effects of LWD Accumulations

Over the last decades, considerable research efforts were focused on pier-scour interactions (e.g. Dargahi, 1989; Ahmed and Rajaratnam, 1998; Johnson and King, 2003; Muzzammil et al., 2004;

FIGURE 2.6: Large LWD accumulation at the Skagit River, Washington, US, during a flood in 1995. It can be observed how blockage is caused by debris bridging two single-pier accumulations. Source: Washington State Department of Transportation.

Dey and Raikar, 2007; Melville, 2008, to cite but a few). The presence of debris accumulations around bridge piers significantly increases the complexity of the problem and poses new challenges for modelling of scour depths. While some early works attempted to model the intricate phenomena associated with LWD jams (e.g. Melville and Dongol, 1992; Parola et al., 2000; Lagasse et al., 2010; Pagliara and Carnacina, 2011b; Rusyda et al., 2014), the research is still in its infancy.

2.2.3.1 Effects of LWD on Flow

Woody debris jams interact with the flow mainly acting as an obstruction, which reduces the free-flow area (Parola et al., 2000; Daniels and Rhoads, 2004; Bradley et al., 2005; Pfister et al., 2013) and strongly influences the distribution of velocities and turbulence in the channel (Gurnell et al., 2002; Wilcox and Wohl, 2006; Manners et al., 2007). The jam size and position considerably alter the flow trajectories (Daniels and Rhoads, 2004), exacerbating flow velocity underneath and beside of the accumulation (Pagliara and Carnacina, 2013). Furthermore, a boundary layer is formed all around the jam raft, the thickness of which depends on the surface roughness (Balachandar and Patel, 2002; Pagliara and Carnacina, 2013), further contracting the flow area (Pagliara and Carnacina, 2013). Figure 2.7 from Pagliara and Carnacina's 2011b experimental study shows an example of scour and conceptual velocity field developed around an

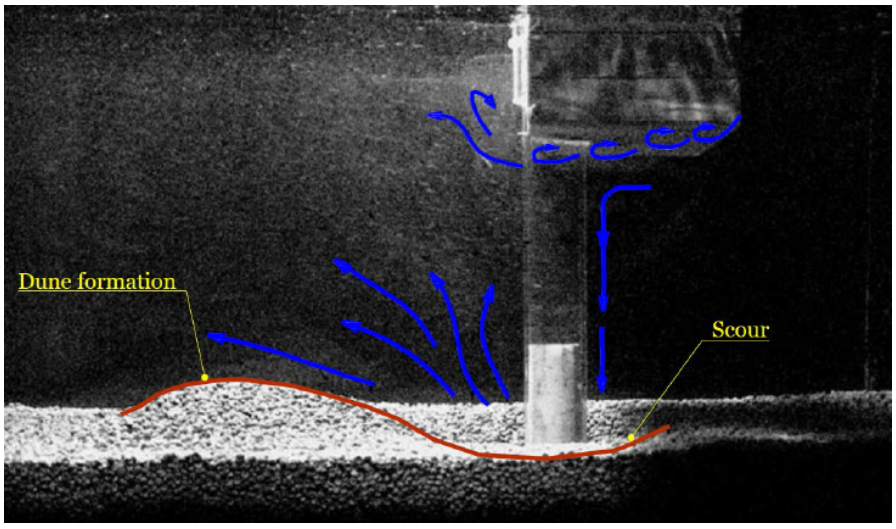

FIGURE 2.7: Velocity, scour and boundary layer separation in presence of an accumulation. Flow from right to left. Adapted from Pagliara and Carnacina (2011b).

idealised debris accumulation. The vorticity system underneath the raft was identified by the authors as the boundary layer formed by the flow-raft interaction.

Other effects on the flow field are the development of vortex structures. A body (as it is in this study a pier with the debris accumulation) immersed in a non-ideal fluid (as it is water) produces a three-dimensional detachment of the flow field. The obstruction yields an adverse pressure gradient (Tritton, 1988; Muzzammil et al., 2004) reducing the velocity of the boundary layer until it drops to almost zero. Therefore, the flow is detached from the obstruction surface and a series of large vortices is developed around the pier. Figure 2.8 by Melville (2008) shows a sketch of the vorticity system of a pier in a river (without debris). The main vortex structures are the so-called horseshoe vortices, which are quasi-periodical (Dargahi, 1989) and with little variation in their structure (Dargahi, 1990). A vertical boundary layer separation at the edge of the pier, resulting in a downstream detachment, is known as wake vortex system (the vertical vortices downstream of the pier in Figure 2.8).

The vorticity system as previously described yields a pressure drop in the wake area downstream of the pier, which results in a pressure difference between the upstream and downstream faces of the obstacle. This dynamic pressure difference is known as the drag force that is applied by the flow on the pier (and, as a reaction, by the pier on the flow). The general equation of the drag force derived through dimensional analysis is generally given as

$$F_D = \frac{1}{2}\rho C_D A v^2, \tag{2.1}$$

where ρ is water density, C_D is the drag coefficient, A is the frontal area obstructing the flow and v the approaching flow velocity relative to the object. The drag coefficient C_D is function of the Reynolds number Re, although at river-scale Re is usually high and C_D assumed independent of Reynolds number, i.e. Reynolds invariance (Wallerstein et al., 2001; Bocchiola et al.,

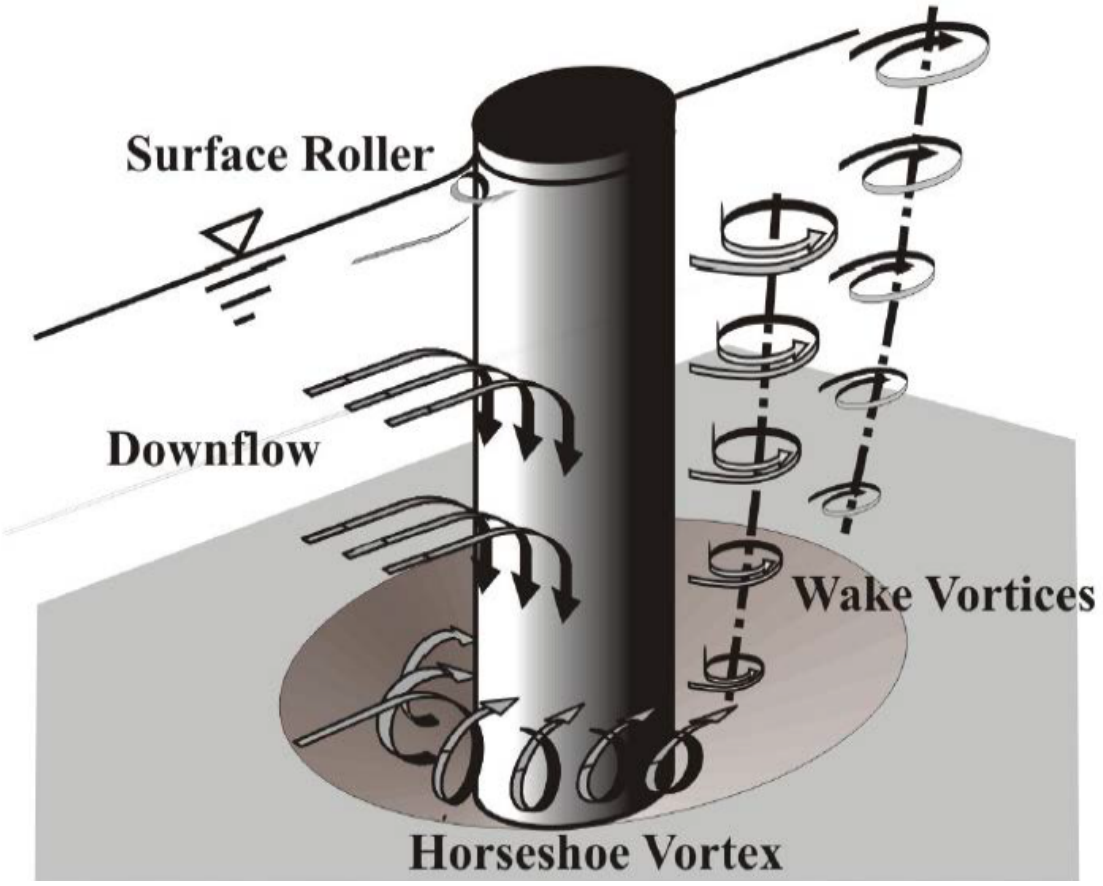

FIGURE 2.8: Sketch of a typical vorticity system at a bridge pier. Source: Melville (2008).

2008). For this particular case, the drag force also depends on many other variables such as roughness of the raft, porosity and the shape and geometry of the accumulation. Thus, correct evaluation of this coefficient should not be carried out with too idealised debris jams (Hygelund and Manga, 2003; Manners et al., 2007). Finer debris (e.g. leaves or branches) can be enmeshed in the jam, blocking a core area of the accumulation (Parola et al., 2000) and change the overall porosity. Manners et al. (2007) compared the drag force applied to several LWD accumulations lying on a river bed and showed that when these jams contain only key-elements (i.e. no *racked* and fine debris are entrapped) drag force is low, whereas in an *impervious* condition (i.e. a jam completely filled by smaller pieces) the force induced by drag is considerably higher than the first case. The LWD-induced drag force becomes an additional structural load exerted on a pier, which may contribute to bridge damage or failure if this is not accounted for during bridge design (Parola et al., 2000; Bradley et al., 2005). Since the area of a debris jam may be considerably larger than the pier alone and the LWD drag coefficient likely to exceed that of the pier, the drag force magnitude with these accumulations is likely to be several times higher than otherwise expected without the accumulation in place (Wu et al., 2014).

Another effect of the drag force is the increase in the upstream water depth (Parola et al., 2000; Bradley et al., 2005; De Cicco et al., 2016). According to basic (1D) momentum conservation

principles, the water level variation depends on the interrelationship among forces (some of which are also defined by the water depths of the control volume). Young (1991) tested at laboratory scale the effect that debris piles (although not accumulated at bridge piers) have on flood levels. The author observed that the stage height rise depends significantly on the frontal area of the debris jams. A recent study by Schalko et al. (2018) tested the accumulation of woody debris at an array of piers and correlated the upstream water rise with the Froude number and the accumulation packing. Other studies (Gippel et al., 1996a,b; Parola et al., 2000) suggested that Froude number, obstructed area, and accumulation drag coefficient are the main variables that might affect the afflux, as together they completely define the drag force F_D. Thus, since size and drag coefficient of LWD jams determine the magnitude of the drag force, they also affect the afflux. It follows that predicting obstructed area A and drag coefficient C_D is crucial for evaluating F_D and, therefore, predicting the effects on the upstream flow.

A few experimental studies attempted to estimate the drag coefficient C_D for LWD accumulations and are summarised in Table 2.1. Parola et al. (2000) performed small-scale laboratory testing using (individually) plates, wedges, and accumulated limbs to model a debris jam. The drag coefficient computed from experimental results ranged widely between 0 and 2, although showing a dependence on the flow blockage ratio (i.e. the ratio between obstructed area and channel cross-sectional area). This dependency was observed for ratios above 36%, whereas for lower values of the blockage ratio the drag coefficient was relatively unaffected. A contrasting observation was reported by Hygelund and Manga (2003), in which they reported a poor correlation (i.e. no dependency) between blockage and C_D for blockages above 30%, even though this study was based on individual debris elements rather than jams, which would limit the applicability to debris accumulations. The authors measured in-situ the torque exerted by the flow on test logs and computed the drag coefficient for each of them. Values of C_D were found within the interval 0.9 to 3.2. Another study was conducted by Manners et al. (2007) on LWD jams in rivers (but not accumulated at a pier), measuring the water depth change in a river section and back-calculating the drag coefficient under different conditions of porosity. Computed values of C_D varied from 0.7 to 9.0, even though this very large variation was acknowledged by the authors as a consequence of the poor definition of the geometry of the frontal area. It is also interesting to notice that, among these mentioned works, only Parola et al. (2000) attempted to reproduce LWD jams at piers with natural twigs and mimicking the process of jam formation, whereas other studies would likely be inaccurate for the application to debris jams at bridge piers due to the different type of jams used. Nevertheless, tests with sticks and limbs by Parola et al. (2000) are only a very small number of the data set analysed (i.e. flat plates were used in the large majority of the experiments to model jams) and tested on a reduced amount of flow conditions, which significantly limits the applicability of these results.

TABLE 2.1: Values of the drag coefficient C_D of debris accumulations from past studies.

Reference	Type of study	C_D range	Observations
Parola et al. (2000)	Experiments on debris accumulations at a pier; vertical plates, wedges, and sticks	0.1 - 1.9	C_D depends on the blockage ratio when greater than 36%
Hygelund and Manga (2003)	In-situ measurements of single logs	0.9 - 3.2	Blockage ratio affected C_D for values below 30%
Manners et al. (2007)	In-situ measurements of debris jams lying on a river channel	0.7 - 9.0	C_D dependent on the porosity of the jam. Poor definition of the frontal area.

2.2.3.2 Scour

Localised scour around bridge piers is a phenomenon driven by the flow field modification induced by the obstruction. Vortices originated by a pier (Figure 2.8) cause a scour hole around the pier. With accumulated woody debris, this effect is exacerbated resulting in a larger scour hole (Melville and Dongol, 1992; Pagliara and Carnacina, 2010, 2011a,b). Melville and Dongol (1992) experimentally studied the debris-induced local scour using several smooth regular shapes to model the debris raft. They produced a scour design curve using the approach of the *equivalent* pier, i.e. the effective diameter of the pier necessary to produce the same scour hole without debris, based on the formulae by Melville and Sutherland (1988). This method was refined by Pagliara and Carnacina (2011a) and Pagliara and Carnacina (2011b) introducing debris characteristics, position, and accumulation size.

Obstructed area, accumulation shape, and velocity are the most important factors affecting local scour at a bridge pier (Lagasse et al., 2010; Pagliara and Carnacina, 2011b). On the other hand, LWD roughness and porosity were observed having second-order effects (Lagasse et al., 2010). Nevertheless, this contrasts with Pagliara and Carnacina's (2011b) findings, which indicate that surface roughness (but not porosity) accounts for a notable effect on the overall scour (i.e. coarser accumulations may cause larger scours).

2.3 Current Guidelines for Modelling Size, Transport, and Effects of Debris Jams and Applications

Guidelines currently available for modelling debris jams at bridge piers are mostly based on site surveys or experiments. There are also some computational models that have been developed in recent years aimed at replicating the mechanics of the accumulation process. Nevertheless, none of these studies was aimed at investigating the dimensions and shape that a jam could produce, substantially limiting their applicability to bridge design and flood risk assessment purposes.

2.3.1 Experiments

Experiments have been an important tool for understanding the phenomenon of woody debris accumulation. Most experimental studies were focused on scour. Melville and Dongol (1992) were among the first to study effects of woody debris on scour at bridge piers. In their experiments, the authors modelled debris accumulations by the use of regular shapes (e.g. cylinders, cones) installed at the pier. Lagasse et al. (2010) conducted similar experiments, but instead used rectangular shapes and wedges with protrusions in the attempt to mimic the inherent irregularities of debris jams. Pagliara and Carnacina (2010, 2011a,b, 2013) followed the approach by Melville and Dongol (1992) and modelled LWD piles through a solid cuboid or natural sticks bound together forming a prismatic shape, an example of which is shown in Figure 2.9. These studies provided interesting insights about the effects that a debris jams may cause to local scour, but their findings may not be accurate. Models of debris accumulations used in these experiments were often idealised, arbitrarily designed, and unlikely to represent shape and size of a real-world LWD jam. Furthermore, these idealised models were adopted irrespectively of the actual jam formation process or intervening variables (e.g. debris size and flow velocity, as suggested by several aforementioned studies). For instance, although flow conditions were varied between experiments, the jam model remained the same. This contrasts with Lyn et al. (2003), who indicated that the size of large wood piles depends on velocity. More importantly, shape and dimensions of these accumulation models were chosen arbitrarily, even though they are likely to be among the most important factors affecting the scour process. The ability to predict shape and size of the accumulations would improve the accuracy of the scour analysis, being consistent with the jams that could be expected at a bridge pier for given conditions.

Other experiments were aimed at investigating the formation process of woody debris accumulations under different conditions, although typically very limited in the number of variables studied (e.g. flow conditions, size of debris), and in the ability to accurately reproduce the full-scale phenomenon. Lyn et al. (2003) studied how velocity and water depth influence the formation of debris jams at bridge pier (although with a limited debris supply and a small number of flow conditions) using twigs and dowels. They concluded that natural sticks or twigs should be preferred to wooden dowels when modelling debris jams due to the primary role played by the

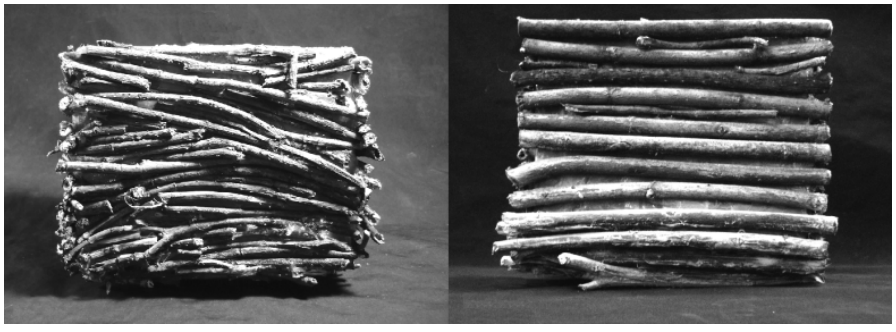

FIGURE 2.9: Drift model used by Pagliara and Carnacina (2013).

inherent irregularities of full-scale debris elements. Rusyda et al. (2014) experimentally analysed accumulations at two Japanese bridges (with and without pier) by instantaneously releasing a large bundle (the number of elements per bundle ranged from 50 to 800) of debris (modelled by dowels) into a 0.3 m-wide flume. The authors proposed a relationship for estimating the volume of a debris jam based on the experimental data. Nevertheless, the large amount of debris pieces released contrasts with previous studies about debris transport, that is unlikely to occur in large bundles (Braudrick and Grant, 2000; Lyn et al., 2003). A recent study by Gschnitzer et al. (2017) tested probability of LWD clogging at bridge decks and bridge piers in a 0.60 m-wide flume. The authors used wooden dowels as debris elements, the length of which ranged between 40% to 120% of the flume width. A similar approach has been used by De Cicco et al. (2016). The authors tested the effects of several pier shapes on the probability of debris entrapment in a 0.30 m-wide flume modelled by dowels of different lengths. The narrow and small flumes used for all of these experiments led to unavoidable interactions with the flume walls, whereby introduced an additional (and unwanted) variable to the problem that was not accounted for. Thus, any conclusions from these studies are likely to be inaccurate, or not representative of a pier that is far from both river banks. Moreover, these flumes could not generally allow a broad range of flow conditions (e.g. Rusyda et al., 2014; De Cicco et al., 2016), limiting the observation of (as will be shown later in the results section) one of the most important factor in the woody debris accumulation process. Another critical limitation is represented by the use of wooden dowels in order to model debris elements, despite this practice has been discouraged (Lyn et al., 2003) due to the poor representation of dowels for real-world LWD.

2.3.2 Engineering Guidelines and Computational Models

Current engineering guidelines regarding size and shape of LWD jams at piers are still lacking a systematic approach. Some of the proposed design jams are contradictory or not informed by robust observations (Diehl, 1997). For instance, Figure 2.10 displays two contrasting bridge design guidelines. Australian design practice recommends a 20 m-wide and 1.2 m-deep rectangular debris raft, while in New Zealand the shape is suggested triangular and 15 m-wide and 3 m-deep (Diehl, 1997). Similarly to the Australian model, Da Deppo et al. (2004) suggested to adopt a rectangular debris accumulation with the purpose of evaluating local scour but not advising about the size to be used. Despite these guidelines attempted to provide a basic approach to the accumulations of woody debris, they seem to lack any underpinning science or observation (either theoretical or empirical) and were proposed not including key-factors such as debris or flow characteristics. Extensive surveys revealed that the size of models proposed for both Australia and New Zealand were frequently exceeded by observed jams (Diehl, 1997; Lagasse et al., 2010).

A few hydraulic computational models for flood modelling including debris supply and formation of debris rafts have been produced in the last few years. In these models, the inclusion of

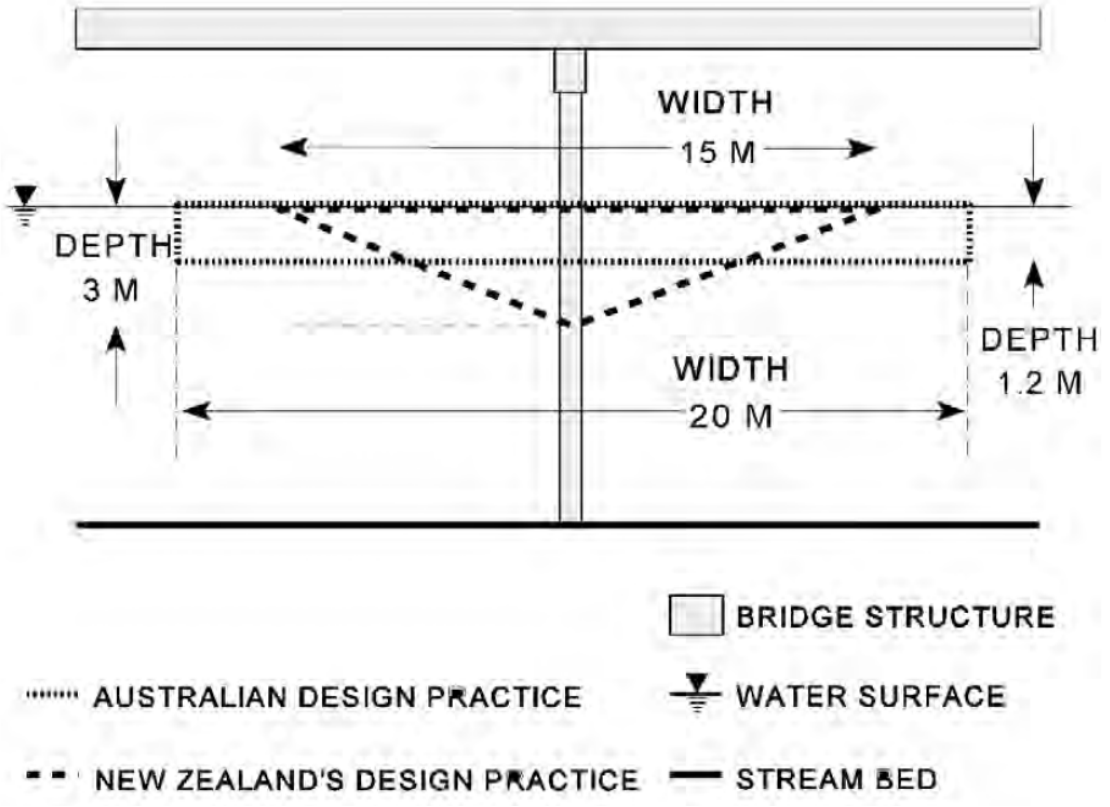

FIGURE 2.10: Australia and New Zealand recommended design practice for woody debris accumulations. Source: Diehl (1997)

incipient motion and transport of debris elements was typically modelled through a balance of forces between friction, drag and debris weight (Stockstill et al., 2009; Ruiz-Villanueva et al., 2013, 2014). LWD are simulated by floating cylinders and their motion include rotation and translation (Stockstill et al., 2009; Ruiz-Villanueva et al., 2014). Ruiz-Villanueva et al. (2014) developed a flood model to simulate a 1997 flash-flood event on a Spanish river subject to a high transport of LWD, which were included in the modelling. The output of this model is a two-dimensional planar raft, i.e. the vertical component of the LWD jams is not included. This represents a considerable limiting factor, since the obstructing area will not have a vertical growth, unlike real-world accumulations. A flood model by Elliot et al. (2012) also takes into account the additional drag force applied to structures due to debris accumulations. This model does not include the LWD build-up process, instead places obstructions at the piers based on in-situ observations. Given that the process of transport and accumulation of debris depends strongly on a complex 3D fluid-debris-pier interaction, it is unlikely that simple hydraulic models will be able to produce meaningful predictions.

Parola et al. (2000) tried to estimate afflux from woody debris obstructions using the wide-spread 1-D river hydraulics software HEC-RAS. They reduced the free flow area with obstructions in correspondence of bridge structures. Although the software is particularly reliable for many

hydraulic processes, a problem of this complexity might require a different approach that is not an oversimplification.

2.4 Summary

The crucial interplay between bridges and rivers have long been a concern for scientists and engineers. Bridge piers alter the flow field, induce structural loads as well as local scour and can restrict the free flow area, rising the upstream water levels. If a large wood debris accumulation occurs at a pier, the aforementioned effect can significantly increase, representing a serious threat to the bridge structural stability and exacerbating upstream water level rise. The latter could be theoretically modelled through momentum conservation principles. Approaching water velocity and accumulation frontal area perpendicular to the flow (as well as the drag coefficient) may allow the correct estimation of the drag force magnitude. Thus, ability to predict both debris size and drag coefficient is of primary importance for the estimation of debris-related effects.

Although woody debris accumulations at piers are recognised to be responsible of numerous bridge failures and increased flooding levels, little research has been carried out to unveil the potential size that these jams could reach. In-situ surveys, as well as experimental studies, did not clearly identify the formation process, jams potential size, and effects on the flow. On the other hand, there is a general agreement from site observations on the typical semi-conical shape achieved by forming piles. Jams are also believed to be initiated by a *key-element* which entraps further smaller pieces and initiates a build-up process. However, the exact formation process is still unknown and ability to predict LWD accumulations size is lacking.

A few experimental studies attempted to describe the accumulation phenomenon, but were limited in detail and scope. For example, model accumulations were far from the actual configurations and not consistent with real jams. Furthermore, the knowledge gap regarding the understanding of the LWD accumulation phenomenon influences the current guidelines about bridge design and flood risk assessment. Indications are often arbitrary or non-empirically based and the methods suggested (e.g. using simplified 1-D equations to model LWD obstructions) are too basic to correctly simulate the actual effects on the stream.

Chapter 3

Methodology

This chapter illustrates the methodology that has been employed to perform the experimental analysis described in the next chapter. At first, a dimensional analysis is carried out. This is followed by a detailed description of experimental facilities, set-up, and variables adopted in this study. Finally, a description of the approach employed for data analysis is provided.

3.1 Dimensional Analysis

Dimensional analysis was performed with the aim of defining a functional relationship between the significant dimensionless variables affecting the accumulation process. Furthermore, dimensional analysis ensures similarity between laboratory and prototype (i.e. real-world) scale. This occurs when ratios between forces are the same for both model and prototype, i.e. a dynamic similarity is established.

The following functional relationship between fluid, flow and debris variables is proposed:

$$f\left(\rho, \mu, v, h, g, D, L, d, \rho_L, B, W, H, K\right) = 0, \tag{3.1}$$

where ρ is the water density, μ is the dynamic viscosity of water, v is the streamwise component of cross-section averaged velocity approaching the LWD jam (prior to the formation of the accumulation), h is the water depth, g is the acceleration due to gravity, D is the diameter of the pier, L and d are respectively the length and diameter of individual debris elements, ρ_L is the debris density, B is the width of the flume, and W, H, and K are respectively width, height, and length of the debris accumulation (as illustrated in Figure 3.1). As two variables W and K are used to describe the planar geometry, the jam shape is not restricted to a semi-circular cone. Table 3.1 summarises variables and dimensions studied.

TABLE 3.1: Variables studied for dimensional analysis. Dimensions are: M for mass, L for length and T for time.

Quantity	Symbol	Dimensions
Water density	ρ	ML^{-3}
Dynamic viscosity	μ	$MT^{-1}L^{-1}$
Water velocity	v	LT^{-1}
Water depth	h	L
Gravity acceleration	g	LT^{-2}
Pier diameter	D	L
Debris length	L	L
Debris diameter	d	L
Debris density	ρ_L	ML^{-3}
Channel width	B	L
Accumulation width	W	L
Accumulation height	H	L
Accumulation length	K	L

Equation (3.1) can then be rearranged in a more compact and dimensionless form by applying Buckingham π-theorem. The theorem states that an equation with n physical variables can be rewritten as a dimensionless equation with $n - k$ variables, where k is the number of fundamental physical quantities. These variables (as a group) must contain all fundamental physical quantities, that for standard fluid mechanics are mass M, length L, and time T. The dimensionless groups resulting from the product between these variables are the so-known π-groups. For the problem of woody debris accumulations, ρ, v, and L have been chosen as the repeating variables yielding the following functional relationship between ten dimensionless variables:

$$g\left(Re_L, Fr_L, \frac{h}{L}, \frac{L}{D}, \frac{d}{L}, \frac{\rho_L}{\rho}, \frac{B}{L}, \omega, \eta, \kappa\right) = 0, \tag{3.2}$$

where Re_L=$\frac{\rho v L}{\mu}$ and Fr_L=$\frac{v}{\sqrt{gL}}$ are respectively the debris Reynolds and debris Froude numbers (i.e. using L as the characteristic length), $\frac{L}{D}$ is the dimensionless length of individual debris elements with respect to the pier size, d/L is the size ratio between a debris diameter and length, h/L is the dimensionless ratio of water depth and debris length, and ω=$\frac{W}{L}$, η=$\frac{H}{L}$, and κ=$\frac{K}{L}$ are the three dimensionless variables used to describe the geometry of the accumulation.

The relationship in (3.2) can be simplified with a few assumptions. In fully turbulent flows, effects of the Reynolds number are usually neglected under the assumption of Reynolds invariance (Wallerstein et al., 2001; Bocchiola et al., 2008; Heller, 2011, 2017), so that Re_L is dropped from (3.2), resulting in:

$$g\left(Fr_L, \frac{L}{D}, \frac{d}{L}, \frac{h}{L}, \frac{\rho_L}{\rho}, \frac{B}{L}, \omega, \eta, \kappa\right) = 0. \tag{3.3}$$

The functional relationship (3.3) relates the three variables characterising the geometry of a debris jam (ω, η, κ) to variables that describe the characteristics of both flow and individual debris

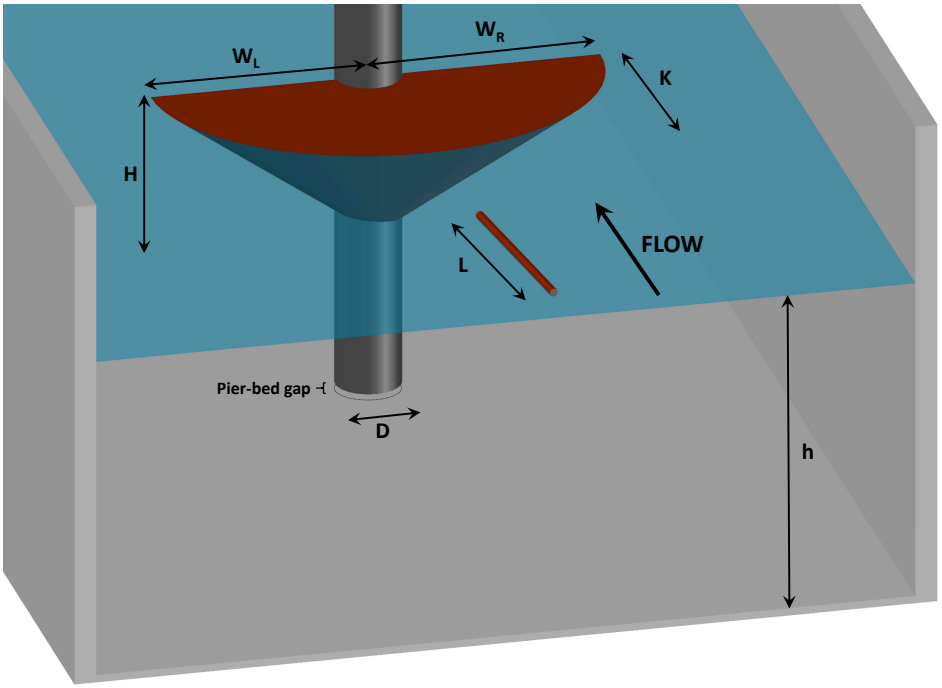

FIGURE 3.1: Idealised 3-d view of a debris jam with indication of geometrical and flow characteristics involved.

elements. Thus, any attempt to describe a jam size, whether theoretically or experimentally, should take into account the relationship found in (3.3).

A further analysis about other possible dimensionless group combinations is proposed in Appendix A.

3.2 Experiments

An extensive experimental campaign was planned in order to thoroughly understand the process of formation and growth of debris jams. The experiments were aimed at:

i Analysing the process of woody debris accumulations throughout their growth and formation;

ii Evaluating the maximum size that debris jams can form during their lifetime;

iii Analysing the effect of the intervening variables in (3.3) on the formation process and maximum size;

iv Comparing accumulations obtained by uniform size debris (i.e. with constant length and diameter) with those resulting from non-uniformly distributed size (in length) debris;

v Evaluating the importance of debris shape comparing wooden dowels with natural non-branched sticks and the effects of branches on accumulations.

Table 3.2 summarises all the experiments carried out in this thesis and then categorised in different groups. For each group, Fr_L was varied in the widest possible range for available values of velocity v and debris length L and identifies the number of experiments conducted. These groups were sorted according to each individual factor analysed for the debris jams:

- Groups U analysed the ratio L/D for different values of both L and D;
- Groups D analysed the ratio d/L for different values of d and keeping L constant;
- Groups H analysed the ratio h/L for different values of h and keeping L constant;
- Groups T analysed the ratio ρ_L/ρ for different values of ρ_L;
- Groups N analysed the ratio L/D for different values of both L and D with non-uniform length elements;
- Group R repeatedly analysed an experiment under same conditions;
- Groups B analysed the effects of debris shape;
- Groups P analysed the effects of pier shape.

A detailed description for each group is provided in the following sections. In total, 732 experiments were conducted.

3.2.1 Experimental Facilities and Instruments

Experiments were carried out at the internal flume located at the Hydraulic Laboratory of the University of Southampton Science Park in Chilworth, Southampton. The tilting flume has a rectangular cross-section, glass-walled, and is 22 m-long and 1.375 m-wide. Figure 3.2 shows a picture of the Chilworth internal flume. The width of the flume ensured that interactions between debris rafts and the walls were minimal, preventing unwanted effects that likely influenced some previous studies (e.g. Rusyda et al., 2014; De Cicco et al., 2016). Water was pumped from a sump located underneath the flume by three pumps with capacity of delivering discharges from 0.08 m^3/s up to 0.42 m^3/s. The nominal power of these pumps is 22.4 kW for pump 1 and 11.2 kW for both pump 2 and 3, for a total nominal power of 44.8 kW. Flow discharge delivered to the flume was controlled by three valves (one for each pump) as shown in Figure 3.3. Flow depths at the pier section were controlled by a flap gate installed at the downstream end of the flume.

TABLE 3.2: Summary of all experiments carried out.

Group	L (mm)	d (mm)	D (mm)	h range (mm)	Number of experiments	Fr range	Fr_L range
U1	375.0	11.85	100	282 - 461	18	0.16 - 0.43	0.14 - 0.43
U2	250.0	11.85	50	296 - 395	21	0.13 - 0.42	0.14 - 0.51
U3	312.5	11.85	50	296 - 396	21	0.13 - 0.42	0.12 - 0.47
U4	375.0	11.85	50	260 - 394	19	0.15 - 0.43	0.12 - 0.43
U5	375.0	11.85	25	282 - 420	18	0.16 - 0.44	0.14 - 0.43
D1	375.0	7.64	50	285 - 377	21	0.14 - 0.51	0.13 - 0.48
D2	375.0	9.65	50	285 - 377	21	0.14 - 0.52	0.13 - 0.48
D3	375.0	14.85	50	285 - 377	21	0.14 - 0.51	0.13 - 0.47
D4	375.0	17.85	50	286 - 377	21	0.14 - 0.51	0.13 - 0.48
D5	375.0	21.59	50	286 - 377	21	0.14 - 0.51	0.13 - 0.48
D6	375.0	29.26	50	295 - 394	21	0.13 - 0.42	0.12 - 0.42
H1	375.0	11.85	50	290 - 299	20	0.13 - 0.46	0.12 - 0.41
H2	375.0	11.85	50	366 - 373	21	0.12 - 0.43	0.11 - 0.43
H3	375.0	11.85	50	442 - 454	17	0.10 - 0.32	0.11 - 0.35
T1	375.0	11.85	50	288 - 377	21	0.14 - 0.51	0.12 - 0.41
T2	375.0	11.85	50	288 - 377	21	0.14 - 0.52	0.11 - 0.43
N1	500.0	11.37	100	268 - 402	17	0.16 - 0.42	0.11 - 0.35
N2	625.0	11.38	100	268 - 407	18	0.16 - 0.43	0.10 - 0.33
N3	375.0	10.86	50	268 - 412	15	0.15 - 0.42	0.13 - 0.40
N4	437.5	10.65	50	268 - 409	16	0.15 - 0.42	0.12 - 0.38
N5	500.0	11.37	50	275 - 408	18	0.15 - 0.43	0.11 - 0.37
N6	562.5	11.40	50	277 - 405	18	0.15 - 0.44	0.11 - 0.35
N7	625.0	11.38	50	274 - 408	18	0.15 - 0.43	0.10 - 0.33
N8	687.5	11.65	50	271 - 405	17	0.15 - 0.43	0.09 - 0.32
N9	750.0	11.35	50	271 - 405	18	0.15 - 0.44	0.09 - 0.30
N10	437.5	10.65	25	274 - 400	16	0.16 - 0.43	0.13 - 0.37
N11	500.0	11.37	25	274 - 401	18	0.16 - 0.44	0.12 - 0.38
N12	625.0	11.38	25	274 - 409	18	0.16 - 0.44	0.10 - 0.34
N13	750.0	11.35	25	274 - 402	18	0.15 - 0.42	0.09 - 0.30
R1	687.5	11.65	50	355 - 365	22	0.23 - 0.24	0.17 - 0.18
B1	375.0	12.00	50	269 - 393	19	0.14 - 0.40	0.14 - 0.39
B2	375.0	11.85	50	261 - 395	19	0.15 - 0.43	0.12 - 0.43
B3	375.0	11.85	50	261 - 396	19	0.15 - 0.43	0.12 - 0.43
P1	375.0	11.85	50	279 - 412	21	0.13 - 0.42	0.11 - 0.42
P2	375.0	11.85	50	305 - 395	21	0.13 - 0.42	0.11 - 0.43
P3	375.0	11.85	50	299 - 381	21	0.13 - 0.43	0.12 - 0.43
P4	375.0	11.85	50	306 - 392	21	0.13 - 0.42	0.12 - 0.43
P5	375.0	11.85	50	304 - 379	21	0.13 - 0.42	0.12 - 0.42

FIGURE 3.2: Side view of Chilworth internal flume at the University of Southampton Science Park.

Instruments and equipment used were carefully selected in order to provide a high level of measurements accuracy. An Acoustic Doppler Velocimeter (ADV) SonTek IQ® Plus was used to measure the average cross-section flow velocity and was placed on the bottom of the flume. Figure 3.4 shows the IQ Plus structure and position of probes. This ADV generates three acoustic beams upstream (two skewed 60° off vertical and horizontal axis and one 25° off vertical axis along the centre axis of the channel) and one downstream (skewed 25° off vertical axis along the centre axis of the channel). The results for each beam are provided in up to 100 cells (depending on flow depth) as small as 2 cm in diameter. An upward-looking beam measures the flow level in tandem with a pressure sensor and the resulting water surface is combined with the averaged cross-section velocity to give the discharge. The nominal accuracy of the instrument is $\pm 1\%$ of measured mean-profile velocity (Fulford and Kimball, 2015). Prior to the experimental campaign, velocity was measured at 36 points evenly distributed in 4 rows and 9 columns along a cross-section for three different flow conditions by a Nortek Vectrino ADV. The measured data was used to estimate the accuracy of the average velocity measured by the IQ. A systematic difference between the two instruments was on average 2.8%, indicating that the IQ could be considered a reliable instrument for measuring average flow discharge in these experiments.

The total load applied to the pier was measured by attaching a load cell onto the top of the pier, which was not touching the flume bed. A Thames Side T66 (50 kg capacity) cell was used, with maximum error of $\pm 0.017\%$ of the capacity. Sampling frequency was 10 Hz and recorded data was analysed by a custom LabVIEW program.

FIGURE 3.3: Regulation valves for the Chilworth Internal flume. Top to bottom: pump 1, pump 3, pump 2.

Continuous video recordings were performed using two cameras Logitech HD Pro Webcam C920 (1920x1080 pixels, recording at 30 fps) and an underwater camera.

Water level upstream of the pier was continuously monitored by a series of four ultrasonic sensors Senix ToughSonic® 14. The data collection frequency was 10 Hz and recorded data was acquired by a custom LabVIEW program. The nominal accuracy for these instruments is better than $\pm 0.5\%$ of the target distance, depending on temperature and environmental conditions. When the use of ultrasonics was not possible (as well as for instruments calibration) a standard point gauge was used, the accuracy of which is ± 0.2 mm.

A detailed description of instrumental calibration and methodology employed for data analysis is reported in Appendix B.

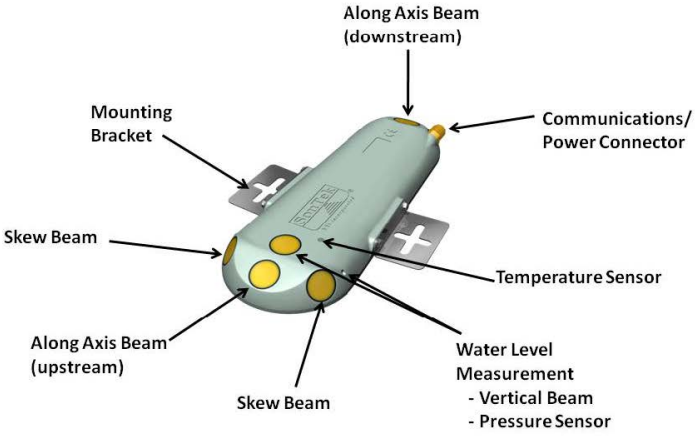

FIGURE 3.4: Drawing of the IQ Plus device indicating the main features. Figure from the SonTek IQ® user's manual.

3.2.2 Flow Conditions

The flow rates used in this study ranged between 0.08 m^3/s, that is the minimum discharge that can be delivered by one pump, to 0.42 m^3/s, that is the maximum discharge with all three pumps fully operational and valves completely opened. Within this flow range, each experimental group was tested from a minimum of 15 to a maximum of 21 flow conditions, in order to vary the debris Froude number Fr_L in intervals of approximately 0.02. The number of Fr_L conditions studied for each group corresponds to the number of tests performed in Table 3.2, except for group R1 as explained in the following section. Average flow velocities reached at the pier section varied from a minimum of 0.21 m/s to a maximum of 0.82 m/s (for test groups U, N, R, B, and P). Each experiment was performed under approximately steady flow conditions and horizontal flume. The practical reason of this last configuration was due to the tilting system being dysfunctional at the time in which the first experimental campaigns were conducted. The maximum flow velocity was extended to 0.91 m/s for test groups D, H, and T, since the tilting system was functioning for this experimental campaign, allowing increased velocities for the highest range of discharges. Water depth between experiments varied in the range of (approximately) 250 mm and 450 mm. Water depth was controlled by the downstream flap gate and (when functioning) the tilting system.

Overall, Reynolds number $Re = \rho v h/\mu$ ranged between 5.10x10^4 and 3.06x10^5 - that correspond to transitional and turbulent flow regimes, and Froude number $Fr = v/\sqrt{gh}$ ranged between 0.12 and 0.52, i.e. subcritical flow.

3.2.3 Debris

Natural sticks (twigs and branches fallen from trees) were used to model debris elements, as also previously recommended by Lyn et al. (2003) in order to represent shape irregularities commonly observed in debris found in natural environments. Sticks used for experimental purposes were collected from limbs and fallen branches (from different trees commonly found in UK and Europe, e.g. beech, oak, birch etc.) around the external compound of the Hydraulics Laboratory in Chilworth (Southampton). The same sticks were also re-used across several tests. The diameter d of all debris elements was measured at both ends using a digital calliper (accuracy ± 0.1 mm), and the average value between these two was adopted as the element diameter. For selection purposes, the sticks employed for the experiments were chosen having a distribution of diameters with a maximum coefficient of variation of 10.5%. For all experiments (except tests T1 and T2) debris dry density ρ_L was kept in the range 450-550 kg/m^3. It was also assumed that in the short travel time between the dropping point and the pier section, changes in density were negligible. Debris density was controlled for all tests by a system which dried the water absorbed from debris sticks after each experiment and monitored by spot measures of the density of debris samples. The mass of the debris sample was measured by a precision scale (accuracy ± 1 gram), whilst the sample volume was obtained by immersing the debris in a prismatic tub filled with water and measuring the water level change (and thus the volume change).

Debris pieces were used according to two different classifications: uniform and non-uniform length debris. The former were sticks of uniform size (i.e. length and diameter of all pieces were kept relatively constant) and adopted for groups U, D, H, T, B, and P, whereas the latter were sorted according to a distribution of the length of the elements and used for groups N1-N13.

Field observations of woody debris accumulations suggest that jams are more likely to be formed by elements the length of which is non-uniformly distributed (Sedell et al., 1988; Blersch and Kangas, 2014), i.e. the length of debris pieces can significantly vary within the same jam. An exception to this non-uniform distribution would be found in those forested areas subject to logging or similar human activities. Accumulations are typically initiated by a key-element and then completed by smaller pieces (Diehl, 1997; Manners et al., 2007; Manners and Doyle, 2008; Lagasse et al., 2010). In natural rivers, distributions of these lengths are typically skewed towards smaller sizes (Blersch and Kangas, 2014). For the definition of a suitable function representing the lengths distribution, published data by Hess (2007) was used. The author measured the length of 156 debris on the South River (Virginia, US). This data was used to fit a log-normal probability density function:

$$p(\varepsilon) = \frac{1}{\varepsilon\sqrt{2\pi}\sigma} e^{-\left(\frac{\ln\varepsilon-\mu}{\sqrt{2}\sigma}\right)^2} \tag{3.4}$$

where ε is the ratio between debris length of a smaller piece L_i and the length of the key-element L_{key} (i.e. L_i/L_{key}), μ and σ are respectively mean and standard deviation of $\ln\varepsilon$.

Through maximum likelihood estimation (MLE) regression analysis, values of μ and σ for the data by Hess (2007) were computed as μ=-1.3039 and σ=0.7367. To produce the sets of debris pieces distributed according to (3.4), the probability density function was discretised in ten different class intervals for the ratio L_i/L_{key} between 0 and 1. Frequency p_i of each size class was determined as

$$p_i = \frac{1}{\Delta\varepsilon} \int_{\varepsilon_{1_i}}^{\varepsilon_{2_i}} p(\varepsilon) d\varepsilon, \tag{3.5}$$

where $\Delta\varepsilon$ is the class width for given values of the ratio L_i/L_{key}, fixed at 0.1 for all cases and ε_{1_i} and ε_{2_i} are the two limits of each class interval. The integral in (3.5) gives the frequency of each class and can therefore be used to determine the number of sticks for a length class relatively to the key-element. Figure 3.5 shows both the curve form (3.4) and bars from integration in (3.5). The distribution in (3.4), with the μ and σ values as found, displays a trend similar to data by Sedell et al. (1988), which was based on about 2000 observations. It also resembled the trend of other published distribution curves (e.g. Manners and Doyle, 2008; Cadol and Wohl, 2010; MacVicar and Piégay, 2012; Blersch and Kangas, 2014). According to the above defined distribution, a set of 13 distributed debris mixtures was produced, each of which was characterised by the length of the longest debris (i.e. the key-element). Smaller elements were added to each group in order to complete the length distribution. Figure 3.6 depicts two samples of 100 debris pieces produced from two different key-elements.

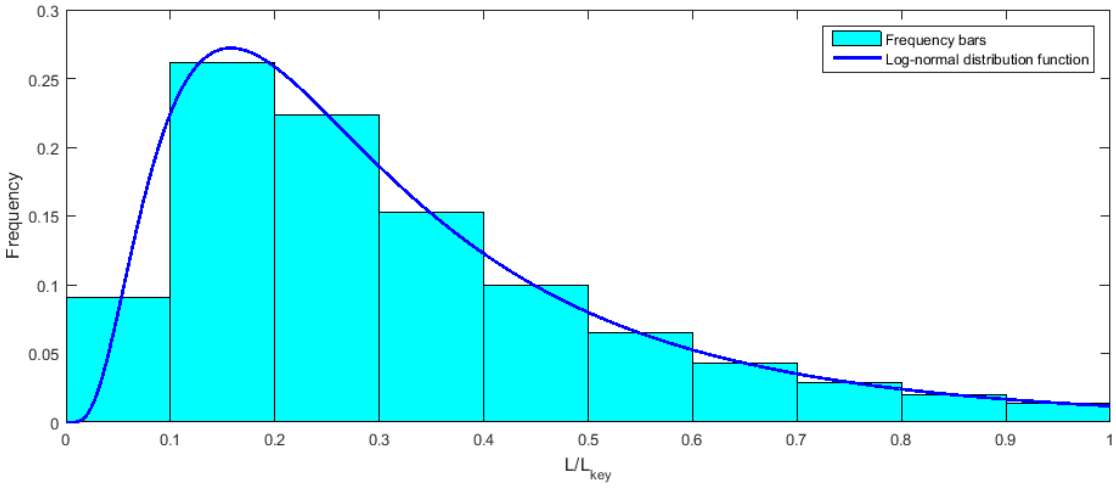

FIGURE 3.5: Bars and log-normal function of debris lengths frequency in rivers expressed as the ratio between the piece length L_i over the key-element length L_{key}.

An exception to the above types of debris elements is made for groups B1 to B3, which will be discussed later.

(A) L_{key}=375mm (B) L_{key}=500mm

FIGURE 3.6: Sets of 100 pieces distributed according to (3.5) for two different key-elements.

3.2.4 Pier Types

Bridge piers were modelled using 600 mm-long solid circular cylinders of different sizes. For the large majority of experiments, piers were used with circular shape of diameter 25 mm, 50 mm, and 100 mm. This shape was adopted as an example of the many possible piers that can be found globally and the diameter was chosen in order to produce values of L/D that are typically observed in the real-world, e.g. in the range 5.2-43 in the US (Lagasse et al., 2010). The influence of this variable on the formation of accumulation was the object of experimental groups U1 to U5 and N1 to N13. For any other test, pier size was kept at 50 mm. Figure 3.7 shows the three PVC piers adopted. Nevertheless, diameter and shape of bridge piers vary significantly and it is therefore necessary to understand their potential influence on the formation of debris jams.

For experimental groups P1 to P5, the pier shape was varied, as will be discussed later.

3.2.5 Experimental Groups

The goal for each experimental group was to analyse the impact from a specific dimensionless variable (as found in (3.3)) or factor on the formation and size of debris jams. The variation of the debris Froude number Fr_L was studied for all groups.

Experimental groups U1 to U5 in Table 3.2 were performed with the purpose to analyse the influence of the ratio L/D on the characteristics of the formed jams. In these experiments, both the debris length L and the pier diameter D were varied. The tested values of L/D ranged from 3.75 to 15 which are within those observed in natural environments (Lagasse et al., 2010). Table 3.3 shows detailed values of L, D, and L/D for each U group.

FIGURE 3.7: PVC model piers used for experiments. Left to right: 25 mm, 50 mm and 100 mm diameter.

TABLE 3.3: Detailed values for experimental groups U1 to U5.

Group	Debris length L (m)	Pier diameter D (m)	L/D
U1	0.375	0.100	3.75
U2	0.250	0.050	5.00
U3	0.3125	0.050	6.25
U4	0.375	0.050	7.50
U5	0.375	0.025	15.00

Groups N1 to N13 were performed with a goal similar to the experimental groups U, varying values of L/D between 5 and 30. Nevertheless, these experiments were conducted with non-uniform length debris distributions and had the additional objective of evaluating the growth of a debris jam when formed by these mixtures. In this case, the debris length L value reported in Table 3.4 corresponds to the length of the key-element from which the mixture is derived.

An additional set of tests was carried out with non-uniform length debris in order to evaluate the stochasticity of the phenomenon and the dispersion of the formed dimensions. These tests were conducted with the same key-element length (687.5 mm) and (approximately) same flow conditions and was repeated 22 times. This group of tests is identified by the R1 group in Table

TABLE 3.4: Detailed values for experimental groups N1 to N13.

Group	Debris length L (m)	Pier diameter D (m)	L/D
N1	0.500	0.100	5.00
N2	0.625	0.100	6.25
N3	0.375	0.050	7.50
N4	0.4375	0.050	8.75
N5	0.500	0.050	10.00
N6	0.5625	0.050	11.25
N7	0.625	0.050	12.50
N8	0.6875	0.050	13.75
N9	0.750	0.050	15.00
N10	0.4375	0.025	17.50
N11	0.500	0.025	20.00
N12	0.625	0.025	25.00
N13	0.750	0.025	30.00

3.2.

Experimental groups D1 to D6 were aimed at investigating the effects of the diameter of debris elements on the accumulation process. For this purpose, debris used for these groups were chosen with fixed length L (375 mm) and diameter varying between each group. Table 3.5 reports the value of diameters used and the d/L ratio. It should be noticed that the d/L ratio was also varied for U and N experimental groups - as diameter was kept constant while debris length varied - even though this range ($3.16\text{x}10^{-2} \leq d/L \leq 4.74\text{x}10^{-2}$ for U1-U5 groups) was smaller than that tested for groups D1 to D6.

TABLE 3.5: Detailed values for experimental groups D1 to D6.

Group	Debris length L (m)	Debris diameter d (mm)	d/L (x10^{-2})
D1	375	7.64	2.04
D2	375	9.65	2.57
D3	375	14.85	3.96
D4	375	17.85	4.76
D5	375	21.59	5.76
D6	375	29.26	7.80

For experimental groups H1, H2, and H3, water depth (and the dimensionless ratio h/L) was kept approximately constant for all experiments within each group, with the aim to evaluate the influence (if any) of the dimensionless ratio h/L. Water depth was controlled by varying the downstream flap gate, the flume slope, and the flow rate. Table 3.6 summarises values of h and h/L for each H test group. In these experiments, debris length L was kept constant at 375 mm.

TABLE 3.6: Detailed values for experimental groups H1 to H3.

Group	Water depth h (m)	h/L	Standard deviation of h (m)
H1	0.294	0.783	0.002
H2	0.370	0.986	0.002
H3	0.448	1.195	0.004

Groups T1 and T2 were performed with two different debris densities, respectively 396 kg/m^3 and 860 kg/m^3, in order to assess the effects of the dimensionless group ρ_L/ρ on the jam dimensions. Density was kept under control in two different ways: for T1 experiments, debris were dried by a drying system until reaching approximately an equilibrium (i.e. constant density). Then, after each experiment they were dried again until reaching constant density. On the other hand, for the T2 group debris pieces were submerged into a water tank overnight and then tested on the following day. Both T1 and T2 had debris length 375 mm and diameter 11.85 mm.

Groups B1-B3 were aimed at analysing the influence of shape complexity on the process of entrapment of individual debris pieces and the growth of the jam. Figure 3.8 displays a representative element for each group B1, B2, and B3 (as well as a standard uniform stick used for the other experimental groups), showing the differences in debris shape complexity studied in this work. The lowest level of complexity is represented by dowels (B1), which are perfectly cylindrical and have a smooth surface. The dowels density was (approximately) 560 kg/m^3, which is very close to the range used for natural sticks. The next level of shape complexity refers to non-branched sticks (all experimental groups already discussed) which are not perfectly straight, may display slight variations of diameter and are rougher than dowels. The introduction of branches is used to add further complexity to the geometry of large wood debris. In general, the characterisation of the complexity of debris shape is of difficult definition due to the many combinations of number of branches (and sub-branches) and their corresponding dimensions. For this reason, in this work a pragmatic approach is adopted where only single-branched debris elements (i.e. natural sticks with a single branch) are tested. However, the potential influence of the size of branches has been analysed by using two values of the perpendicular distance b between the centre of the main straight element and maximum extension of the branch (as shown in Figure 3.8). Namely, groups B2 and B3 were characterised by values of b/L=0.25 and b/L=0.50, respectively. The values of b/L were arbitrarily selected in order to evaluate the potential influence of this variable on the jam size in a broad range. All sticks had a length of 375 mm and diameter of 11.85 mm (on average, standard deviation of 1.24 mm). The only exception to this was group B1, in which a diameter d=12 mm was used because of commercial availability of dowels. Table 3.7 shows a summary of properties studied for groups B2 and B3.

Experimental groups P1 to P5 were focused on the effects of pier shape on LWD jam growth and maximum size. In this study, five of the shapes studied by De Cicco et al. (2016) were replicated with some minor differences. Figure 3.9 shows the detailed cross-sections for piers used in groups P1 to P5. Maximum width of the pier in the streamwise direction was kept constant

FIGURE 3.8: Types of debris elements used in this experimental study for uniform length pieces. From left to right: wooden dowel (group B1), non-branched natural stick (groups U, D, H, T, and P), branched sticks - small branch (group B2), and branched sticks - large branch (group B3).

TABLE 3.7: Detailed values for experimental groups B2 and B3.

Group	Debris length L (mm)	Branch length b (mm)	b/L
B2	375	93.75	0.25
B3	375	187.5	0.50

for all groups at D=50 mm. For group P1, a square pier of side 50 mm was used, whereas pier P2 was an isosceles triangle having internal angle at the upstream vertex of 45°. Experimental group P3 tested an ogive-shaped pier, based on the von Kármán ogive function, the shape of which minimises drag (Pert, 2013). This particular ogive shape was chosen only for the wide use of the function in engineering applications, but did not have a specific use for the debris piles problem. For groups P4 and P5, the cross-sections used were, respectively, a regular trapezoid having minor base 25 mm and major base 50 mm, and an upstream looking half-circle of diameter 50 mm. The pier used for experiments in group P1 was a square rod of polyvinyl-chloride, while piers for groups P2 to P5 were made by 3D-printed hollow shells. These were then filled with fine aggregate concrete and coated with bituminous paint in order to leave a surface finish comparable to the other piers. Table 3.8 presents the main characteristics of all shapes used.

TABLE 3.8: Detailed values for experimental groups P1 to P5.

Group	Pier width D (mm)	Shape	Notes
P1	50	Square	PVC bar
P2	50	Triangle	45° vertex angle
P3	50	Ogive	von Kármán ogive
P4	50	Trapezoid	minor base 25 mm, height 25 mm
P5	50	Half-circle	50 mm-wide, 50 mm-long

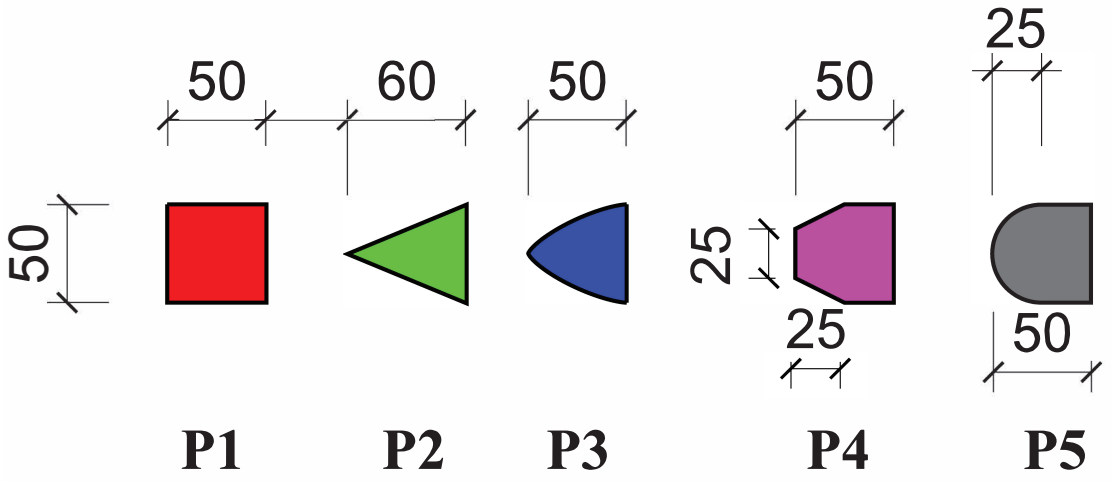

FIGURE 3.9: Model piers used for different pier shapes. Left to right: square, triangle, ogive, trapezoid and half-circle. Measures are in mm.

3.2.6 Experimental Set-Up

3.2.6.1 Set-Up

Figure 3.10 illustrates (not to scale) the flume used and the experimental set-up adopted. Model piers were placed 11 m downstream of the flume inlet. This position guaranteed fully developed flow conditions, according to past studies in the same flume (Myers et al., 2013). The load cell was attached onto the top of the pier by a bolted joint measuring the force in the streamwise direction. To prevent loss of measured load due to friction between pier and flume bed, a small gap of approximately 0.5 mm was left between the pier and bottom of the flume, as sketched in figure 3.1. A bracing structure was placed at the joint with the load cell to minimise vibrations due to the elasticity of the bars.

All tests were continuously recorded by the three cameras positioned at right angles, which allowed the continuous monitoring of the three variables W, H, and K. A camera Logitech C920 was placed on the top of the flume 70 cm upstream from the pier, in the centre line and at a height of 145 cm from the flume bottom, slightly angled pointing downstream, that measured the width W and the length K. Another camera Logitech C920 was placed on the hydraulic left side of the

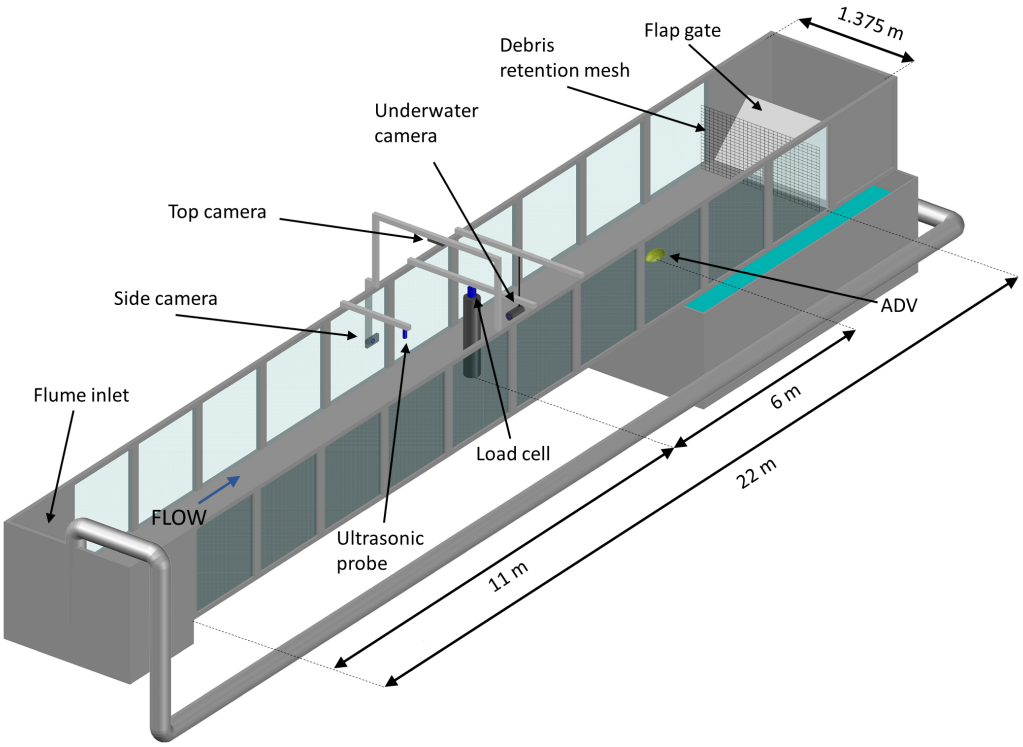

FIGURE 3.10: Sketch of the flume set-up showing the position of the instruments used (not to scale). Sumps and pipes are simplified for ease of representation and only the ultrasonic sensor closest to the pier is represented.

flume, 30 cm upstream from the pier and 30 cm from the flume bed, recording the vertical (i.e. H) and longitudinal (i.e. K) growth of the accumulation. The cylindrical underwater camera held by a thin bar was placed in the channel centre line, 25 cm from the flume bottom and 60 cm downstream from the pier, measuring the height H and the width W. Its size (a diameter of 35 mm), shape, and location were chosen to minimise the alterations on the upstream flow conditions. These three cameras together provided a detailed description of the time evolution of the shape and size of the accumulation in three dimensions. Size measurements were made possible by using a reference mesh, the image of which was captured prior to each experiment. For the top camera, a ruled paper with a square mesh of 10 mm side was used, which was positioned at different elevations in order to account for depth variations during the experiments. A wired square mesh of 12.7 mm side was submerged to serve as a reference for the other two cameras. Appendix B shows pictures of the calibration meshes. Figure 3.11 shows the set-up at the pier location, displaying pier, cameras, and load cell.

The acoustic doppler velocimeter (ADV) IQ Plus was placed 6 m downstream from the pier. This position was preferred to an upstream location in order to ensure that flow measurements were occurring at a relatively undisturbed cross-section at all times, e.g. not being subject to backwater effects. However, in presence of large accumulations (generally for $L \geq$625 mm) the flow field recorded by each cell showed some modifications due to the extension of the wake at the section of measurement. The resulting velocity profiles were typically slowed down at

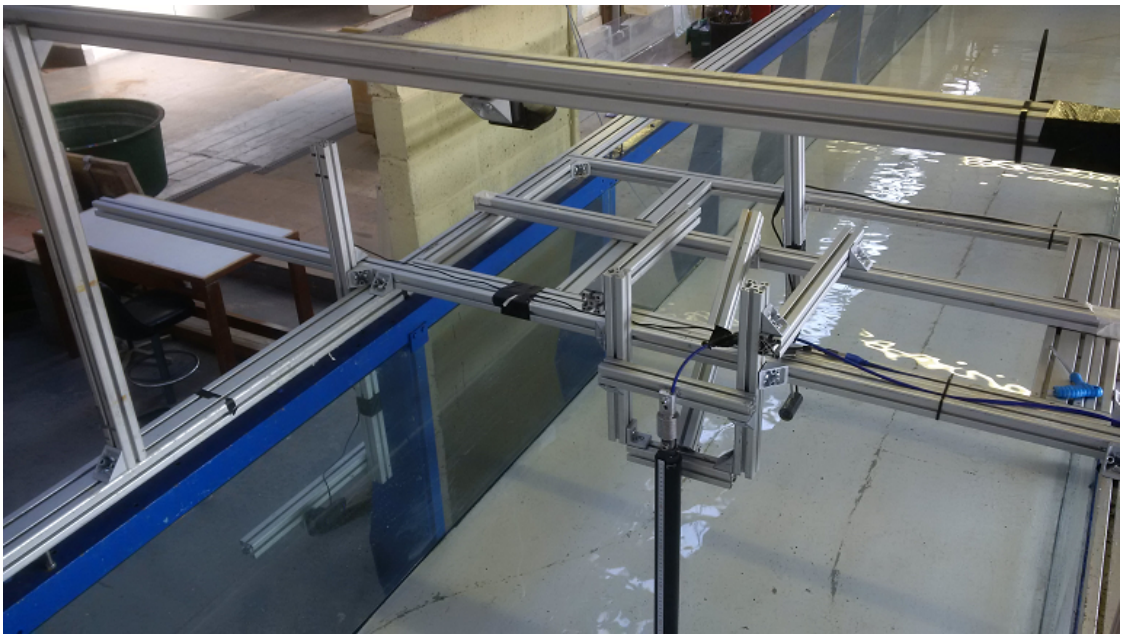

FIGURE 3.11: Experimental set-up displaying pier, load cell, cameras and aluminium braces. Downstream viewing.

the central beam and accelerated on the external beams. However, since the IQ Plus recorded the cross-section averaged velocity and discharge before and after the accumulation formation, comparisons between the undisturbed and disturbed situations showed only very minor alterations (i.e. typically less than 1% on the average values). Therefore, the wake did not invalidate the discharge measurements even under large accumulations.

A series of four ultrasonic sensors was placed at the flume centreline at 6 m (US1), 4 m (US2), 2 m (US3), and 1 m (US4) upstream from the pier nose. A closer position would have not been possible as the accumulation could have reached the sensors recording location, altering the results. The combined use of ADV and ultrasonics allowed the definition of the average velocity at the pier cross-section. The velocity at the pier cross-section was computed as the ratio between the discharge measured by the ADV and the cross-sectional area at the pier. This approach was possible since all experiments were carried out with steady flow conditions and constant discharge.

3.2.6.2 Experimental Procedure

Although each group of experiments was aimed at investigating different variables, the experimental procedure was kept consistent throughout all 732 experiments. Experiments started turning on the pumps (with all equipments and instruments already positioned and calibrated) and then regulating the flow with valves and flap gate until reaching the desired velocity or water depth. Water was pumped from the sumps underneath the flume. Flow conditions were checked by real-time data from the downstream-placed ADV. Data collection and debris-feeding were

begun as soon as the desired flow conditions were established.

Debris elements were individually introduced into the flume at a distance of 7 m upstream of the pier. Debris elements were manually dropped onto the water surface at a distance of (approximately) 50 mm and released parallel to the streamwise direction, reproducing the mode of transport of individual logs observed in natural streams (Diehl, 1997). The only exception regards the non-uniformly distributed debris (groups N1 to N13) in which, unlike all the other tests, experiments were started with a key-element already in place at the pier. The dropping point was at the flume centreline, after which debris elements were left free to move with the current, remaining at the water surface. A dropping frequency of approximately 20 debris/min was used in all experiments, which represents the *uncongested* mode of debris transport (defined by Braudrick and Grant (2000) as the condition when logs or branches are transported individually, rather than in clusters). This type of transport has been previously described as the most commonly observed in rivers (Braudrick and Grant, 2000; Lyn et al., 2003; Lagasse et al., 2010). The analysis of video recordings of a preliminary set of tests indicated that in *uncongested* mode of transport, the debris dropping frequency could change the speed of the growth, but would not significantly change the final dimensions of the formed debris piles. Therefore, the dropping frequency was kept constant for all experiments and focused on the analysis of other variables that were deemed to play a more important role on the final dimensions. Only short interruptions were necessary to remove non-accumulated sticks and which did not have any influence on the process. These non-accumulated sticks were prevented from reaching the sumps by a wired screen placed at the flume outlet, and were frequently removed to avoid any unwanted backwater effect. In experiments with high flow velocity, a small number of debris elements needed to be manually placed at the pier in order to initiate an accumulation, which would otherwise have taken too long to form by the stochastic process of self-assembly observed in other experiments. This operation was conducted only for a reduced number of tests, typically those at the highest range of Fr_L, and only to initiate the accumulation process.

3.3 Summary

The knowledge gap about woody debris accumulations revealed that a deep understanding of the formation and growth of these jams is required. Therefore, in order to bridge this gap an extensive experimental analysis was planned. A preliminary dimensional analysis was carried out in section 3.1 with the goal to define a relationship among the dimensionless variables important to the LWD phenomenon. Furthermore, this ensures similarity between laboratory and prototype scale. The choice of the debris length L as part of the repeated group in the dimensional analysis suggested that the resulting dimensionless ratios of the debris jam size are a function of other dimensionless groups, e.g. the debris Froude number Fr_L. Experimental planning was based on these findings and dimensionless groups obtained from dimensional analysis were individually

tested for assessment.

Experiments were conducted at the University of Southampton Internal Flume in Chilworth. The main factors identified by the dimensional analysis were tested by several experimental groups. Measurements were performed through state-of-the-art devices, which allowed the highest levels of accuracy. All tests followed the same standardised procedure: once flow conditions were established, debris elements (modelled by natural sticks) were individually dropped and left free to travel and accumulate at the bridge pier. Each experimental group was studied varying only a relevant variable per time. Also, a broad range of flow conditions was tested for each group. In total, 732 experiments were conducted.

Chapter 4

Experimental Results

This chapter presents the results from 732 experiments in which the formation of woody debris jams accumulations at bridge piers was modelled as described in the previous section. The chapter describes the temporal evolution, and identifies key-stages of jams growth and formation. A detailed analysis of the maximum size that jams reached over their life-time and an assessment of the intervening factors on the formation processes are then presented.

4.1 Time Evolution of Debris Jams at Piers

The evolution of debris accumulations observed in all experiments presented in this study repeatedly showed a similar pattern that can be conceptually classified as three different phases, hereafter referred to as *unstable*, *stable* and *critical*. This conceptualisation is developed from quantitative and qualitative observations. Figures 4.1 and 4.2 show the evolution of ω, η, κ, and the measured drag force (vertical axes) in time (horizontal axis) for three examples at different values of Fr_L for, respectively, group U4 (uniform length debris) and group N5 (non-uniform length debris). At the beginning of the build-up process, the debris pile is formed by only a few elements that are anchored to the pier at the water surface. These members significantly increase the width of the debris recruiting area, resulting in a rapid increase of the three geometrical variables W, H and K as well as of the force exerted onto the pier. During this initial development, which was classified as *unstable*, debris can be easily detached from the jam either individually or in clusters resulting in frequent variations of the geometrical variables, or even in an early jam failure.

After the LWD pile has created a stable net of entangled elements, its width is subject to smaller and more gradual variations. The accumulation height follows a similar trend, although it reaches a more regular state later during the experiment. This stage is classified as a *stable* jam condition. During the development of this phase, the shape of all debris accumulations resembled a half-cone pointing downwards, which results in a triangular cross-section, although minor

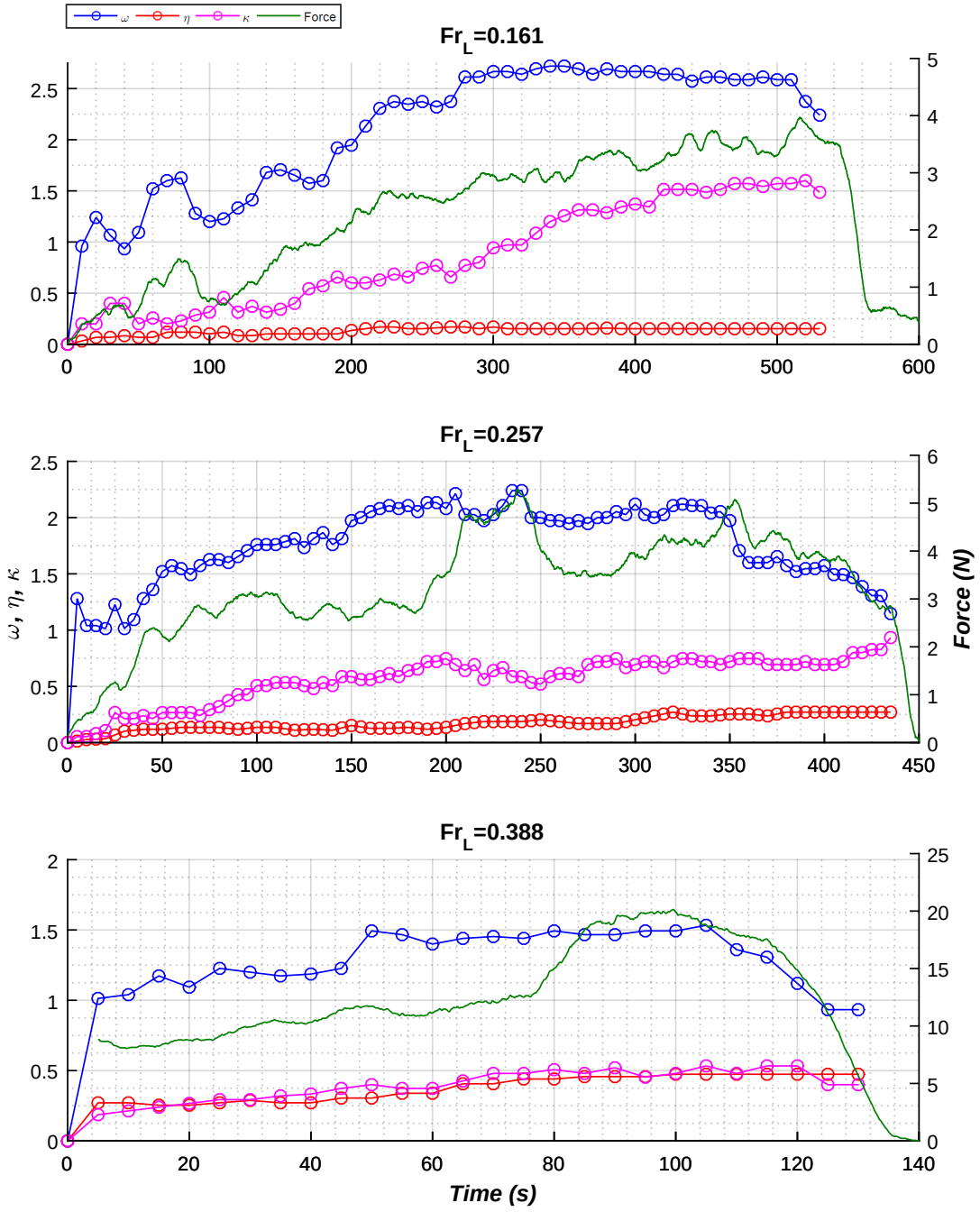

FIGURE 4.1: Time evolution of dimensionless width ω (in blue), height η (in red), and length κ (in magenta), as well as drag force (in green) for three uniform length debris experiments from group U4.

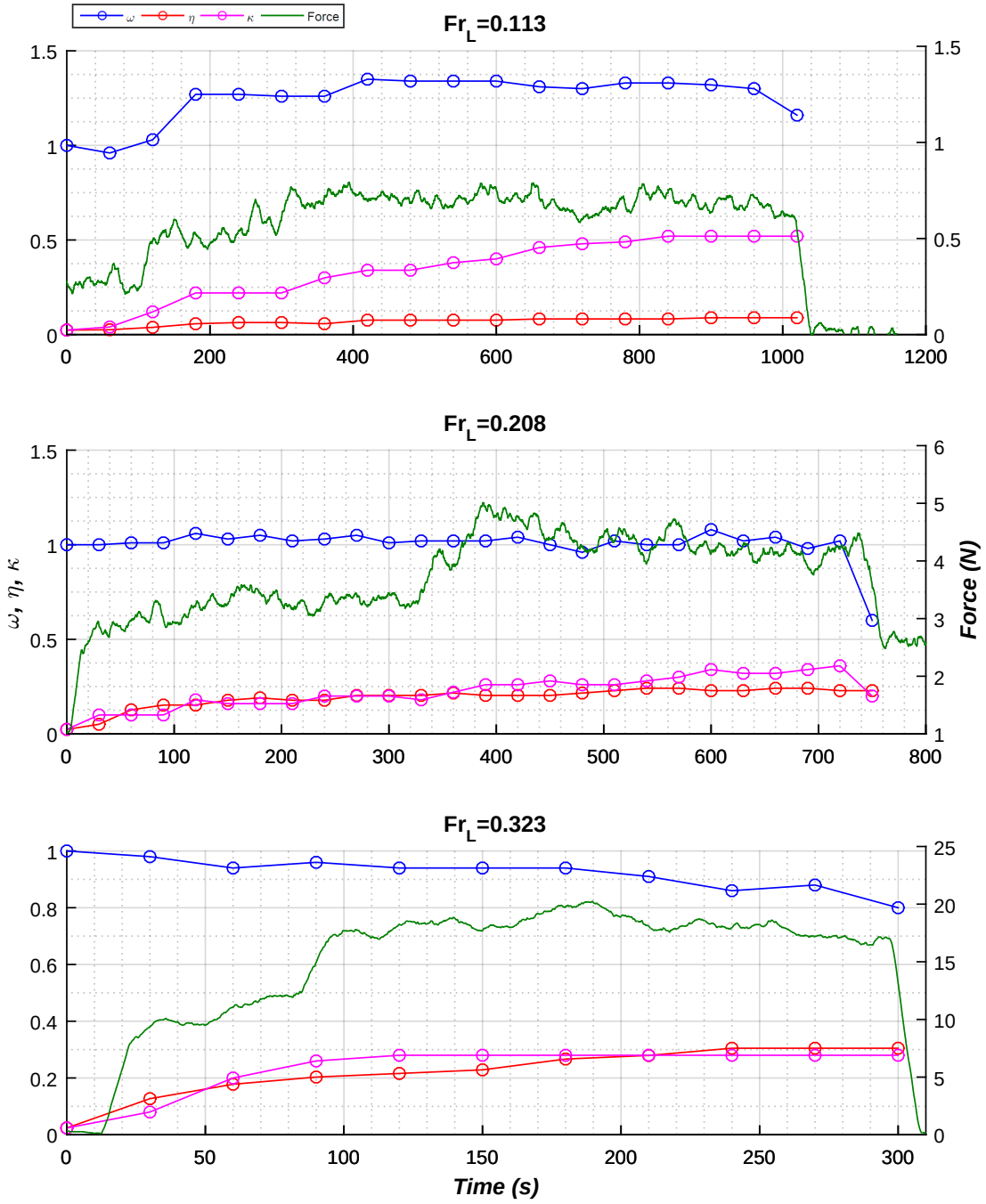

FIGURE 4.2: Time evolution of dimensionless width ω (in blue), height η (in red), and length κ (in magenta), as well as drag force (in green) for three non-uniform length debris experiments from group N5.

FIGURE 4.3: Typical accumulation shape during the stable phase for a non-uniform size debris test (L=500 mm, D=50 mm, v=0.411 m/s resulting in L/D=10 and Fr_L=0.186). Images were captured at the same instant from: (***a***) top camera, (***b***) underwater camera located downstream from the pier, (***c***) side camera.

deviations were observed because of the inherent imperfection of geometric shapes formed by debris. The base of the jam is not circular as the values of K can differ significantly from $W/2$. Figure 4.3 shows a typical accumulation shape in this stable condition as observed by the three cameras. The cross-section of the accumulation was found to be asymmetrical in all experiments when reaching the stable phase. Asymmetry is defined here as the condition in which the ratio between the left and right semi-widths W_L and W_R of the accumulation at the water surface (where W_L and W_R are respectively cross sectional distances from the pier centre to the left and right edges of the debris jam) is different than unity. Although the duration of each phase varied for each test, it was clearly observed in all experiments that the stable condition lasted longer than the other two phases.

Finally the last stage (critical) is reached when the jam begins an oscillatory rotational movement about the pier. This motion begins autonomously and it is not a consequence of the impact of individual debris, but rather the result of the jam growth and spatial development. During this phase debris feeding continued uninterrupted. Eventually, these oscillations lead to the disengagement of the accumulation from the pier, which then drifts away (i.e. is dislodged from the pier by the flow). Figure 4.4 shows the final rotational sequence of an accumulation during the failure stage. The duration of this last phase varied for each test. At high flow conditions failure occurred abruptly through a single and sudden rotation. Figure 4.5 shows a conceptualised example of the jam size growth in time and a sketch of the different stages observed during the lifetime of an accumulation in order to qualitatively represent the vast majority of accumulations observed.

The failure behaviour described above was observed in all tests and began when W, H and K were very close to their maximum values over the course of the experiment. Thus, the accumulation size at the onset of the critical stage can be regarded as a proxy for the maximum potential dimensions that modelled jams can reach, even though in some cases they were not strictly maxima. In this work, values of width, height, and length measured at this stage (hereafter denoted by the superscript c for critical) are shown as the maximum values obtained during the experiments.

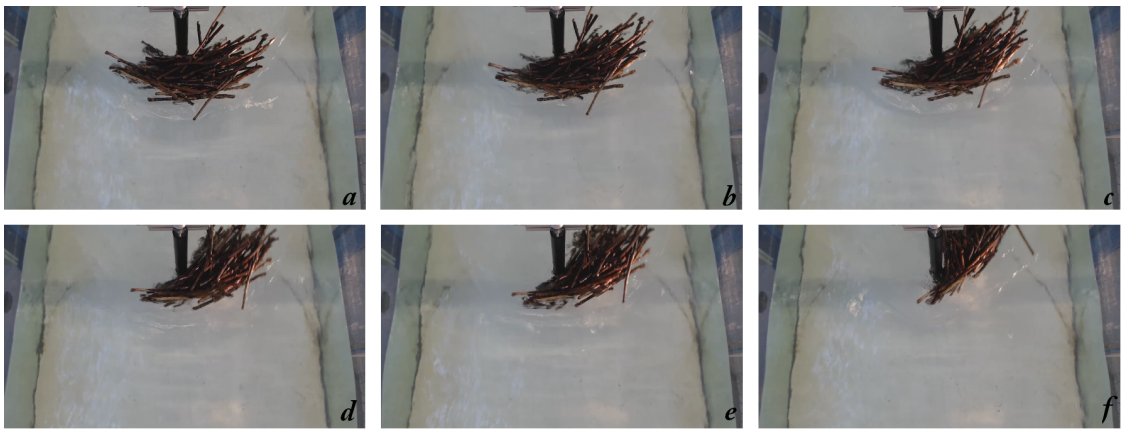

FIGURE 4.4: An example of accumulation failure for uniform size debris at the upstream face of the pier. The jam gradually rotates about the pier axis until it is completely dislodged from the pier and drifts away. Photos *a* to *f* are taken with intervals of 1 second between each other.

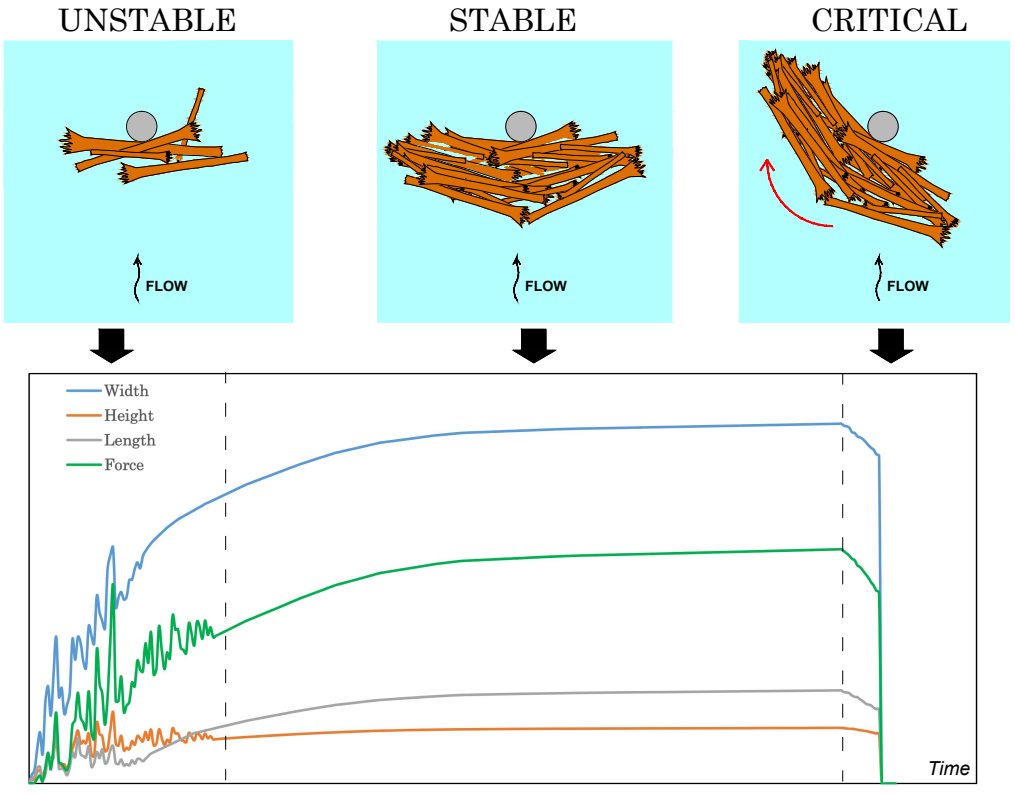

FIGURE 4.5: Conceptual sketch of the three growth phases typically observed in a jam. On the top: exemplified planar view. On the bottom: conceptualised plot based on actual data for growth in time of the main geometrical variables and of the applied force.

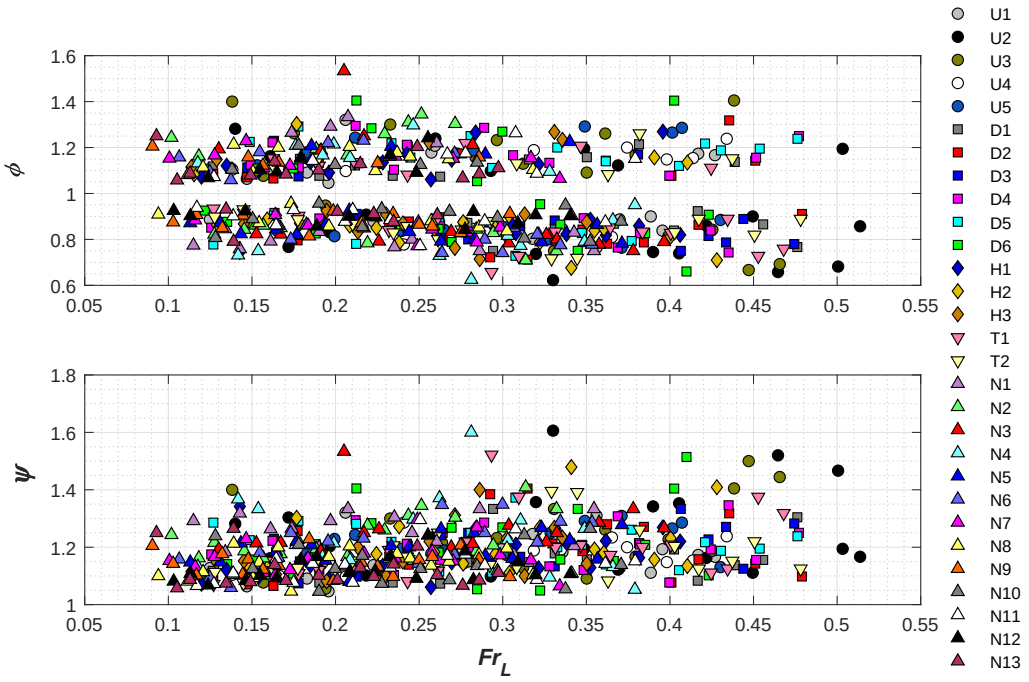

FIGURE 4.6: Asymmetry factors ϕ and ψ for all experiments (except groups P and B) against Fr_L. On the top ϕ=W_L^c/W_R^c, on the bottom ψ=W_{max}^c/W_{min}^c.

In all tests, failure occurred as a rotation towards the side of the largest semi-width. For instance, a jam as sketched in Figure 3.1 fails rotating clockwise if the semi-width on the left side is greater than the semi-width on the right side of the pier (i.e. W_L>W_R), otherwise it will rotate anticlockwise. This is what occurred to the jam in Figure 4.4, in which rotation was anticlockwise and the right semi-width W_R larger than the left semi-width W_L. The deepest point of the jam was observed at the pier face in virtually all experiments. In order to understand the influence of asymmetry on failure, two asymmetry factors $\phi = W_L^c/W_R^c$ and $\psi = W_{max}^c/W_{min}^c$ (where W_{max}^c and W_{min}^c are respectively the largest and smallest of W_L^c and W_R^c at the critical stage) are introduced. The values of ϕ and ψ for all experiments with both uniform and non-uniform debris are plotted as a function of Fr_L in Figure 4.6. These results show that an accumulation generally fails at values of ϕ within the narrow range of approximately 0.70-0.95 and 1.05-1.30 (ψ between 1.05-1.30), and that ϕ and ψ are also independent of Fr_L. No failure occurred for values of ϕ and ψ close to unity, which suggests that failure is primarily caused by the moment of the drag force induced by asymmetry (i.e. a shift of the centre of pressure away from the pier axis, that is the axis of rotation). In addition, in Figure 4.6 no noticeable differences are observed between the results of uniform and non-uniform debris experiments. Finally, it has been observed that flow conditions distinctly affect the life-time of a woody debris jam, substantially reducing the time of all phases with increasing Fr_L, as it can be noted in Figures 4.1 and 4.2.

The following sections will separately analyse the relations between the potential geometry of debris jams (represented by ω^c, η^c and κ^c) and flow and debris characteristics for uniform and non-uniform debris.

4.2 Maximum Size of Large Wood Jams

The following section analyses the maximum dimensionless size that was reached by woody debris jams during the experimental analysis. Appendix C provides an overview on the corresponding dimensional results.

4.2.1 Uniform Length Debris

Figure 4.7 shows the three relations between the variables characterising the critical geometry of the debris accumulations (i.e. ω^c, η^c and κ^c) and Fr_L for all experiments with uniform debris, i.e. groups U1 to U5, D1 to D6, H1 to H3, and T1 to T2. The figure shows a clear and strong dependency of the geometry of accumulations on flow, with all values clustered within a relatively narrow band. At low Fr_L the critical width is largest, reaching a value of 2.5 to 3 times the length of an individual debris element (i.e. ω^c=2.5 to 3). The value of ω^c gradually decreases with Fr_L down to $\omega^c \approx 1.5$ for the highest values of Fr_L tested. An opposite trend is observed for the dimensionless height η^c, which displays an increase with increasing Fr_L. Namely η^c values vary from around 0.1 at $Fr_L < 0.15$ up to $\eta^c \approx 0.5$ at $Fr_L \approx 0.47$. In other words, the cross-sectional shape of the accumulations changes from wide and superficial for low Fr_L values to narrow and deep with increasing Fr_L. The dimensionless streamwise length of the accumulation κ^c gradually drops with increasing Fr_L down to an average value of approximately κ^c=0.5. The other dimensionless parameters showed limited influence on the size of debris accumulations and will be discussed in detail in section 4.4.

4.2.2 Non-Uniform Length Debris

Results for the critical width ω^c, height η^c and length κ^c for all 13 groups of experiments performed with non-uniform length debris (N1 to N13 on table 3.1) are presented in Figure 4.8. Similarly to the results of the uniform debris tests, ω^c and κ^c decrease whereas η^c increases with increasing Fr_L. The highest values of ω^c range approximately between 1.1 and 1.5 at low Fr_L, and decrease down to around $0.8 \sim 1$ for the highest values of Fr_L tested. For $Fr_L > 0.25$ an important number of experiments displayed values of ω^c below 1, i.e. the accumulation width is smaller than the length of the key-element. This occurs when the key-element is tilted from its initial position perpendicular to the flow, resulting in a smaller cross-sectional width. The dimensionless height η^c shows small values (around 0.1) at low Fr_L, which then increases with Fr_L up to $\eta^c \approx 0.4$. As previously observed for the uniform debris, the dimensionless length κ^c decreases with increasing Fr_L, ranging from approximately 0.4-0.6 at the lowest to 0.2-0.3 at the highest values of Fr_L tested.

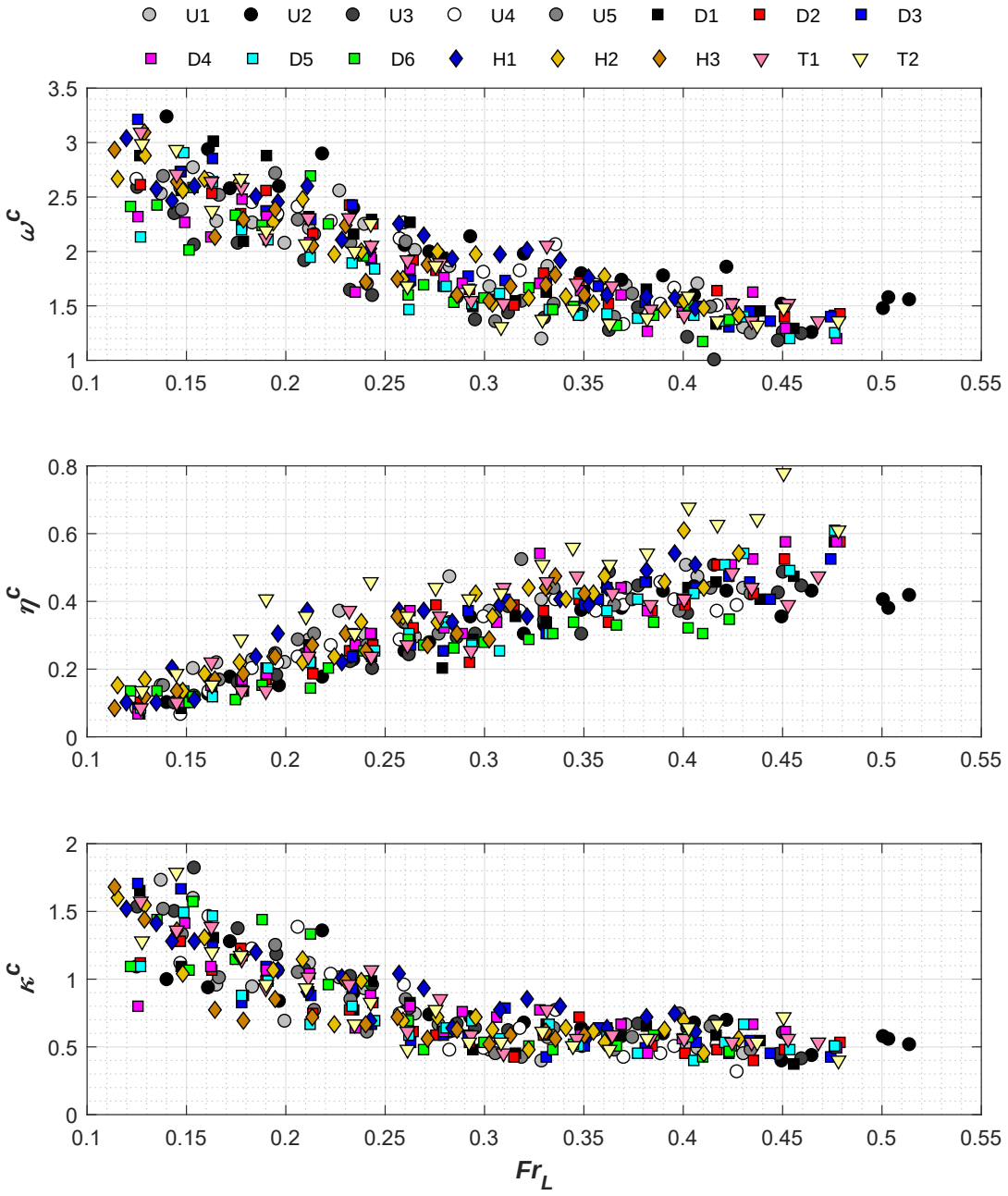

FIGURE 4.7: Critical values of the dimensionless (top to bottom) width ω^c, height η^c, and length κ^c against Fr_L (horizontal axis) for uniform debris tests.

Interesting insights into the influence of the distribution of debris length on the critical geometry of accumulations can be obtained by comparing the values of ω^c, η^c and κ^c in uniform and non-uniform experiments from Figures 4.7 and 4.6. This comparison shows that under the same Fr_L the potential width of a debris jam formed with non-uniformly distributed debris is considerably smaller than the corresponding width of a uniform debris jam. In particular, at low values of Fr_L (around 0.1), observed values of ω^c were up to 2.5 times higher in the uniform than in the non-uniform experiments ($\omega^c \approx 3$ and $\omega^c \approx 1.2$ respectively). With increasing Fr_L this difference is reduced (uniform $\omega^c \approx 1.5$ and non-uniform $\omega^c \approx 0.9$ at $Fr_L \approx 0.47$ and $Fr_L \approx 0.40$ respectively), although it is still high (i.e. the non-uniform debris accumulation is 40% smaller in width). The dimensionless height η^c reveals a less pronounced difference between non-uniform and uniform debris than ω^c. In particular, for low Fr_L the non-uniform η^c tends to be slightly larger than in the uniform case. For higher Fr_L this difference is inverted and η^c for uniform debris is slightly larger than the non-uniform case. In the lower range of Fr_L the values of κ^c observed in the non-uniform debris experiments were approximately one third of the corresponding κ^c values obtained with uniform debris, while at high Fr_L the ratio between non-uniform and uniform κ^c values was approximately half.

4.2.3 Repeated Tests

In order to understand the dispersion associated with the dynamics of debris accumulation and the predictability of the geometrical variables ω^c, η^c, and κ^c, one particular test was repeated 22 times using the same flow conditions and debris characteristics (debris from group N8, L=687.5 mm, D=50 mm, Fr_L=0.173 and L/D=13.75).

The mean value, standard deviation and coefficient of variation (CV) of ω^c in these experiments were 1.0552, 0.1047 and 0.0992, respectively. The values of the same statistical parameters of η^c were 0.2036, 0.0491 and 0.2410, while κ^c displayed values of 0.3193, 0.0889 and 0.2784. The values of CV for ω^c denote a relatively small dispersion (less than 10%) whereas for η^c and κ^c CV is higher, indicating a greater degree of stochasticity for these two variables. These results are summarised in Table 4.1.

TABLE 4.1: Statistical values obtained for the repeated tests of group R1.

Quantity	Mean	Standard deviation	Coefficient of variation
ω^c	1.0552	0.1047	0.0992
η^c	0.2036	0.0491	0.2410
κ^c	0.3193	0.0889	0.2784

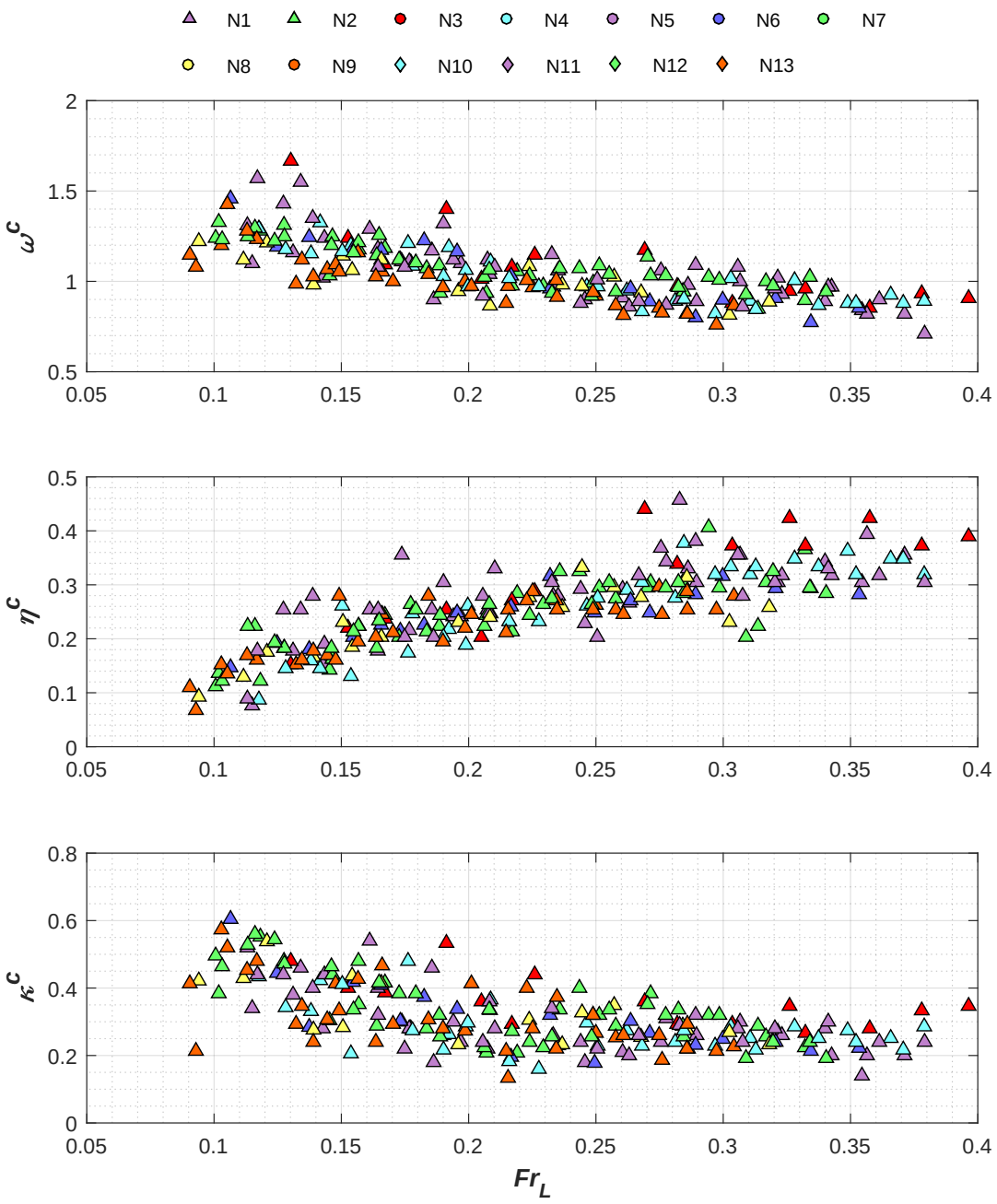

FIGURE 4.8: Critical values of the dimensionless (top to bottom) width ω^c, height η^c, and length κ^c against Fr_L (horizontal axis) for non-uniform debris tests.

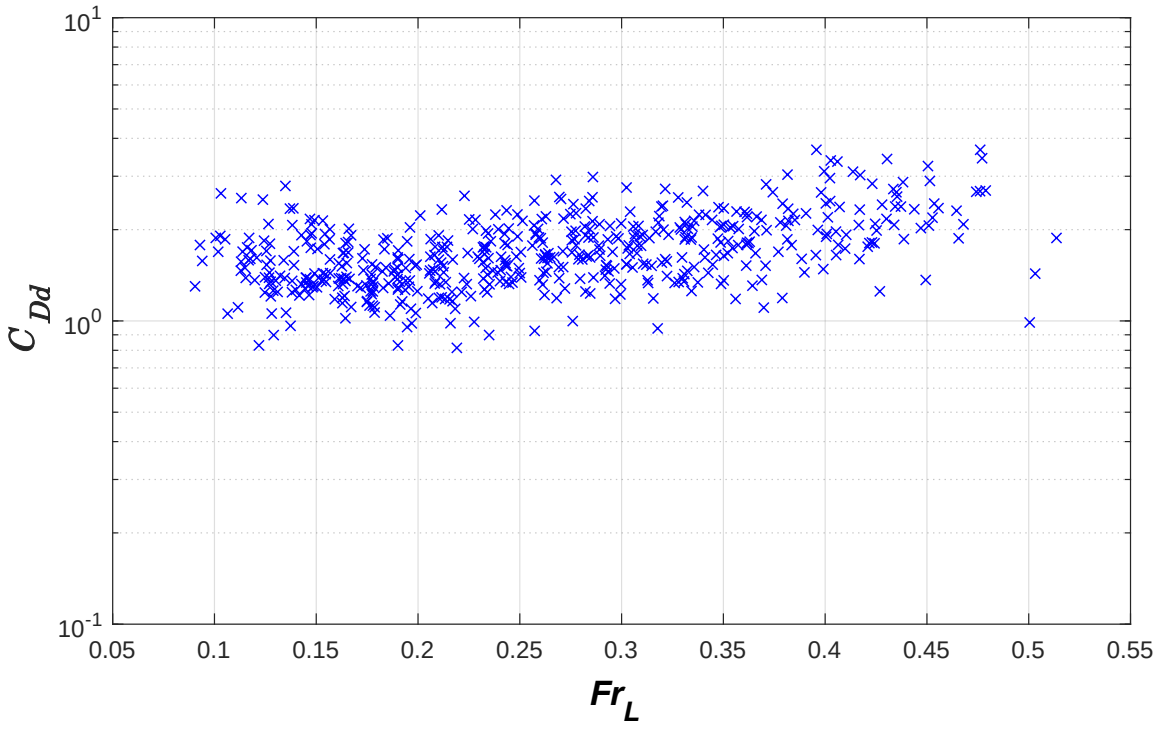

FIGURE 4.9: Drag coefficient C_{Dd} values as a function of Fr_L for all experiments (except groups P and B).

4.3 Drag Force

The force measured by the load cell allowed the analysis of the drag force exerted on the woody debris accumulation. The approaches employed to estimate the drag force exerted by the debris F_{Dd} and the drag coefficient of the debris C_{Dd} are detailed in Appendix B.

As expected, over the course of the experiments drag evolves in time following a trend similar to the growth of the LWD jam. Namely, drag increases at a fast rate during the *unstable* phase of the jam growth, when it is subject to rapid changes that are clearly linked to the changes in the jam size. When the jam achieves the *stable* phase, the rate of change becomes milder and only dependent on the small changes of the jam size. During the *critical* phase, the oscillations of the woody debris pile induce a slight reduction and small variations in the measured force, until it eventually drops abruptly during the jam failure. During each individual test, the maximum drag force values were reached at the onset of the critical phase and are hereafter used for the estimation of the drag coefficient. A sketch of the temporal evolution of the drag force, together with jam size variables, is shown in Figure 4.5.

Figure 4.9 displays values of C_{Dd} for all experiments relatively to Fr_L. While dispersion is relatively high, at low Fr_L most C_{Dd} values are within the range 1.0∼2.0. No systematic differences have been observed in terms of the values of C_{Dd} for the different groups of experiments with uniform and non-uniform debris.

4.4 Main Factors Influencing the Critical Dimensions of Debris Accumulations

The analysis carried out in sections 4.1 and 4.2 highlighted the most important features observed for the formation of woody debris jams and the maximum size that was obtained for both uniform and non-uniform length debris with respect to the debris Froude number Fr_L. In this section, the influence of other individual dimensionless variables identified in the dimensional analysis is assessed, together with other debris and pier features.

4.4.1 Debris Diameter

Figure 4.10 compares the values of ω^c, η^c, and κ^c for experimental groups D1 to D6 against the overall experimental results as shown in Figure 4.7. The figure shows that results are clustered around the same range of values for all dimensionless jam size variables. There is only a (slight) trend that can be noted in regards to debris with the largest diameter (i.e. D5 and D6) in which the accumulation size tends to be in the smaller than other groups for ω^c and η^c, although still within the narrow band of observed data.

4.4.2 Debris Density

Figure 4.11 shows ω^c, η^c, and κ^c for experimental groups T1 and T2 overlapped onto the results of other uniform length debris tests. The results of these experiments showed no noticeable differences for the horizontal dimensions ω^c and κ^c between different values of the relative density ρ_L/ρ. Nonetheless, as shown in figure 4.11, T2 tests (i.e. debris with the highest density) displayed values of η^c up to 30% greater than those with smaller ρ_L/ρ values, whilst T1 experiments followed the general trend. The tendency shown by group T2 could be particularly noticeable for the higher range of Fr_L, whilst less marked for the lowest values of Fr_L tested.

4.4.3 Shape of Individual Debris Elements

Figure 4.12 compares the critical dimensions of debris jams formed by natural sticks (4.12a, for an example from group U4), dowels (4.12b, group B1), and the two branched debris (4.12c and 4.12d, groups B2 and B3, respectively) for a range of Fr_L. The figure illustrates important differences among the four types of debris studied. Qualitatively, through visual observations jams formed by dowels are more densely packed and display a more regular geometry. Dowels tended to be oriented perpendicularly to the streamwise direction of the flow in the first layers of the debris pile, although at the higher range of Fr_L this pattern was less evident. During these experiments, for (approximately) $Fr_L \geq 0.40$, jams could not form under any circumstances. All debris pieces were rapidly removed by the flow, and single elements were entrapped only for a

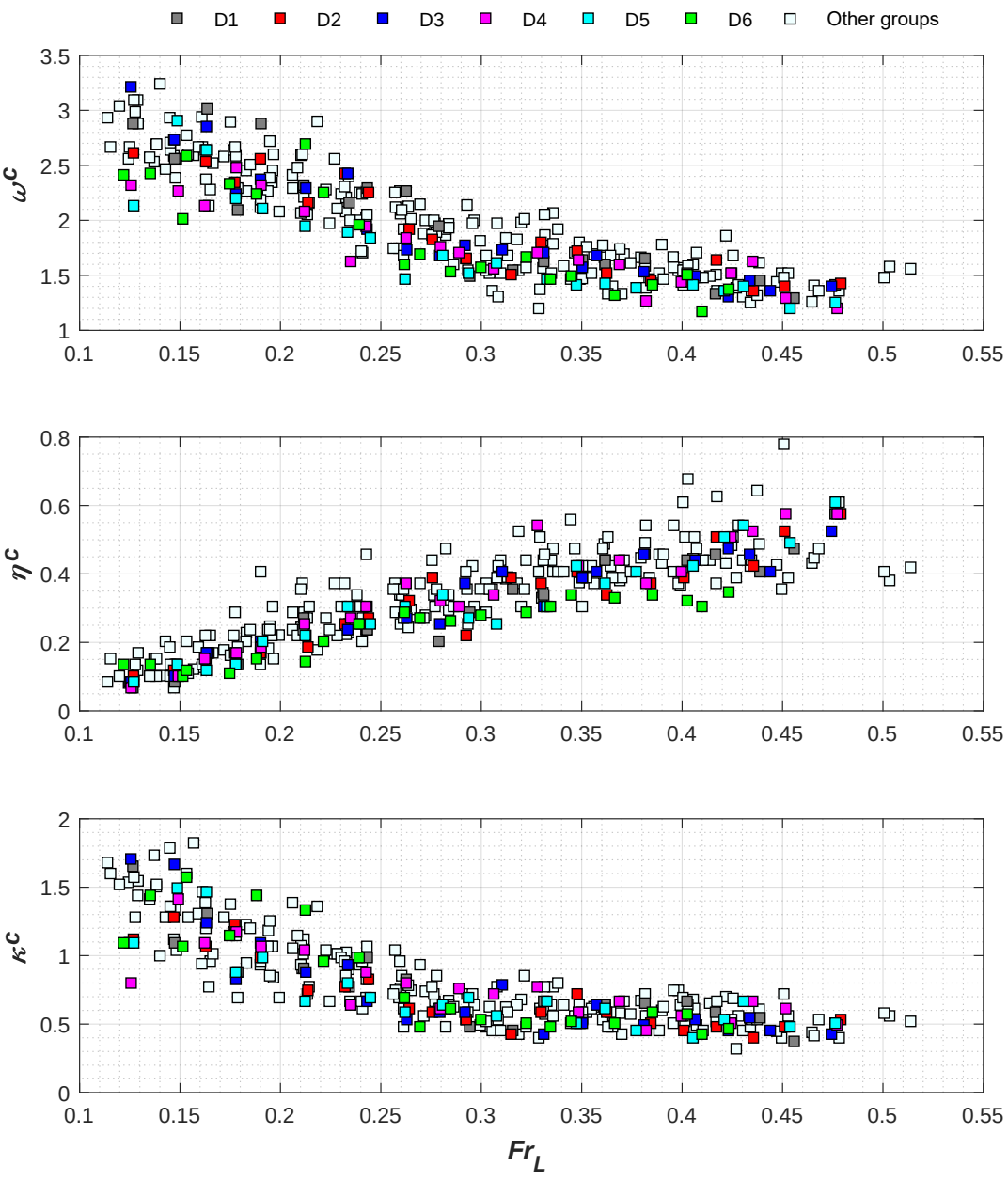

FIGURE 4.10: Values of the dimensionless (top to bottom) width ω^c, height η^c and length κ^c against Fr_L (horizontal axis) for experimental groups D1 (d/L=0.020), D2 (d/L=0.026), D3 (d/L=0.040), D4 (d/L=0.048), D5 (d/L=0.058), and D6 (d/L=0.078) and compared to groups U, H, and T (in light blue).

very short period of time. Furthermore, even when a large number of elements (i.e. more than 15) was placed at the pier in the attempt to initiate an accumulation, they were rapidly dislodged from the pier. Therefore, Fr_L=0.40 can be approximately regarded as the maximum value of Fr_L under which jams formed by this idealised type of debris can possibly develop.

Debris accumulations formed by branched sticks displayed a different behaviour. An example

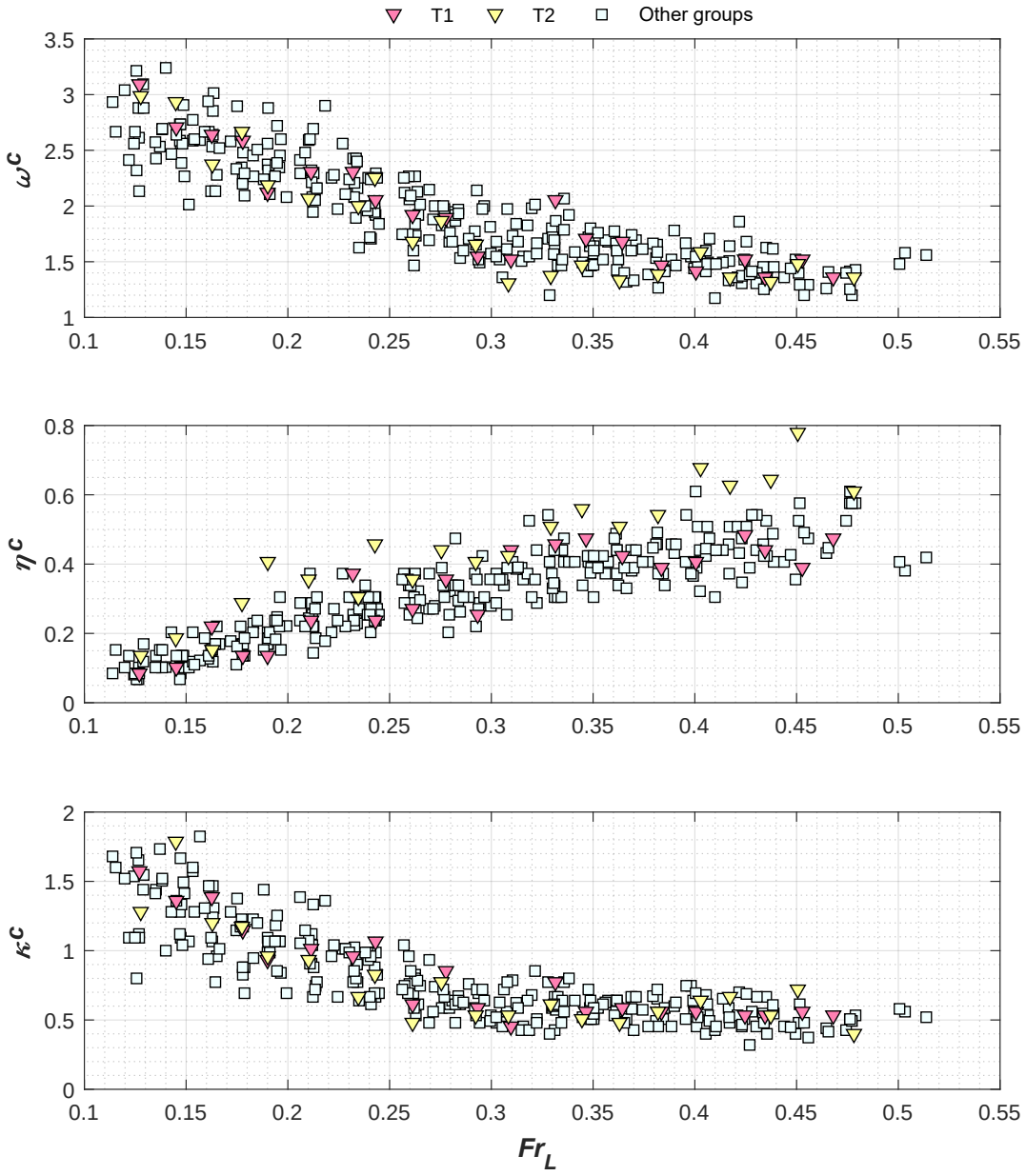

FIGURE 4.11: Values of the dimensionless (top to bottom) width ω^c, height η^c and length κ^c against Fr_L (horizontal axis) for experimental groups T1 (ρ_L/ρ=0.396) and T2 (ρ_L/ρ=0.860) and compared to groups U, D, and H (in light blue).

can be observed in figures 4.12c and 4.12d, which show two jams from groups B2 and B3 under very similar values of Fr_L. Jams formed by branched debris tended to be very unstable with frequent dislodgement of elements and size variation, and never displaying the long stable periods that were frequently observed for non-branched debris. Furthermore, the packing density (defined as the ratio of the solid volume and the overall volume) of jams formed by branched debris was significantly smaller than the packing of jams formed with non-branched sticks. Qualitative observations indicate that this trend depends on the dimensionless ratio b/L (i.e. visual inspections indicates that B3 experiments displayed higher porosities than B2).

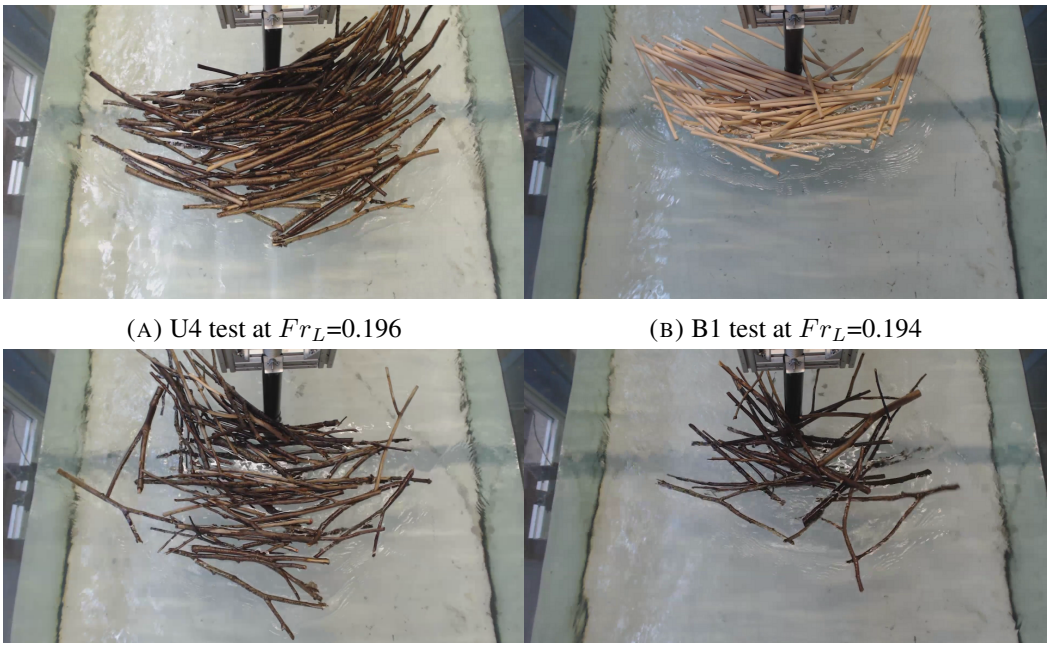

(A) U4 test at Fr_L=0.196 (B) B1 test at Fr_L=0.194

(C) B2 test at Fr_L=0.191 (D) B3 test at Fr_L=0.196

FIGURE 4.12: Examples of accumulations before the jam failure, during experiments with non-branched debris (4.12a), debris jams formed by dowels in group B1 (4.12b), branched in group B2 (4.12c), and branched in group B3 (4.12d) for similar Fr_L and equal length and diameter of debris pieces.

Figure 4.13 shows the maximum width, depth, and length (made dimensionless by L) reached by accumulations formed during experiments of groups B1, B2, and B3 as a function of Fr_L and overlapped to the experimental results for non-branched debris. At the lowest range of Fr_L (e.g. for $Fr_L \leq 0.20$), jams formed by dowels (group B1) reach maximum dimensions comparable to those previously observed for natural non-branched debris, i.e. $\omega^c \approx 2.7\text{-}3.0$, $\eta^c \approx 0.2$, and $\kappa^c \approx 1.5$. However, at larger Fr_L the jam dimensionless width ω^c, and length κ^c drop significantly compared to the corresponding values obtained with natural sticks. At the highest range of Fr_L, the values of ω^c, η^c, and κ^c are approximately 1.1, 0.25, and 0.2, respectively. Visual observations at these flow regimes revealed that both individual and bunch of elements were less likely to be entrapped by the forming debris jam, suggesting that interlocking and frictional forces were smaller than in jams formed by natural sticks.

The maximum size reached by branched jams (groups B2 and B3) also displays important differences compared to non-branched sticks. Figure 4.13 shows that for $Fr_L < 0.20$ jams formed by branched sticks can be significantly narrower (up to 35% less) than jams made of non-branched elements. For example, at low Fr_L jams of group B3 showed a maximum dimensionless width ω^c of approximately 1.9, whereas values for non-branched sticks ranged between 2.5 and 3.2. Although this difference is more clearly observed for ω^c, the same tendency (albeit less marked) also holds true for η^c and κ^c, with the latter being the least affected. With increasing values of Fr_L, differences in ω^c for non-branched and branched debris are reduced to approximately

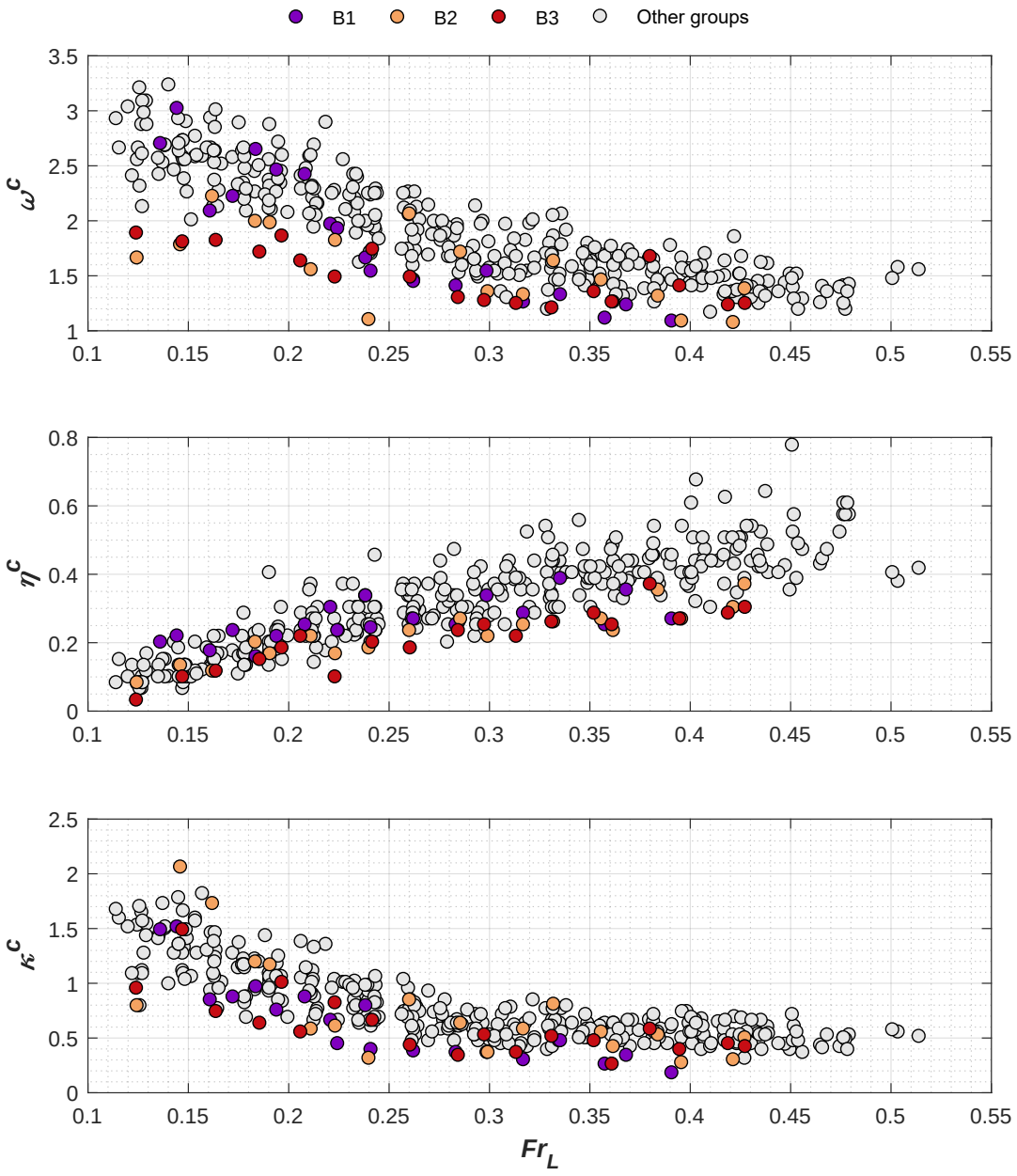

FIGURE 4.13: Values of the dimensionless (top to bottom) width ω^c, height η^c, and length κ^c against Fr_L (horizontal axis) for experimental groups B1 (dowels), B2 (small branches), and B3 (large branches) and compared to standard uniform length sticks used for other experimental groups.

20%. Differences between jams formed by debris elements with branches of different length (i.e. groups B2 and B3) are less pronounced than with non-branched elements, although the values of ω^c in B3 are in general smaller than those of B2.

4.4.4 Pier Diameter

The influence of the pier width (i.e. pier diameter for circular piers) on the critical dimensions of the debris accumulations was tested by the dimensionless variable L/D. Figure 4.14 shows the maximum size of debris jams for experimental groups U1 to U5. Although L/D was varied between 3.75 (group U1) and 15 (group U5) for uniform debris, values of ω^c, η^c, and κ^c are all clustered within a narrow band. Likewise, for non-uniform debris L/D varied between 5 (group N1) and 30 (group N13) In other words, for a given size of debris the influence of the pier diameter D on the accumulation size is negligible within the range of values of L/D tested in this study.

4.4.5 Pier Nose Shape

Figure 4.15 shows the maximum size of accumulations as a function of Fr_L for groups P1 to P5, along with the data for circular piers. Overall, these results for ω^c and κ^c of all tests lie on the same scatter band previously obtained for a circular pier, except for square piers, which resulted in slightly wider and longer debris accumulations. The depth of accumulations formed at all pier shapes lie on the same band, and no significant differences can be attributed to any particular shape. At the lowest values of Fr_L tested (i.e. say, $0.12 \leq Fr_L \leq 0.15$), ω^c for experiments in groups P2-P5 ranged between 2.4$\sim$3.1, η^c between 0.04$\sim$0.08, and κ^c between 1.2$\sim$1.6, all of which falling within the range of scatter of results obtained with circular piers. For increasing Fr_L, ω^c and κ^c decrease, whereas η^c increases. Around the highest value of Fr_L studied in this work (i.e. $Fr_L \approx 0.42$) ω^c for P2-P5 ranges between 1.4$\sim$1.9, η^c between 0.35$\sim$0.55, and κ^c between 0.50$\sim$0.90.

Varying the shape of the pier had only minor or negligible effects on the formation and maximum size of large wood piles. Qualitatively, jams accumulated on piers of groups P1 to P5 showed consistency with those formed at a circular pier. No substantial differences were observed with regards to this formation process, with the exception for piers with flat surfaces (i.e. square in group P1 and trapezoidal in P4). These groups were typically more efficient in recruiting debris at the early stages of the jam formation, which reduced the duration of the *unstable* phase. However, the results provided in this study show that the shape of the pier has only a minor influence on the final, maximum dimensions of formed jams.

4.4.6 Flow Depth

The influence of the dimensionless depth h/L was also tested. In tests H1 to H3 three different values of h/L (namely 0.783, 0.986 and 1.195) were kept approximately constant for each group and are plotted in Figure 4.16 compared to the other experimental groups for uniform debris

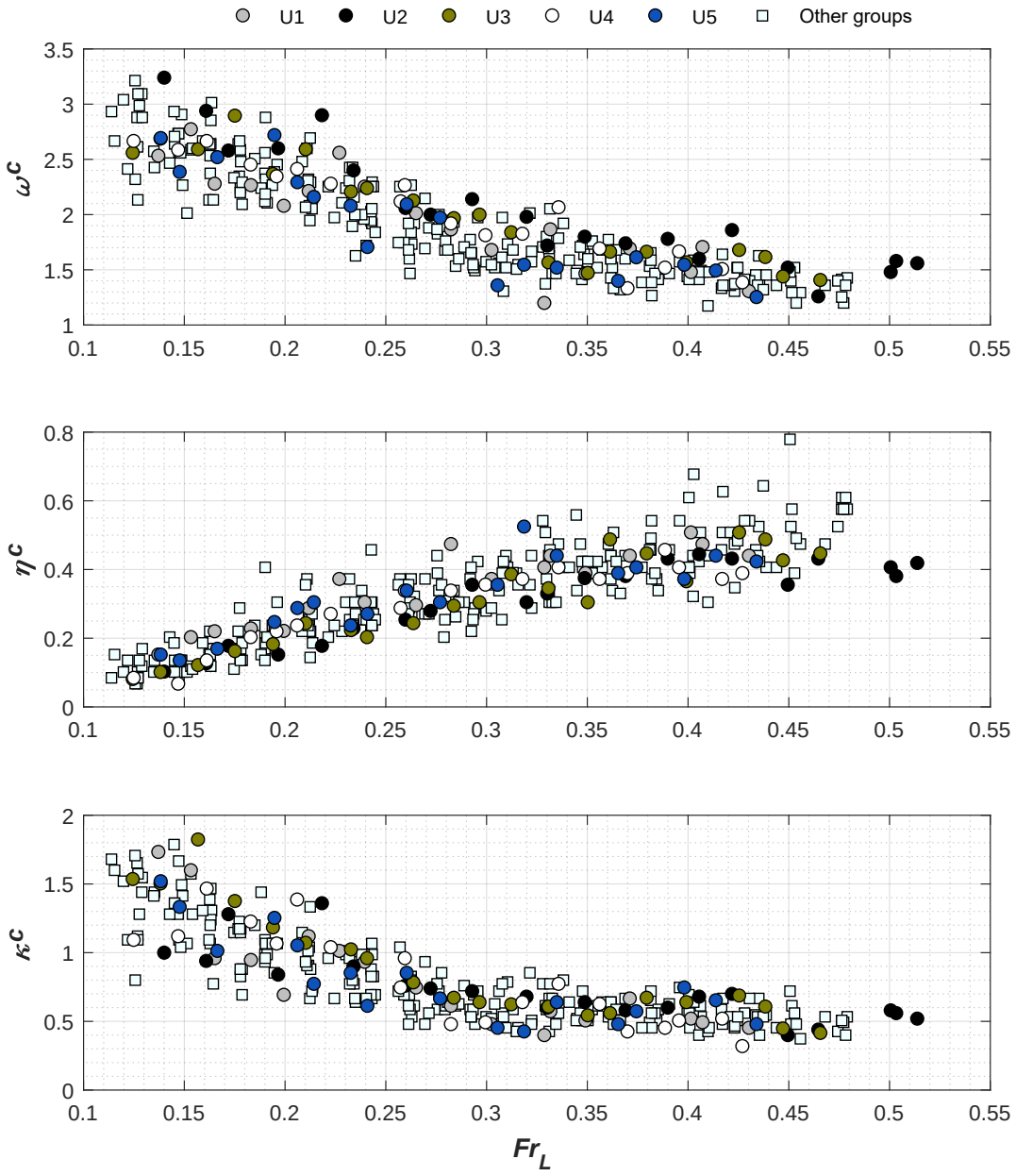

FIGURE 4.14: Values of the dimensionless (top to bottom) width ω^c, height η^c, and length κ^c against Fr_L (horizontal axis) for experimental groups U1 (L/D=3.75), U2 (L/D=5), U3 (L/D=6.25), U4 (L/D=7.5), and U5 (L/D=15) and compared to groups D, H and T (in light blue).

elements. No clear difference in the values of ω^c, η^c, and κ^c was observed across tests with different values of h/L. All values of ω^c, η^c, and κ^c follow the same trend and data points are not indicating any significant influence of h/L.

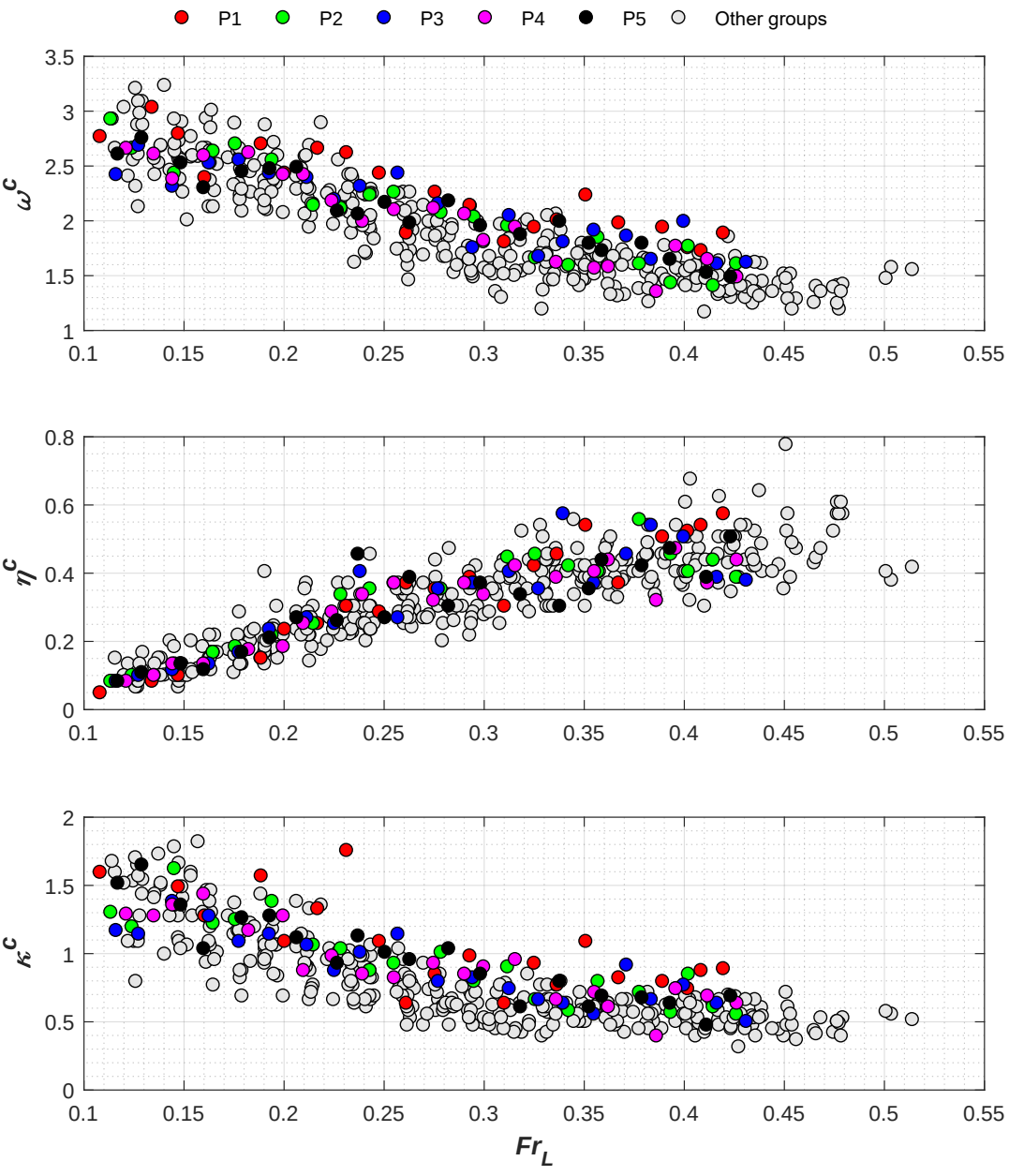

FIGURE 4.15: Values of the dimensionless (top to bottom) width ω^c, height η^c, and length κ^c against Fr_L (horizontal axis) for experimental groups P1 (square pier), P2 (triangular pier), P3 (ogive pier), P4 (trapezoidal pier), and P5 (half-circle pier) and compared to groups U, D, H, and T (in light blue).

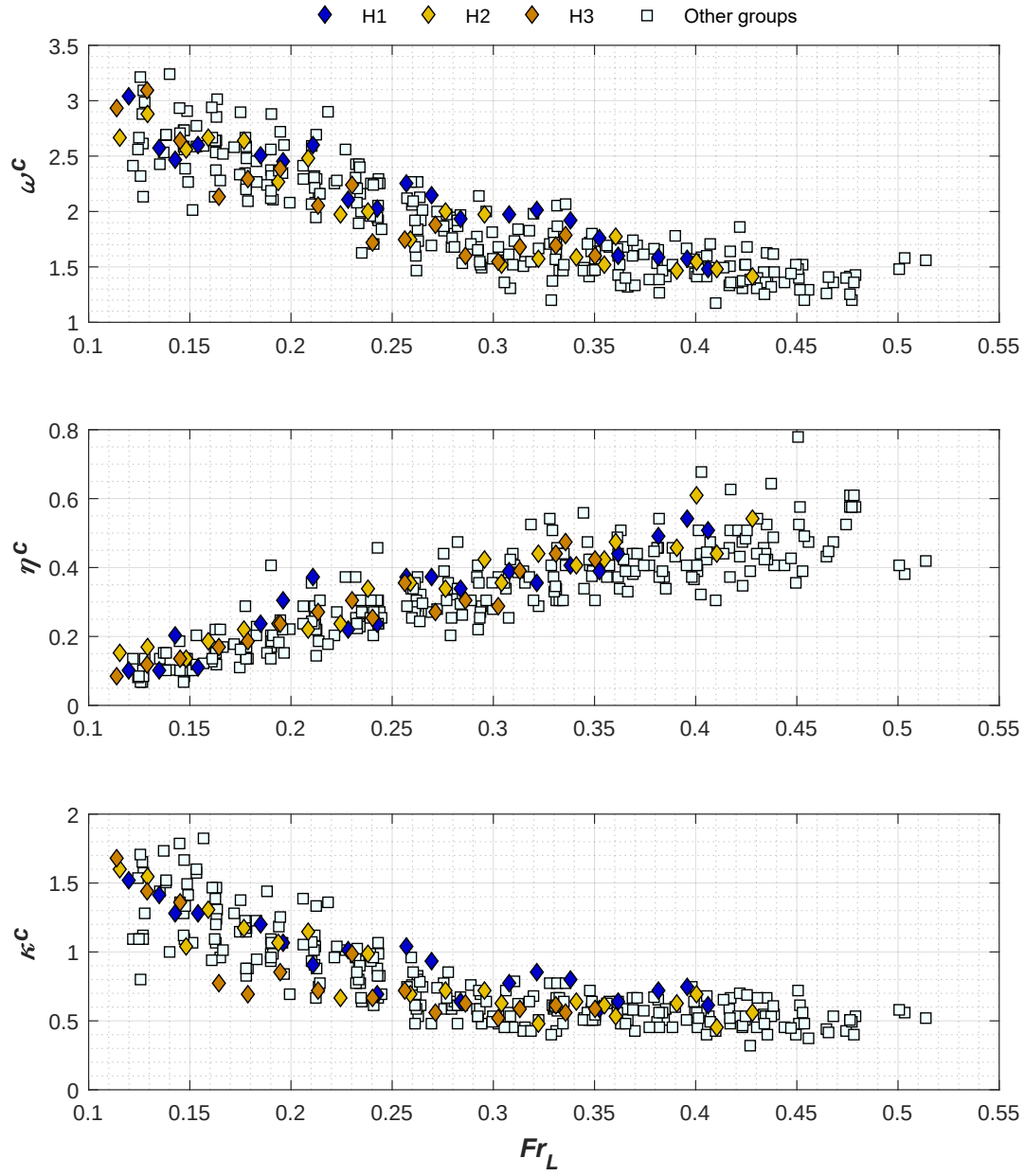

FIGURE 4.16: Values of the dimensionless (top to bottom) width ω^c, height η^c and length κ^c against Fr_L (horizontal axis) for experimental groups H1 (h/L=0.783), H2 (h/L=0.986), and H3 (h/L=1.195) and compared to groups U, D and T (in light blue).

4.5 Analysis and Discussion

The results from the experiments presented in this thesis provide important insights into the phenomena of debris accumulations at bridge piers. A detailed analysis and discussion is provided in the next sections.

4.5.1 Formation and Failure of Debris Jams

The evolution of debris accumulations at bridge piers is halted when a critical size is reached, after which a failure mechanism was observed in all tests. In addition, during all tests the dimensions of the accumulations at this critical condition were either highest or close to highest. This provides an opportunity to define variables that for practical purposes represent the maximum dimensions that these accumulations can reach under given conditions of flow and a continuous supply of debris of given length. Previous studies on woody debris accumulations at bridges have not investigated the entire jam lifetime and therefore have not reported this key behaviour. In particular, the accumulation process has only been studied marginally in the laboratory by Lyn et al. (2003). However, a field survey by Lyn et al. (2007) noted that a few accumulations disappeared at some point, and in one case they proposed that the debris jam could have been disengaged from the pier and then transported and accumulated again downstream at another bridge pier. The experimental results presented in this work provide strong evidence supporting this observation. The shape observed during the experiments was also consistent with field observations by Diehl (1997); Abbe and Montgomery (2003); Lagasse et al. (2010). Namely, the shape of the jams formed in all of the experiments shown in this work resembled a half-cone, with only minor deviations observed.

The experimental results reported in this thesis have shown that failure always occurred when accumulations were asymmetric and through a rotation towards the widest side. This suggests that failure is caused by a shift in the centre of application of the drag force from the pier axis towards the widest side. The observed values of the asymmetry factor ψ indicates that only a relatively small asymmetry is needed to drive failure (on average, failure was observed when the largest semi-width was approximately 17% greater than the smallest). Values of ψ below 1.1 are rare, confirming that when the accumulation is almost or perfectly symmetrical (i.e. $\psi \approx 1$) failure is unlikely. On the other hand, lack of ψ values over 1.5 indicates that at these values cannot be formed because the failure rotation takes place before they can be reached. The idea that jam failure is governed by forces induced by asymmetry is analysed in detail in chapter 5.

4.5.2 Maximum Size Estimation

The comparison of the size of accumulations that are formed by uniform and non-uniform debris has unveiled important differences. Although both show the same qualitative behaviour, experiments with debris of uniform length produce accumulations that are considerably larger than those formed with a log-normal distribution of lengths having the same maximum length. This indicates that idealised laboratory tests with uniform size debris may not correctly represent real-world processes that take place in natural environments, where debris is typically non-uniform. One exception to this rule may occur when the main supply of debris to the river

comes from human activities that can produce more uniformly distributed sizes, such as logging. In spite of these considerations, uniform debris offer less complex experimental conditions that can be advantageous in the development of a mechanistic explanatory theory for the processes observed in these experiments. It is also interesting to observe that the value of ω=1 proposed by Diehl (1997) based on field observations falls within the experimental results conducted with non-uniform debris (ω^c=1 for $Fr_L \approx 0.25$). However, the same results show that ω^c can reach values approximately between 0.8 and 1.4 depending on Fr_L.

The experiments in this work on both uniform and non-uniform debris reveal clear relations between the three variables characterising the geometry of accumulations ω^c, η^c, κ^c and Fr_L. Furthermore, results clearly indicate that the length of individual debris elements L is key for determining the potential size reached by LWD piles, as previously suggested by field observations (Diehl, 1997). Results also showed that for practical purposes, the maximum size of the jam can be assumed independent of L/D, d/L, and h/L within the range of values tested in these experiments. For instance, the dimensionless group d/L displayed only modest effects on the dimensions of the accumulations. The dimensionless water depth h/L showed no influence on the geometry of the LWD accumulations, confirming observations by Lyn et al. (2003) that for h sufficiently high (e.g. no interactions with the bed), its effects on the debris jam growth are null. Lyn et al. (2003) observed that this variable can have an influence on the accumulation process at shallow depths, in which case the accumulation would get anchored to the river bed. In this study, all tests were performed with enough water depth to prevent any interaction between debris and flume bed. Likewise, pier diameter D and debris length L were varied resulting in a wide range of the L/D variable, but no noticeable influence on the geometry of the formed accumulations was observed. As a result, for the range of conditions analysed in this study the influence of d/L, h/L, and L/D is minimal and can be neglected from the functional relation (3.3). Similar considerations are partially applicable to the dimensionless debris density ρ_L/ρ. While ρ_L/ρ has no effects on ω^c and κ^c, its influence on η^c is important as for the highest debris density the accumulation depth was significantly higher than other tests with smaller ρ_L/ρ values. In the following analysis, this influence of ρ_L/ρ on η^c is neglected, and as a consequence, these results are strictly valid only for values of ρ_L within the experimental range of 450-550 kg/m^3. The experimental results shown in this thesis have also confirmed the isolated pier assumption adopted previously. Figure 4.17 shows the width blockage ratio W^c/B for all experimental tests. The values of this ratio were $0.23 < W^c/B < 0.67$ in most (90%) experiments. Higher values of W^c/B were formed only in a few tests (i.e. $0.67 < W^c/B \leq 0.87$ in only 10% of the experiments), but even within this higher range no substantial differences in the dimensionless variables ω^c, η^c, and κ^c have been observed for different W^c/B values. For example, at low Fr_L in figure 4.7, results for groups $U1$, $U2$, $U3$, and $D3$ display similar values of ω^c=W^c/L despite substantially different values of W^c/B across these points. The amount of data at high values of W^c/B is however limited and further tests are needed to determine the influence of this variable on the dimensions of debris accumulations (i.e. for non-isolated piers).

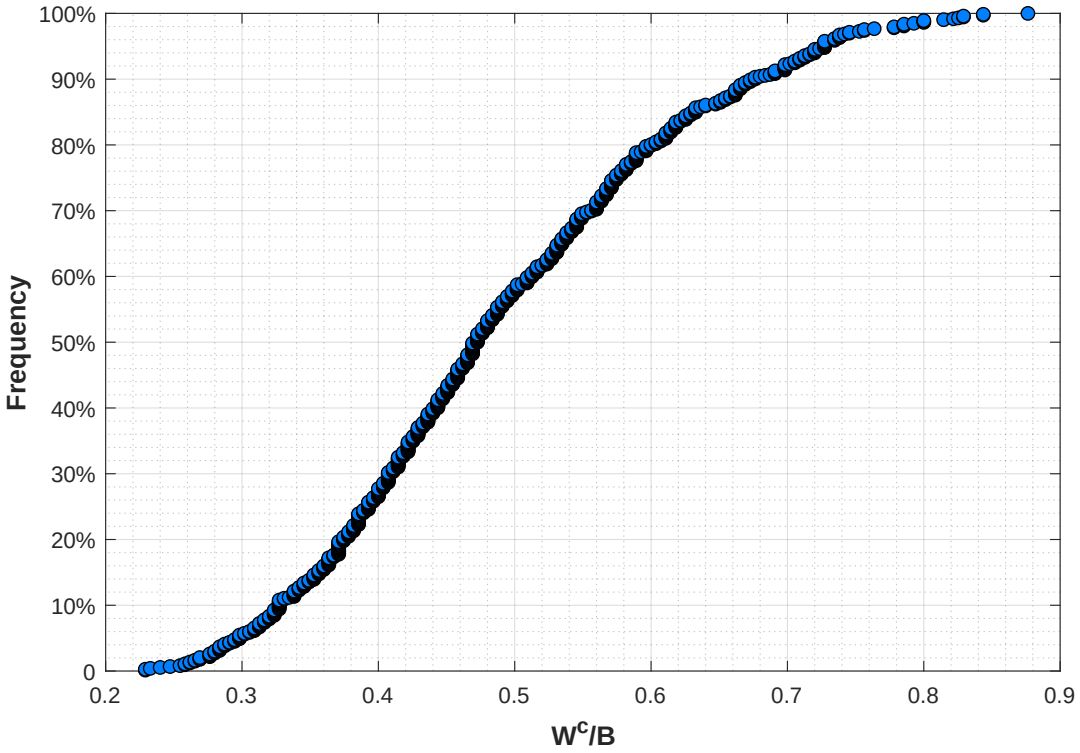

FIGURE 4.17: Frequency of occurrence of the width blockage ratio W^c/B for all experimental tests.

Under the above assumptions and further assuming that ω^c, η^c, and κ^c are mutually independent, the functional relation (3.3) can be simplified as

$$\mathbf{G} = \mathbf{F}(Fr_L) \tag{4.1}$$

where $\mathbf{G} = [\omega^c, \eta^c, \kappa^c]^T$ is the vector representing the critical geometry of the accumulation and $\mathbf{F} = [f_1(Fr_L), f_2(Fr_L), f_3(Fr_L)]^T$ is the vector function. Equation (4.1) enables predictions of the potential dimensions of debris accumulations to be made as a function of the length of debris supplied from upstream and the approach flow velocity. This assumes that the accumulation is 'supply unlimited', - i.e. the river or stream provides enough floating debris for the processes observed in these experiments to develop - and that the hydrological event is long enough for a jam critical stage to be reached. Therefore, this represents a worst-case scenario that can be useful to assess horizontal loadings and afflux under extreme conditions. The results of the regression analysis of the data presented on Figures 4.7 yields the following three components of $\mathbf{F}$:

$$\begin{aligned}
\omega^c &= 0.988 + 3.238e^{-4.625Fr_L}, \\
\eta^c &= 0.703 - 0.887e^{-3.004Fr_L}, \\
\kappa^c &= 0.466 + 3.720e^{-9.936Fr_L}. \quad \text{for } 0.11<Fr_L<0.51
\end{aligned} \tag{4.2}$$

The corresponding regression of the non-uniform length debris results in:

$$\begin{aligned}
\omega^c &= 0.774 + 0.939e^{-6.139Fr_L}, \\
\eta^c &= 0.394 - 0.458e^{-5.770Fr_L}, \\
\kappa^c &= 0.246 + 1.178e^{-15.039Fr_L}. \quad \text{for } 0.10<Fr_L<0.40
\end{aligned} \tag{4.3}$$

A plot of these regressions is shown in Figure 4.18, fitting the experimental data with (4.2) and (4.3).

A further analysis has been carried out in order to assess whether correlation is strong and results are significant. Since the proposed equations are non-linear, regressions in (4.2) and (4.3) and data from Figure 4.7 have been mapped onto the plane $Fr_L \rightarrow e^{-cFr_L}$ where c is the parameter used for each of the regressions. This mapping linearises the regression curves i.e. they become straight lines and allow computation of correlation coefficients against observed data. Figures 4.19 and 4.20 show (for uniform and non-uniform debris respectively) these functions in the linearised space and the fitting of the data. The values of the coefficient of determination R^2 for equations (4.2) in the mapped space were 0.82, 0.79, and 0.77 for ω^c, η^c and κ^c respectively, which suggest a very strong correlation. The corresponding values of R^2 found for the non-uniform tests from equations (4.3) were 0.60, 0.69, and 0.45, which indicate a moderately strong correlation for ω^c and η^c and a moderate correlation for κ^c. A p-value test carried out for each variable yielded p-values well below the significance level of α=0.01 in any case, which suggests that results are statistically significant.

These regressions can be regarded as a first attempt for estimating potential dimensions of LWD accumulations at bridge piers. While equations (4.2) and (4.3) both display similar trends, uniform length debris produce jams that are substantially larger than those formed by non-uniform elements. In most real-world situations, (4.3) should be used to model a woody debris accumulation. However, (4.2) could be adopted to simulate certain scenarios involving the supply of debris of approximately uniform length (e.g. in areas subject to logging or harvesting) or as a more conservative estimate. An analysis of (4.2) and (4.3) under the two scenarios is shown in Appendix D, based on the historical event of Charles' Bridge collapse in Prague during the 1890 flood due to the accumulation of a very large LWD jam. It is important to highlight that the relations above have been derived from experiments conducted in a straight prismatic flume in which the pier was located at the centre of the rectangular cross section. Therefore, strictly

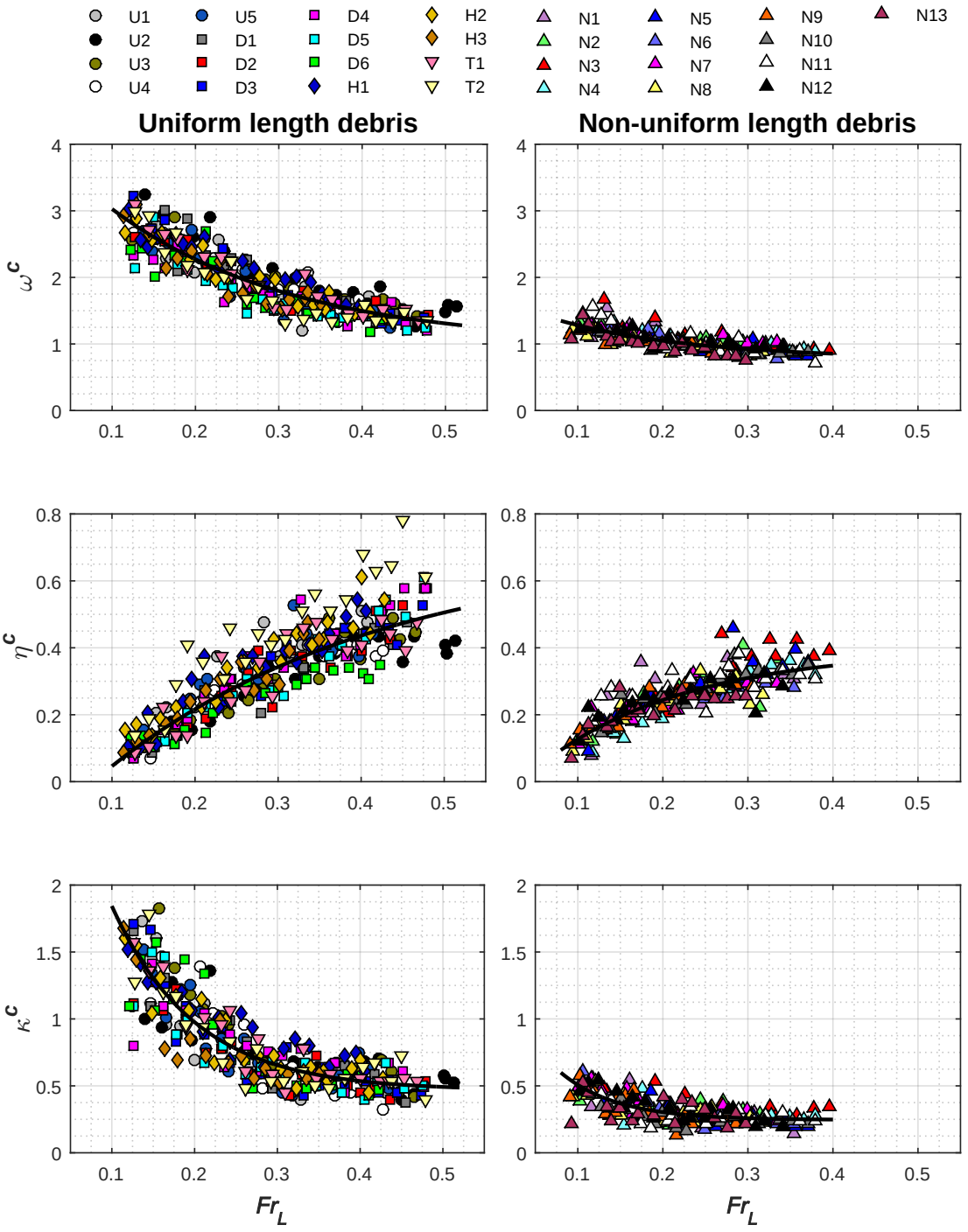

FIGURE 4.18: Fitting (black curve) of regressions in (4.2) and (4.3) with experimental data for both uniform and non-uniform debris.

speaking equations (4.2) and (4.3) are only valid under similar conditions. Flow in rivers can display complex patterns such as secondary currents that are likely to influence the processes of formation, growth and failure of debris jams at piers. It is unclear how these effects will influence the critical dimensions of accumulations formed under these conditions.

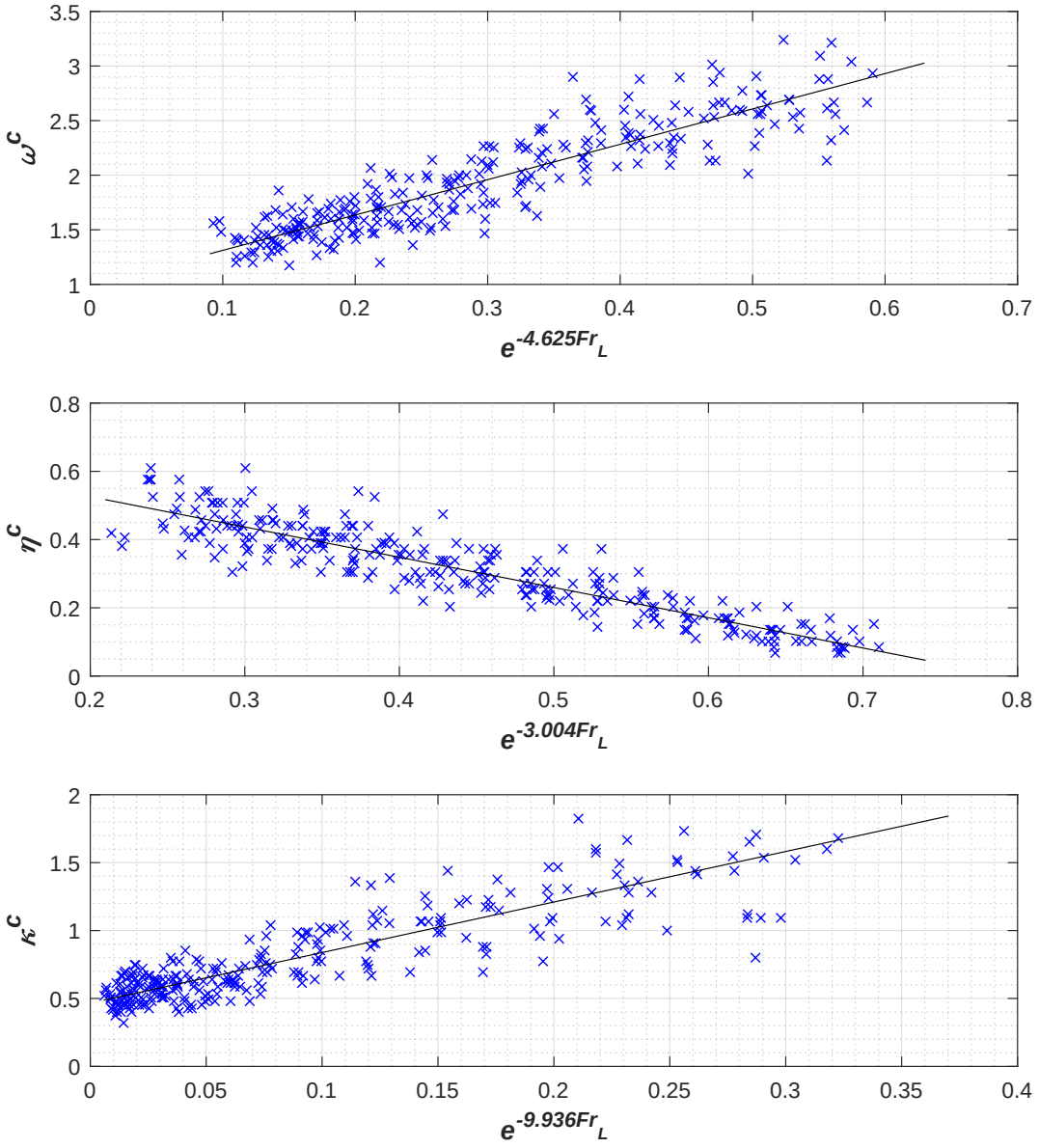

FIGURE 4.19: Plot of regressions (4.2) with experimental data mapped onto a linearised space for all dimensionless geometric values.

A statistical analysis has been carried out on experimental data of groups B1, B2, and B3 in order to assess whether values are significantly different from the data of jams formed by natural sticks or not. Since the sample size of these groups is considerably smaller than the combined size of the other groups, a Welch's t-test was carried out for each of the maximum size variables (i.e. ω^c, η^c, and κ^c) for each experimental group. Data from group B1 was only assessed for values of $Fr_L \geq 0.20$, since it was shown in figure 4.13 that observations below that value of Fr_L were consistent with natural stick jams. The resulting p-values for group B1 at $Fr_L \geq 0.20$ were below the significant level of α=0.01 for all jam size variables, suggesting that the size of jam formed by dowels is significantly different from those formed by natural sticks. Likewise,

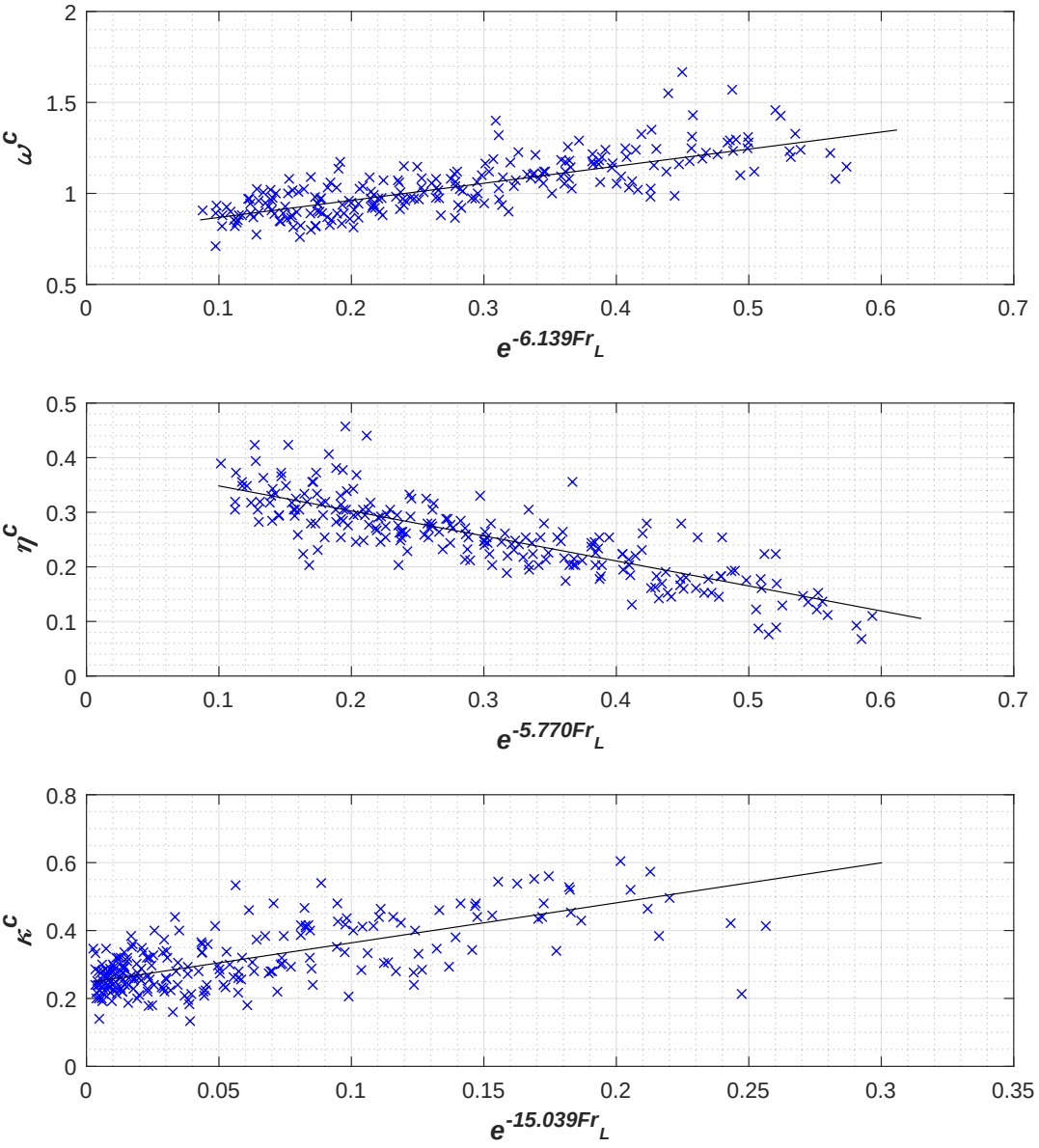

FIGURE 4.20: Plot of regressions (4.3) with experimental data mapped onto a linearised space for all dimensionless geometric values.

test for groups B2 and B3 revealed that the resulting p-values were substantially smaller than the significance level of α=0.01 for ω^c and η^c, whilst this was not observed for κ^c, in which case the resulting p-value is 0.101, suggesting that the length of jams formed with branched debris is not significantly different than those formed with natural unbranched sticks. This is consistent with the observations in figure 4.13, whereby κ^c was deemed less affected by branched elements.

4.5.3 Drag Coefficient of Accumulated Jams

The analysis of the drag coefficient presented in Figure 4.9 completes the set of variables necessary to determine the drag force exerted on a debris jam. In this work, the large majority of C_{Dd} values is gathered between 1 and 2. These results are consistent with other preliminary works described in section 2.2.3.1. For example, Parola et al. (2000) experimentally examined the forces that can be exerted by LWD on a pier in laboratory tests using different jam models (flat plates, solid cones and model debris elements), in which C_D varies broadly between just over 0 and 2. The present study provides further evidence and a substantially larger data set than Parola et al. (2000).

The values of the drag coefficient reported in this thesis should be used with caution. Parola et al. (2000) observed that C_{Dd} decreases with an increase in the blockage ratio (i.e. the ratio between the obstructed area and the free flow area) when this ratio exceeds 36%. In the present work, the values of the blockage ratio were much smaller (the maximum value was smaller than 20%), therefore representing the condition of an isolated pier. In addition, the dispersion observed in figure 4.9 highlights the difficulties in obtaining accurate and consistent predictions of C_{Dd} from laboratory experiments of debris accumulations. For example, an accurate measure of the frontal area was not always possible and could have led to large errors and the velocity approaching the pier-debris structure could be substantially different than the velocity in undisturbed conditions.

4.5.4 Factors Influencing Debris Jams Characteristics

The use of dowels to model natural woody debris in rivers (e.g. Rusyda et al., 2014; De Cicco et al., 2016; Gschnitzer et al., 2017) needs to be carefully re-considered for a number of reasons. First, dowel jams never formed for $Fr_L \geq 0.40$, which is lower than the maximum values of $Fr_L \approx 0.5$ for which an accumulation of natural sticks was experimentally observed to develop. In addition, accumulations formed by dowels are smaller than those formed by natural sticks, particularly when $Fr_L \geq 0.25$. Another difference was observed for the shape and disposition that debris assume. The regular structure displayed by the accumulation of dowels may not be representative of real-world jams that are formed by natural wood drifts, which - as field observations show - display a less regular shape. For these reasons, results reported in this thesis provide evidence in support of previous recommendations by Lyn et al. (2003), who suggested that use of dowels should be avoided for experimental studies on LWD accumulations.

Debris jams formed by branched sticks were significantly smaller and less stable than those formed by non-branched elements. This is counter-intuitive, as branches are expected to provide interlocking and therefore robustness to the accumulation. Here it is proposed a hypothesis

that would potentially explain this observed behaviour. The asymmetry between the two semi-widths on the left and right (W_L and W_R) has been previously observed to be a primary factor inducing the torque required to dislodge the debris jam from the pier. During the experiments presented in this work, it was qualitatively observed that during tests in groups B2 and B3, the planar asymmetry varied widely as new debris pieces were recruited. Namely, the widest side of the accumulation changed from one side to the other several times during the experiments. The reason for this behaviour is related to the higher porosity of jams formed by branched debris. High porosity values means that each element's contribution to increasing one semi-width is higher, leading to a more discontinuous growth and increased probability of large asymmetries being formed by chance, which causes the inherent instability of the branched debris jam. Further work is needed to study this hypothesis.

For practical purposes, natural non-branched sticks of uniform length appear to model the natural phenomena of the accumulation of woody debris at single piers more representatively than uniform length dowels. On the other hand, as discussed above, uniform length sticks used as debris elements still remain an approximation about the type of material transported in rivers and may not capture all the possible characteristics of real-world accumulations, e.g. as for the case of branched debris. Nevertheless, since the largest accumulations observed are formed with uniform length non-branched sticks, results from these experiments can be regarded as a worst-case scenario that is useful for practical engineering applications.

The results of the experiments with different pier shapes presented in this work shows that the pier shape does not substantially influence the dimensions of formed debris jams. The only exception to this rule was observed for squared piers, which displayed widths and lengths approximately 15% larger than the other groups. This last observation, combined with previous findings by De Cicco et al. (2016), who concluded that square piers are more likely to entrap debris elements, indicates that piers of square shape should be avoided in rivers where debris accumulations may occur. As a result, the regression shown in (4.2) and (4.3) for prediction of woody debris jams size can be applied without introducing any shape factor, in consideration of the highly similar data values obtained.

4.6 Conclusions

Experimental results shown in this work provide a detailed analysis of the whole life of debris accumulations at bridge piers including their formation, growth, and failure. The key-points observed from experimental analysis are:

- The growth of woody debris jams can be conceptualised into three phases classified as *unstable*, *stable*, and *critical* conditions. The unstable phase occurs at the beginning of the

recruitment process, when a debris framework is formed and the accumulation displays a rapid growth. During this phase individual debris elements are easily disengaged and drift downstream. Once a robust framework is formed, a stable phase is observed during which only moderate changes in the accumulation structure occur and the jam either stops from growing or grows at a slow pace. Finally, the critical phase denotes the terminal stage of a debris accumulation when an oscillatory rotational movement is observed, which eventually leads to the failure of the accumulation (i.e. complete removal from the pier).

- The failure phenomenon is ubiquitous and occurs for all experiments. Furthermore, in almost all tests the oscillations began when the size of the debris jam was maximum. Therefore, this failure condition can be used to define metrics to characterise the dimensions of potentially large accumulations.

- Results have shown a clear and strong dependency of the accumulation dimensions on the dimensionless parameter Fr_L=$v/\sqrt{gL}$. For all cases, at low values of Fr_L, dimensionless width ω^c and length κ^c are highest, while dimensionless height η^c is smallest. ω^c and κ^c were observed to decrease with increasing Fr_L, while η^c displayed the opposite trend.

- A comparison between the dimensions of debris jams formed with uniform and non-uniform distributions of the length of individual debris pieces has shown considerable differences between the two type of elements. Accumulations formed by single sized debris are notably larger than those formed by log-normally distributed debris of equal maximum length. This indicates that idealised experiments with uniform debris length will overestimate accumulations that are likely to be formed in the real-world, where debris is typically non-uniform in size, although this is not always true.

- The dimensionless pier size L/D, debris diameter d/L, and water depth h/L were observed to have negligible influence on the maximum size achieved by an accumulation within the studied range. Namely, values of ω^c, η^c and κ^c obtained in all experiments were clustered within a narrow band for values of L/D ranging from 3.5 to 30, d/L from 0.020 to 0.078, and h/L from 0.783 to 1.195. The relative debris density ρ_L/ρ had no influence on the width ω^c and length κ^c of the accumulations. However, experiments performed with the highest value of ρ_L/ρ resulted in accumulations that were up to 30% deeper than those formed with the lowest values of ρ_L/ρ.

- The size of the jams obtained from experiments with six different pier shapes revealed that the dimensions of the formed debris jams are not significantly influenced by the shape of the pier. A relatively minor exception to this was observed for the square shape. In this case, the maximum width of the accumulation was approximately 15% larger than the corresponding width found for accumulations with other shapes. Square piers were also observed to initiate the accumulation process more rapidly, although this has not been assessed quantitatively.

- Debris jams formed by dowels (i.e. perfectly cylindrical elements) tend to reach sizes that are comparable to those formed by natural sticks only for the lowest range of the debris

Froude number Fr_L. However, at the highest range of Fr_L, these jams can be up to 40% smaller than those formed by natural sticks. Moreover, dowel accumulations could not be formed for Fr_L>0.40. Under these conditions, elements were promptly removed from the pier by the flow, even if attempts were made to place them manually at the pier as a large bunch.

- Experiments with branched debris elements showed that branches play a significant role on the formation process. Accumulations of this kind were observed to be less stable than those formed by non-branched sticks, displaying frequent early failures and a continuous change of the jam shape. Furthermore, the maximum size reached by branched jams was significantly smaller than those formed by non-branched natural sticks, with differences up to 35% for ω^c, at the lowest range of Fr_L.

- A function to estimate the maximum size of a debris accumulation based on experimental data is provided in this work. Furthermore, an estimation of the drag coefficient of debris jams is shown. The values of C_D varied between 0.9 and 3.5. The drag coefficient together with the maximum size of the jam, may provide valuable applications to a number of practical uses, e.g. the effects of debris jams on upstream water levels during floods, as well as the estimation of horizontal loadings exerted by debris on piers.

Chapter 5

Theoretical Analysis

The experimental results observed in Chapter 4 provided the description of a crucial stage of woody debris accumulations at bridge piers, that is the dislodgement of these jams through an oscillatory motion once the maximum size has been reached. The ability to theoretically describe these events may provide fundamental insights into the stability of these jams. This chapter develops a simplified model that describes the motion of a conceptualised debris jam develops in presence of asymmetric geometry and under the effect of the sole drag force.

5.1 Model Construction

Consider the problem of the rotational motion of a porous half-conical body about a cylinder immersed in a predominantly unidirectional free-surface flow field. Further, it is assumed that the diameter of the cylinder is negligible compared to the size of the solid, so that the position of the pivot point is assumed not to change with the motion of the body. The geometry of the body, which generically reproduces the main characteristics observed in chapter 4, is described by the width W in the direction normal to the main flow, a longitudinal length K, and a depth H below the water surface, as shown in figure 5.1. In addition, the dimension ΔK is introduced to represent the downstream extension beyond the pivot point (hereafter referred to as *tail*). For simplicity, the tail length ΔK is assumed equal on both sides.

To describe the motion of the solid, two Cartesian frames of reference are adopted. In the first frame, x, y, and z denote the transverse, streamwise, and vertical coordinates, respectively. The second frame is defined by the coordinates x', y', and z' and is used to describe a rotation θ of the first frame about the vertical axis (z=z'). The coordinates of the edge of the debris body are denoted by x_e, y_e, and z_e (or x'_e, y'_e, and z'_e for the second frame of reference). A shape asymmetry is introduced by the condition $W'_- \neq W'_+$ (figure 5.1), where W'_- and W'_+ are, respectively, the smaller and larger semi-widths of the jam in the rotation frame and thus

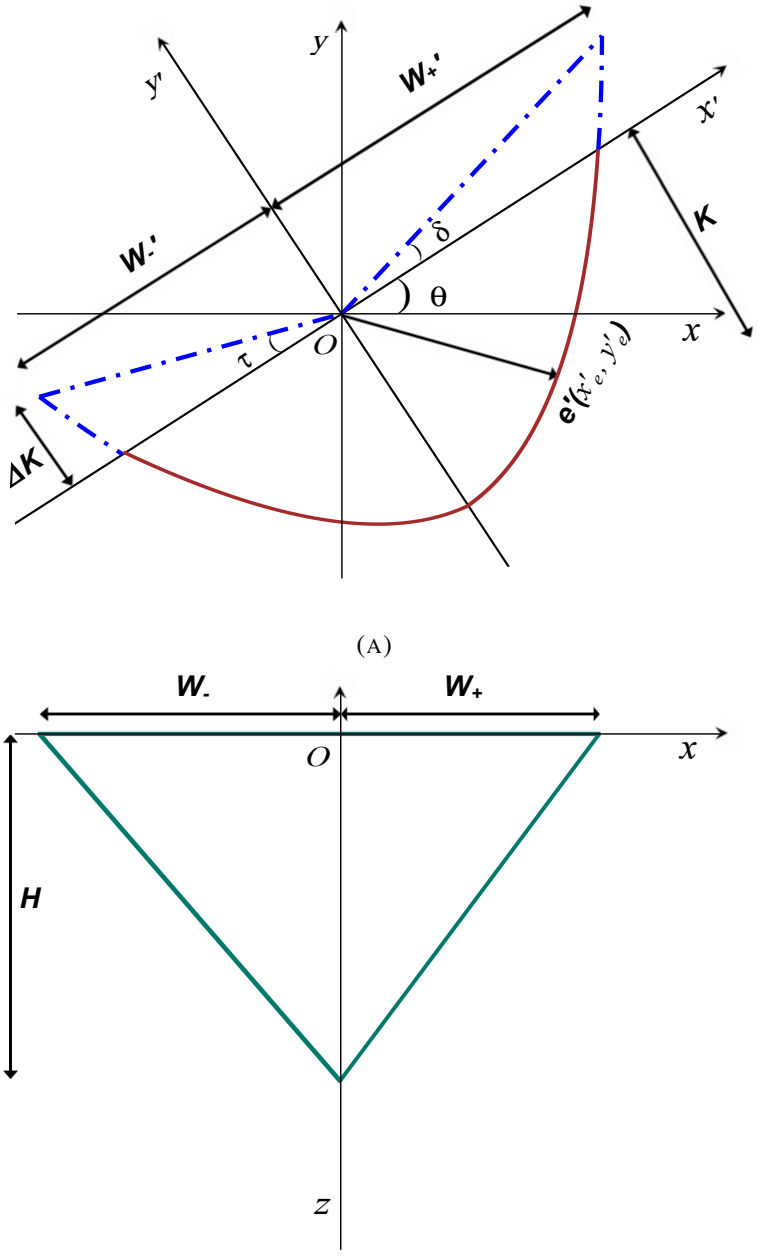

FIGURE 5.1: Conceptualised geometry of a debris jam at a pier. (A) and (B) show respectively the plan view and the maximum projected area of the jam for a given angle of rotation θ. It can be noted that in (B) $W_- > W_+$ being the projection of W'_- and W'_+.

by definition $W'_-<W'_+$. The rotational motion of the debris jam about the vertical axis can be modelled by the principle of conservation of angular momentum $I\ddot{\theta} = \Gamma$, where *I* is the moment of inertia of the debris body with respect to the axis of rotation z (which must include the added mass effect) and Γ is the torque of all external forces applied to the debris body. The proposed model assumes that drag $F_D = 0.5\rho C_D A v^2$, which is also assumed parallel to the streamwise direction, is the dominant force governing the rotational motion; where ρ is the water density, C_D the coefficient of drag, A the frontal area of the solid projected onto the $x-z$ plane and v the streamwise component of the average flow velocity. Other forces that take part in this process, such as friction between the pivot and solid, hydrostatic force difference between the upstream and downstream sides of the solid or the lift force, are neglected in the proposed model. The motion of the debris mass is assumed much slower than the flow velocity, so that its potential effects on the forces are also ignored in the model. In addition, it is assumed that drag is applied at the centroid of the cross-sectional area A. In essence, it is therefore postulated that the rotational motion is mainly governed by variations of the torque of drag induced by changes in A and the x position of its centroid x_c, which occur as a function of θ and the geometry of the solid (e.g. W'_+, W'_-, K, ΔK), which yields

$$I\ddot{\theta} = F_D x_c = \frac{1}{2}\rho C_D A v^2 x_c. \tag{5.1}$$

Equation (5.1), implies that for θ=0, a perfectly symmetrical solid (W'_-=W'_+) would remain static (Γ=0). From this stable condition, any asymmetry (i.e. $W'_-<W'_+$) or small rotation θ would lead to $x_c\neq 0$ and initiate the flow-solid dynamic interaction.

The geometry of the debris body (figure 5.1.b) is modelled by a piecewise second order polynomial describing the position **e'**=$[x'_e, y'_e]$ of the leading (i.e. upstream) boundary of the body at the free-surface:

$$\begin{aligned} y'_e &= \frac{K+\Delta K}{W'^2_-}x'^2_e - K && \text{for } x'_e \in \left(0,\ \pm W'_-\right) \\ y'_e &= \frac{K+\Delta K}{W'^2_+}x'^2_e - K && \text{for } x'_e \in \left(0,\ \pm W'_+\right) \end{aligned} \tag{5.2}$$

To account for the effect of asymmetry, the asymmetry factor is defined as

$$\psi = \frac{W'_+}{W'_-}, \tag{5.3}$$

therefore, horizontal planar asymmetry (i.e. $W'_+\neq W'_-$, also considering that $W'_+>W'_-$ by definition) implies $\psi>1$. Considering that W'_++W'_-=W, W'_-=$\frac{W}{1+\psi}$ and W'_+=$\frac{W\psi}{1+\psi}$, yields

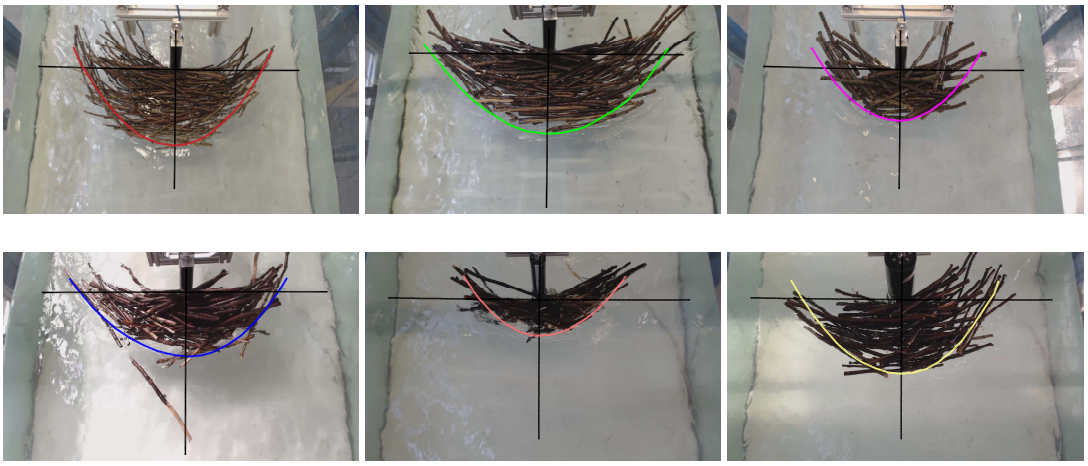

FIGURE 5.2: Examples of the curves used to model the shape of the accumulations. The background image shows debris accumulations obtained during the experiments analysed in section 4. The pier-jam contact point represents the origin of the x and y axes (solid black lines) as sketched in figure 5.1.

$$y'_e = \frac{(K+\Delta K)\,(1+\psi)^2}{W^2} x'^2_e - K, \qquad \text{for } x'_e \in \left(0,\ \pm W'_-\right)$$
$$y'_e = \frac{(K+\Delta K)\,(1+\psi)^2}{W^2\psi^2} x'^2_e - K. \qquad \text{for } x'_e \in \left(0,\ \pm W'_+\right) \tag{5.4}$$

Two dimensionless variables α=W/K and β=$\Delta K/K$ are introduced to describe the shape of the debris body and the relative size of the tail. Substituting α and β into (5.4) yields

$$y'_e = \frac{(1+\beta)\,(1+\psi)^2}{\alpha W} x'^2_e - \frac{W}{\alpha}, \qquad \text{for } x'_e \in \left(0,\ \pm W'_-\right)$$
$$y'_e = \frac{(1+\beta)\,(1+\psi)^2}{\alpha W\psi^2} x'^2_e - \frac{W}{\alpha}. \qquad \text{for } x'_e \in \left(0,\ \pm W'_+\right) \tag{5.5}$$

Figure 5.2 shows examples of how (5.5) can model the top geometry of debris jams formed at laboratory scale. Equation (5.5) is here used to define the expressions for the area A, centroid x_c, and moment of inertia I. Since A and x_c depend on the projection of **e'** onto the $x-z$-plane (see figure 5.1), they change with the rotation of the debris body. The area A and the position of its centroid x_c are obtained by determining the maximum values of the projection **e=Re'** of **e'** onto the x axis (herein referred to as W_- and W_+, respectively) within the domain -$\pi/2 \leq \theta \leq \pi/2$, where **R** is the rotation matrix and **e'** is defined by (5.5). Since only the first component of **e** is of concern to this work:

$$x_e(x'_e,\theta)=\begin{cases} x'_e\cos\theta-\frac{(1+\beta)(1+\psi)^2}{\alpha W}x'^2_e\sin\theta+\frac{W}{\alpha}\sin\theta & \text{for } x'_e\in\left(0,\ \pm W'_-\right)\\ x'_e\cos\theta-\frac{(1+\beta)(1+\psi)^2}{\alpha W\psi^2}x'^2_e\sin\theta+\frac{W}{\alpha}\sin\theta & \text{for } x'_e\in\left(0,\ \pm W'_+\right)\end{cases} \tag{5.6}$$

For low absolute values of the angle of rotation ($\theta_t^-\leq\theta\leq\theta_t^+$), the optima of (5.6) is given by $[W_-,W_+]=[x_e(W'_-,\theta),x_e(W'_+,\theta)]$, which for $W'_-<W'_+$ yields

$$\begin{aligned} W_-(\theta)&=\frac{W}{(1+\psi)\cos(\tau)}\cos(\theta-\tau), && \text{for } \theta_t^-\leq\theta\leq\pi/2\\ W_+(\theta)&=\frac{W\psi}{(1+\psi)\cos(\delta)}\cos(\theta+\delta). && \text{for } -\pi/2\leq\theta\leq\theta_t^+\end{aligned} \tag{5.7}$$

where θ_t^- and θ_t^+ are the limit angles for which the maximum projection of x'_e onto x is no longer given by the projection of W'_- and W'_+ respectively, and:

$$\begin{aligned}\tau&=\arctan\left(\frac{\beta(1+\psi)}{\alpha}\right),\\ \delta&=\arctan\left(\frac{\beta(1+\psi)}{\alpha\psi}\right),\end{aligned} \tag{5.8}$$

are the angles formed by the two tails of the jam with the x'-axis, as shown in figure 5.1.

On the other hand, if $\theta>\theta_t^+$ or $\theta<\theta_t^-$, the optima of (5.6) may occur within the interval $-W'_-<x'_e<W'_+$, in which case it can be defined by:

$$\frac{dx_e}{dx'_e}=\begin{cases}\cos\theta-\frac{2(1+\beta)(1+\psi)^2}{\alpha W}x'_e\sin\theta=0 & \text{for } x'_e\in\left(0,\ \pm W'_-\right)\\ \cos\theta-\frac{2(1+\beta)(1+\psi)^2}{\alpha W\psi^2}x'_e\sin\theta=0 & \text{for } x'_e\in\left(0,\ \pm W'_+\right)\end{cases} \tag{5.9}$$

Solving (5.9) for x'_e yields

$$x'_e=\begin{cases}\frac{1}{\tan\theta}\frac{\alpha W}{2(1+\beta)(1+\psi)^2} & \text{for } x'_e\in\left(0,\ \pm W'_-\right)\\ \frac{1}{\tan\theta}\frac{\alpha W\psi^2}{2(1+\beta)(1+\psi)^2} & \text{for } x'_e\in\left(0,\ \pm W'_+\right)\end{cases} \tag{5.10}$$

substituting (5.10) into (5.6) for $\theta>\theta_t^+$ or $\theta<\theta_t^-$ yields

$$\begin{aligned} W_-(\theta)&=\frac{\cos^2\theta}{\sin\theta}\frac{\alpha W}{4(1+\beta)(1+\psi)^2}+\frac{W}{\alpha}\sin\theta,\\ W_+(\theta)&=\frac{\cos^2\theta}{\sin\theta}\frac{\alpha W\psi^2}{4(1+\beta)(1+\psi)^2}+\frac{W}{\alpha}\sin\theta.\end{aligned} \tag{5.11}$$

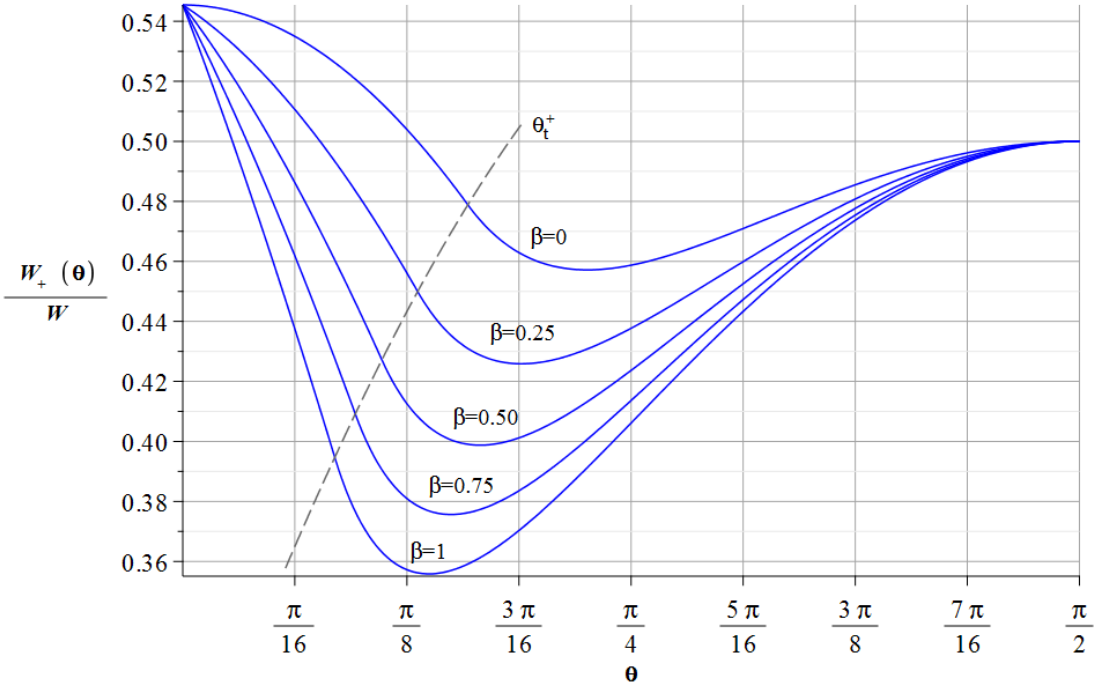

FIGURE 5.3: Plot of the normalised W_+ according to (5.7) and (5.11) (indicating also θ_t^+ as a convolved function) for fixed values of α=2, ψ=1.2 and varying β.

Figure 5.3 displays the normalised W_+ - i.e. the ratio between W_+ in (5.7) and (5.11) and W - projected onto the x-axis for arbitrary values of α and ψ varying β. The figure shows that W_+ decreases with the rotation for then increasing again, whilst larger tails result in smaller values of W_+.

At θ=θ_t^- and θ=θ_t^+, the values of respectively W_- and W_+, given by (5.11) and (5.7), must coincide. Combining these equations yields:

$$\begin{aligned} \theta_t^- &= -\arctan\left[\frac{\alpha}{2\,(1+\beta)\,(1+\psi)}\right], \\ \theta_t^+ &= \arctan\left[\frac{\alpha\psi}{2\,(1+\beta)\,(1+\psi)}\right]. \end{aligned} \tag{5.12}$$

The geometrical variables x_c and A can be now be obtained from (5.11) and (5.7). The projected area A is a triangle of height H and base $W_+(\theta)$+$W_-(\theta)$:

$$A(\theta) = \frac{(W_+(\theta) + W_-(\theta))\,H}{2}. \tag{5.13}$$

Thus, from (5.7) and (5.11):

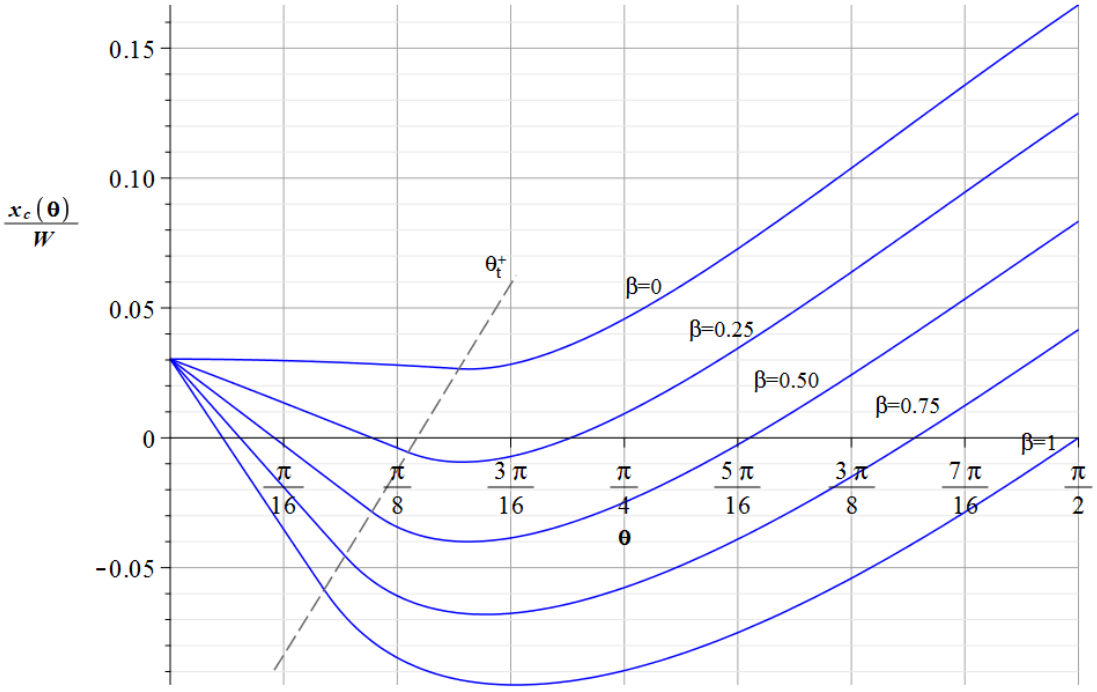

FIGURE 5.4: Plot of the normalised x_c according to (5.16) (indicating also θ_t^+ as a convolved function) for fixed values of α=2, ψ=1.2 and varying β.

$$A(\theta) = \begin{cases} \frac{WH}{2}\left[\frac{\alpha}{4(\psi+1)^2(1+\beta)}\frac{\cos^2\theta}{\sin\theta} + \frac{\sin\theta}{\alpha} + \frac{\psi}{\psi+1}\frac{\cos(\theta+\delta)}{\cos(\delta)}\right] & \text{for } -\frac{\pi}{2}\leq\theta<\theta_t^- \\ \frac{WH}{2(\psi+1)}\left[\psi\frac{\cos(\theta+\delta)}{\cos(\delta)} + \frac{\cos(\theta-\tau)}{\cos(\tau)}\right] & \text{for } \theta_t^-\leq\theta\leq\theta_t^+ \\ \frac{WH}{2}\left[\frac{\alpha\psi^2}{4(\psi+1)^2(1+\beta)}\frac{\cos^2\theta}{\sin\theta} + \frac{\sin\theta}{\alpha} + \frac{1}{\psi+1}\frac{\cos(\theta-\tau)}{\cos(\tau)}\right] & \text{for } \theta_t^+<\theta\leq\frac{\pi}{2} \end{cases} \tag{5.14}$$

Since the projected cross-section is a triangle, the centroid in the x-coordinate is defined as:

$$x_c(\theta) = \frac{W_+(\theta) - W_-(\theta)}{3}. \tag{5.15}$$

Substituting (5.7) and (5.11) into (5.15), the x-coordinate of the centroid may be written as

$$x_c(\theta) = \begin{cases} \frac{W}{3}\left[\frac{\psi}{\psi+1}\frac{\cos(\theta+\delta)}{\cos(\delta)} - \frac{\alpha}{4(\psi+1)^2(1+\beta)}\frac{\cos^2\theta}{\sin\theta} - \frac{\sin\theta}{\alpha}\right] & \text{for } -\frac{\pi}{2}\leq\theta<\theta_t^- \\ \frac{W}{3(\psi+1)}\left[\psi\frac{\cos(\theta+\delta)}{\cos(\delta)} - \frac{\cos(\theta-\tau)}{\cos(\tau)}\right] & \text{for } \theta_t^-\leq\theta\leq\theta_t^+ \\ \frac{W}{3}\left[\frac{\alpha\psi^2}{4(\psi+1)^2(1+\beta)}\frac{\cos^2\theta}{\sin\theta} + \frac{\sin\theta}{\alpha} - \frac{1}{\psi+1}\frac{\cos(\theta-\tau)}{\cos(\tau)}\right] & \text{for } \theta_t^+<\theta\leq\frac{\pi}{2} \end{cases} \tag{5.16}$$

The centroid x-coordinate on the plane shown in figure 5.1 corresponds to the distance between the application point of the drag force and the pivot point, since the origin O is placed at the pier-jam contact point. Figure 5.4 presents the normalised x-coordinate of the centroid for given values of α and ψ varying β. It can be noted that with increased values of β the centroid tends to lie in the negative domain, since the projection of W_- becomes larger than the projection of the jam on the W_+ side.

The moment of inertia of a body as sketched in figure 5.1 with respect to the axis of rotation z, can be found by applying the perpendicular axis theorem to a horizontal disk of infinitesimal thickness dz, and then integrating along the z-axis. The density of the debris jam is defined here as ρ_j=$\phi\left(\rho_w + C_M\rho\right)$ where C_M is the coefficient of added mass, ϕ is the fraction of jam volume occupied by the solid (in this case wood), ρ_w is the density of wood.

From (5.2), the two moments of inertia with respect to the x' and y' axes are:

$$\begin{aligned}
I_{x'} &= \rho_j W \int_{-\frac{W}{\alpha}}^{W\frac{\beta}{\alpha}} y'^2 \left(\sqrt{\frac{1+y'\frac{\alpha}{W}}{1+\beta}}\right) dy' - \rho_j \int_0^{W\frac{\beta}{\alpha}} y'^2 \left(y'\frac{\alpha}{\beta}\right) dy' \\
I_{y'} &= \rho_j \int_{-\frac{W}{1+\psi}}^{0} x'^2 \left[-x'^2\frac{(1+\beta)(1+\psi)^2}{\alpha W} + \frac{W}{\alpha} - x'(1+\psi)\frac{\beta}{\alpha}\right] dx' + \\
&+ \rho_j \int_0^{\frac{W\psi}{1+\psi}} x'^2 \left[-x'^2\frac{(1+\beta)}{\alpha W}\frac{(1+\psi)^2}{\psi^2} + \frac{W}{\alpha} + x'\frac{(1+\psi)}{\psi}\frac{\beta}{\alpha}\right] dx'
\end{aligned} \tag{5.17}$$

The resulting integrals are:

$$\begin{aligned}
I_{x'} &= \rho_j \frac{W^4}{420\alpha^3}\left(15\beta^3 + 24\beta^2 - 32\beta + 64\right) \\
I_{y'} &= \rho_j \frac{W^4\left(\psi^2 - \psi + 1\right)(8+3\beta)}{60\left(1+\psi\right)^2}
\end{aligned} \tag{5.18}$$

The moment of inertia of the disk for the perpendicular axis theorem is $I_{z'} = I_{x'} + I_{y'}$ and can now be integrated along the z-axis, yielding:

$$I = \int_{-H}^{0} \left(I_{x'} + I_{y'}\right)\left(1 + \frac{z}{H}\right)^4 dz = \frac{\left(I_{x'} + I_{y'}\right)H}{5}. \tag{5.19}$$

Replacing (5.18) into (5.19) yields the moment of inertia about the z-axis:

$$I = \frac{\rho_j W^4 H}{300\alpha}\left[\frac{\left(\psi^2 - \psi + 1\right)(8+3\beta)}{\left(1+\psi\right)^2} + \frac{15\beta^3 + 24\beta^2 - 32\beta + 64}{7\alpha^2}\right]. \tag{5.20}$$

For simplicity, some terms that are assumed time-independent (which include the dimensions of the solid) are grouped into a single parameter

$$\chi = \frac{1}{12}\frac{\rho C_D W^2 H v^2}{I}, \tag{5.21}$$

Substituting Equations (5.14), (5.16), and (5.21) into (5.1) and defining ω=$\dot{\theta}$, yields the following system of equations:

$$\begin{aligned}
&\dot{\theta} = \omega \\
&\dot{\omega} = \begin{cases}
\chi\left[\left(\frac{\psi}{\psi+1}\frac{\cos(\theta+\delta)}{\cos\delta}\right)^2 - \left(\frac{\alpha}{4(1+\beta)(1+\psi)^2}\frac{\cos^2\theta}{\sin\theta} + \frac{\sin\theta}{\alpha}\right)^2\right] & \text{for } -\frac{\pi}{2}\leq\theta<\theta_t^- \\
\frac{\chi}{(\psi+1)^2}\left[\psi^2\frac{\cos^2(\theta+\delta)}{\cos^2(\delta)} - \frac{\cos^2(\theta-\tau)}{\cos^2(\tau)}\right] & \text{for } \theta_t^-\leq\theta\leq\theta_t^+ \\
\chi\left[\left(\frac{\alpha\psi^2}{4(1+\beta)(1+\psi)^2}\frac{\cos^2\theta}{\sin\theta} + \frac{\sin\theta}{\alpha}\right)^2 - \left(\frac{1}{1+\psi}\frac{\cos(\theta-\tau)}{\cos\tau}\right)^2\right] & \text{for } \theta_t^+<\theta\leq\frac{\pi}{2}
\end{cases}
\end{aligned} \tag{5.22}$$

Equations (5.22) will be used to model the rotational motion of the solid in the range of $-\pi/2\leq\theta\leq\pi/2$. The phase plane object of the following analysis has coordinates θ, ω.

5.2 Analysis of Fixed Points

5.2.1 Non-Tailed Accumulation

This section analyses the fixed points (i.e. steady state or equilibrium solutions of an ODE system) of equation (5.22) for the particular condition given by β=0 (that is, a half-cone body with no tails, i.e. ΔK=0). Under this condition, equation (5.22) simplifies to:

$$\begin{aligned}
&\dot{\theta} = \omega \\
&\dot{\omega} = \begin{cases}
\chi\left[\left(\frac{\psi}{1+\psi}\cos\theta\right)^2 - \left(\frac{\alpha}{4(1+\psi)^2}\frac{\cos^2\theta}{\sin\theta} + \frac{\sin\theta}{\alpha}\right)^2\right], & \text{for } -\pi/2\leq\theta<\theta_t^- \\
\chi\frac{\psi-1}{\psi+1}\cos^2\theta, & \text{for } \theta_t^-\leq\theta\leq\theta_t^+ \\
\chi\left[\left(\frac{\alpha\psi^2}{4(1+\psi)^2}\frac{\cos^2\theta}{\sin\theta} + \frac{\sin\theta}{\alpha}\right)^2 - \left(\frac{1}{1+\psi}\cos\theta\right)^2\right]. & \text{for } \theta_t^+<\theta\leq\frac{\pi}{2}
\end{cases}
\end{aligned} \tag{5.23}$$

The fixed points of the system (5.23) are first determined. Within the sub-domain $\theta_t^-\leq\theta\leq\theta_t^+$, Equation (5.23) only admits one fixed point at ($\frac{\pi}{2}$, 0). This is, however, outside the sub-domain within which the function is defined (i.e. θ_t^+ is always less than π/2). Therefore no fixed points are found within this region of the phase plane. Regarding the sub-domain $\theta_t^+<\theta\leq\pi/2$, four solutions for (5.23) set equal to zero are found at ω=0 and θ=$\arctan\left(\alpha\frac{\pm1\pm\sqrt{1-\psi^2}}{2(1+\psi)}\right)$. However, none of these points are real, since $\psi>1$ by definition. It follows that no fixed points are found in the interval $\theta_t^+<\theta\leq\pi/2$.

In the sub-domain $-\pi/2 \leq \theta < \theta_t^-$, $[\dot{\theta}, \dot{\omega}]$=0 (from Equation (5.23)) admits four solutions given by $\omega = 0$ and θ=$\arctan\left(\alpha \frac{\pm\psi \pm \sqrt{\psi^2-1}}{2(1+\psi)}\right)$. Two of these solutions cannot be accepted as they would result in a positive value of θ; hence, outside of the sub-domain of study, being $\theta_t^- < 0$ (i.e., from (5.12)) for any conditions. For the other two solutions, one of them will always be larger than θ_t^- and cannot be accepted for the domain of study. Within the sub-domain $-\pi/2 \leq \theta < \theta_t^-$, only one fixed point is found at ω=0 and

$$\theta_{nt} = \arctan\left(-\alpha \frac{\psi + \sqrt{\psi^2 - 1}}{2\,(1+\psi)}\right). \tag{5.24}$$

The nature of this fixed point can be determined by analysing the eigenvalues λ_{nt} of the Jacobian J_{nt} of (5.23) at the fixed point θ_{nt} (where the sub-index nt is used to denote the specific condition of a non-tailed body):

$$J_{nt} = \begin{bmatrix} 0 & 1 \\ 2\chi \left[-\sin(2\theta_{nt}) \frac{\psi^2}{(\psi+1)^2} - \frac{2\left(1+\left(\frac{\alpha^2}{4(\psi+1)^2}-1\right)\cos^2\theta_{nt}\right)^2}{\alpha^2 \sin^3\theta_{nt}} \right] & 0 \end{bmatrix} \tag{5.25}$$

$$\lambda_{nt} = \pm\sqrt{2\chi}\sqrt{-\sin(2\theta_{nt})\frac{\psi^2}{(\psi+1)^2} - \frac{2\left(1+\left(\frac{\alpha^2}{4(\psi+1)^2}-1\right)\cos^2\theta_{nt}\right)^2}{\alpha^2\sin^3\theta_{nt}}}. \tag{5.26}$$

Since θ_{nt} is always negative, the term inside the square root of (5.26) must be positive, resulting in real and distinct eigenvalues. Thus, the fixed point θ_{nt} is a saddle. Saddle nodes are surrounded by open trajectories except along the stable manifold. Therefore, considering the problem of a body immersed in a turbulent flow, the problem of a non-tailed accumulation can be practically assumed as inherently unstable. In simple terms, the torque exerted on a non-tailed body with planar asymmetry will never be opposed by a counteracting torque, and the body will simply continue to rotate about the pivot. This makes impossible for such body to remain in a stable equilibrium, unlike experimental observations of debris accumulations.

5.2.2 Tailed Accumulations

In this section it is shown that other fixed points emerge for values of β>0 by analysing the system (5.22). A fixed point for the sub-domain $\theta_t^- \leq \theta \leq \theta_t^+$ of (5.22) occurs at ω=0 and

$$\theta_1 = \arctan\left(\frac{\psi-1}{\psi+1}\frac{\alpha}{2\beta}\right). \tag{5.27}$$

Since $\theta_1 \leq \theta_t^+$ and considering Equation (5.12), it follows that for θ_1 to exist a necessary condition is

$$\psi \leq 1 + \beta. \tag{5.28}$$

A second solution of (5.22) equal to 0 at $\theta_2 = \pi/2$ is omitted as it falls outside the sub-domain considered here. It is now possible to analyse the nature of the fixed point θ_1. The Jacobian of (5.22) for $\theta_t^- \leq \theta \leq \theta_t^+$ and at the fixed point θ=θ_1 is given by

$$J_1 = \begin{bmatrix} 0 & 1 \\ -\frac{2\chi}{(\psi+1)^2}\left[\psi^2\frac{\sin(2(\theta_1+\delta))}{\cos^2\delta} - \frac{\sin(2(\theta_1-\tau))}{\cos^2\tau}\right] & 0 \end{bmatrix} \tag{5.29}$$

the eigenvalues of which are:

$$\lambda_1 = \pm\sqrt{-\frac{2\chi}{(\psi+1)^2}\left[\psi^2\frac{\sin\left(2\left(\theta_1+\delta\right)\right)}{\cos^2\delta} - \frac{\sin\left(2\left(\theta_1-\tau\right)\right)}{\cos^2\left(\tau\right)}\right]}. \tag{5.30}$$

The sign of the terms inside the square brackets define the nature of the fixed points in the phase plane. If positive, λ_1 is purely imaginary, hence the fixed point is a neutrally stable centre; if negative, λ_1 has two real and opposite values and the fixed point is a saddle (i.e. unstable node). For the case of λ_1 the term within square brackets is always positive; hence, the eigenvalue is purely imaginary. As a result, the fixed point θ_1 will always be a neutrally stable centre.

For the interval $\theta_t^+ < \theta \leq \pi/2$, the same analysis reveals four additional solutions of equation (5.22) set equal to zero at ω=0 and

$$\begin{aligned}
\theta_3 &= -\arctan\left[\alpha\frac{1-\sqrt{1-\psi^2}}{2\left(\psi+1\right)\left(1+\beta\right)}\right], \\
\theta_4 &= -\arctan\left[\alpha\frac{1+\sqrt{1-\psi^2}}{2\left(\psi+1\right)\left(1+\beta\right)}\right], \\
\theta_5 &= \arctan\left[\alpha\frac{1-\sqrt{1-\psi^2\frac{1-\beta}{1+\beta}}}{2\left(\psi+1\right)\left(1-\beta\right)}\right], \\
\theta_6 &= \arctan\left[\alpha\frac{1+\sqrt{1-\psi^2\frac{1-\beta}{1+\beta}}}{2\left(\psi+1\right)\left(1-\beta\right)}\right].
\end{aligned} \tag{5.31}$$

Since $\psi > 1$, θ_3 and θ_4 are not real and cannot be fixed points of Equation (5.22). On the other hand, θ_5 and θ_6 are real only if $1 - \psi^2\frac{1-\beta}{1+\beta} \geq 0$. As a result, the fixed points θ_5 and θ_6 can only exist in the phase plane if

$$\beta \geq \frac{\psi^2 - 1}{\psi^2 + 1}, \tag{5.32}$$

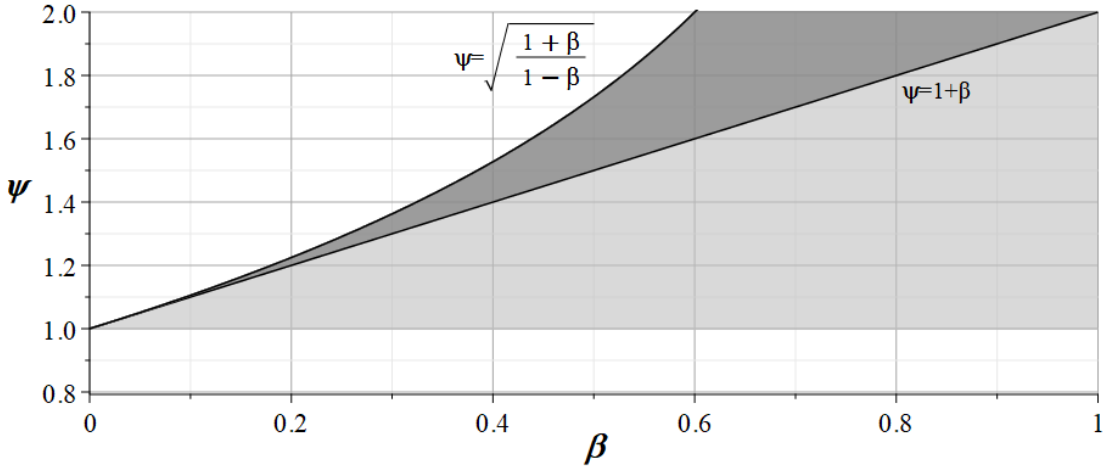

FIGURE 5.5: Region of existence for θ_5 and θ_6: the former is found only in the darker area (which corresponds to the non-existence of θ_1), while the latter is defined for both darker and lighter shaded areas. Values of ψ and β outside of this region would result in no fixed points θ_5 and θ_6.

or, alternatively:

$$1 < \psi^2 \leq \frac{1+\beta}{1-\beta}, \tag{5.33}$$

In other words, θ_5 and θ_6 can only exist for values of $\beta<1$ (i.e. $\Delta K<K$). In addition, the fixed points θ_5 and θ_6 must satisfy the condition $\theta_{5,6}\geq\theta_t^+$. First, $\theta_t^+\leq\theta_6$ can be simplified as:

$$\frac{1}{\psi}\psi^2\frac{1-\beta}{1+\beta} \leq 1+\sqrt{1-\psi^2\frac{1-\beta}{1+\beta}}. \tag{5.34}$$

The second term on the right hand side of (5.34) is real only if $\psi^2\frac{1-\beta}{1+\beta}\leq 1$. Therefore, the left hand side is always less than 1 (since, by definition, $\psi>1$), while the right hand side must be greater than 1; hence, $\theta_6>\theta_t^+$ in any case. The condition $\theta_5\geq\theta_t^+$ leads to $\psi\geq 1+\beta$. As θ_1 is only defined for $\psi\leq\beta$+1, it follows that θ_1 and θ_5 cannot coexist in the phase plane, resulting in maximum two fixed points (i.e. θ_6 and either θ_5 or θ_1) in the positive domain. Figure 5.5 shows the region of existence of θ_5 and θ_6 for values of ψ and β. When conditions in (5.32) or (5.33) are not satisfied, neither θ_5 nor θ_6 exist in the phase plane, thus there will only be open trajectories. Practically, this implies that a small tail or a very large asymmetry factor would lead to a rotation that eventually causes the failure of the debris body. On the right end of the figure, for values of $\beta>1$, neither θ_5 nor θ_6 exists, there will only be θ_1 which (if neutrally stable) would result in a highly stable situation for any condition.

To understand the nature of θ_5 and θ_6, the eigenvalues of the Jacobian matrix of (5.22) are analysed within the sub-domain $\theta_t^+ < \theta \leq \pi/2$:

$$J_2 = \begin{bmatrix} 0 & 1 \\ 2\chi \left[\frac{\sin(2(\theta_{5,6}-\tau))}{\cos^2\tau(\psi+1)^2} + \frac{2\left(1+\left(\frac{\alpha^2\psi^2}{4(1+\beta)(\psi+1)^2}-1\right)\cos^2\theta_{5,6}\right)^2}{\alpha^2\sin^3\theta_{5,6}} \right] & 0 \end{bmatrix} \tag{5.35}$$

for which case θ can be either θ_5 or θ_6. The resulting eigenvalues are

$$\lambda_2 = \pm\sqrt{2\chi}\sqrt{\frac{\sin\left(2\left(\theta_{5,6}-\tau\right)\right)}{\cos^2\tau\left(\psi+1\right)^2} + \frac{2\left(1+\left(\frac{\alpha^2\psi^2}{4(1+\beta)(\psi+1)^2}-1\right)\cos^2\theta_{5,6}\right)^2}{\alpha^2\sin^3\theta_{5,6}}}. \tag{5.36}$$

Equation (5.36) shows that λ_2 can be either real or imaginary, depending on the sign of $\sin\left(2\left(\theta_{5,6}-\tau\right)\right)$. For values of $\theta_{5,6}$ sufficiently large (e.g. $\theta_{5,6} \geq \tau$), λ_2 could be real, resulting in a saddle point, otherwise a neutrally stable centre is observed. This results in the alternation between a centre and a saddle, as will be observed in the phase plane analysis presented in section 5.3, whereby θ_1 (or θ_5 depending on β) provides a centre, while θ_6 is a saddle.

Finally, for the interval $-\pi/2 \leq \theta < \theta_t^-$ solutions to Equation (5.22) set equal to zero occur at ω=0 and

$$\begin{aligned}
\theta_7 &= \arctan\left[\alpha\frac{\psi\left(\beta+1\right)+\sqrt{\psi^2\left(\beta+1\right)^2+\beta^2-1}}{2\left(\psi+1\right)\left(\beta^2-1\right)}\right], \\
\theta_8 &= \arctan\left[\alpha\frac{\psi\left(\beta+1\right)-\sqrt{\psi^2\left(\beta+1\right)^2+\beta^2-1}}{2\left(\psi+1\right)\left(\beta^2-1\right)}\right], \\
\theta_9 &= \arctan\left[\alpha\frac{\psi-\sqrt{\psi^2-1}}{2\left(\psi+1\right)\left(1+\beta\right)}\right], \\
\theta_{10} &= \arctan\left[\alpha\frac{\psi+\sqrt{\psi^2-1}}{2\left(\psi+1\right)\left(1+\beta\right)}\right].
\end{aligned} \tag{5.37}$$

The two results for θ_9 and θ_{10} will be positive; hence, these will not be part of the sub-domain. On the other hand, both θ_7 and θ_8 will be negative for $\beta < 1$. Comparing θ_7 with θ_t^-, the former will always be smaller than the latter, thus a fixed point of the system; conversely, θ_8 will always be greater than θ_t^-, thus not included in the sub-domain. This is the analogous situation to the non-tailed case analysed in the previous section. In order to understand the nature of the only

fixed point θ_7, the Jacobian of (5.22) within the sub-domain -π/2$\leq\theta<\theta_t^+$ is analysed:

$$J_3 = \begin{bmatrix} 0 & 1 \\ 2\chi \left[-\frac{\sin(2(\theta_7+\delta))}{\cos^2\delta} \frac{\psi^2}{(\psi+1)^2} - \frac{2\left(1+\left(\frac{\alpha^2}{4(1+\beta)(\psi+1)^2}-1\right)\cos^2\theta_7\right)^2}{\alpha^2\sin^3\theta_7} \right] & 0 \end{bmatrix} \tag{5.38}$$

The resulting eigenvalues are:

$$\lambda_3 = \pm\sqrt{2\chi}\sqrt{-\frac{\sin\left(2\left(\theta_7+\delta\right)\right)}{\cos^2\delta}\frac{\psi^2}{\left(\psi+1\right)^2} - \frac{2\left(1+\left(\frac{\alpha^2}{4(1+\beta)(\psi+1)^2}-1\right)\cos^2\theta_7\right)^2}{\alpha^2\sin^3\theta_7}}. \tag{5.39}$$

In consideration that θ_7 is always negative, the term inside the square root in (5.39) will always be positive, thus the eigenvalues are distinct and real, which will result in a saddle in the phase plane.

5.3 Phase-Plane Analysis

In this section, the phase-plane of the system of differential equations discussed in the previous section is analysed to provide further insights into the behaviour of the proposed model.

Figure 5.6 shows different phase portraits plotted for the constant value of the asymmetry factor ψ=1.2, 1$\leq\alpha\leq$3 and 0$\leq\beta\leq$1. The blue lines in this figure represent arbitrary trajectories, whereas the black solid line is the boundary between a stable (i.e. orbits around the first fixed point) and unstable (i.e. open trajectories) solutions. These phase portraits were plotted for particular values of other intervening parameters, namely W=0.6 m, H=0.15 m, ρ_j=800 kg/m^3, C_D=1.5, v=0.4 m/s. These values are within the range tested in the experiments in chapter 4, and are adopted here in order to enable an analysis of the proposed model under conditions for which evidence is available. Sub-figures on the top row of figure 5.6 depict the condition analysed in section 5.2.1, where β=0 and only open trajectories are possible, except for the stable manifold of the saddle in the negative domain. For $\beta>0$ two fixed points emerge in the positive domain (namely a centre and a saddle), as also discussed previously. The size of closed orbits about the neutrally stable centre increases with the value of β, which translates into increased stability to the system. Furthermore, for increasing β the distance on the θ axis between these two fixed points increases; the first fixed point (i.e. the neutrally stable centre) is shifted towards the origin, whilst the second fixed point (i.e. the saddle) moves towards higher values of θ. This increases the chances of an oscillatory motion being stable even when the values of the angular displacements are large. At the highest range of β, very large angles and/or angular velocities would be needed in order to reach open trajectories leading to the failure of the debris jam. The value of β=1 is used to illustrate the extreme case of a jam with a very large tail, in which case a strong stability is observed. Indeed, the model implies that for $\beta = 1$, it would be possible

to observe a rotation approaching θ=π/2 that would remain in oscillatory motion about the pier. The figure also shows that when β>0, the stable area of the phase plane increases with α.

Figure 5.7 shows the phase portrait of the system (5.22) for a constant value of β=0.40, and α and ψ varying within the ranges 1≤α≤3 and 1≤ψ≤1.60 (values of W, H, ρ_j, C_D, v in this figure are the same as those used in figure 5.6). The sub-figures at different rows are used to highlight the influence of asymmetry on the stability of the system. The top row shows the phase portrait for a perfectly symmetric body (ψ=1). Under this condition the stable centre is located at the origin, and it is observed that a large perturbation would need to be introduced to induce failure. In addition, the required perturbation from θ=0 increases significantly with α, as has also been previously pointed out in figure 5.6. As ψ increases, the two fixed points approach each other, reducing the region of the domain where closed orbits are possible. For ψ=1.6 the system is intrinsically unstable; no fixed points are observed and any small perturbation would eventually lead to a non-periodic motion. This occurs because ψ is larger than the critical condition as observed in (5.33), which for β=0.4 is ψ=1.53.

The phase planes shown in figures 5.6 and 5.7 also reveal a saddle point in the negative side of the domain. This implies that, in theory, the body could reach an open trajectory towards negative values of θ, although this would require relatively large initial displacements, compared to those required for open trajectories along the positive side of the domain.

5.4 Exact Solution

An exact solution of Eqs (5.22) can be obtained, as described in this section. The solution that is sought here represents a relationship between the angle θ and the angular velocity $\frac{d\theta}{dt}$. The approach used is typically adopted for the exact solution of the motion of a pendulum, and it is detailed in Strogatz (2015). An application is first provided for the simplified non-tailed system in (5.23) and then extended to the complete model in (5.22). Furthermore, the analysis is only provided for the positive domain of θ, in which the failure of a debris accumulation has been observed to consistently occur.

5.4.1 Non-Tailed Accumulation

Consider the equation in (5.23) for $\theta_t^- \leq \theta \leq \theta_t^+$. Both terms on the left and right hand side can be multiplied by $\frac{d\theta}{dt}$ which yields

$$\frac{d\theta}{dt}\frac{d^2\theta}{dt^2} = \chi\frac{\psi+1}{\psi-1}\frac{d\theta}{dt}\cos^2\theta. \tag{5.40}$$

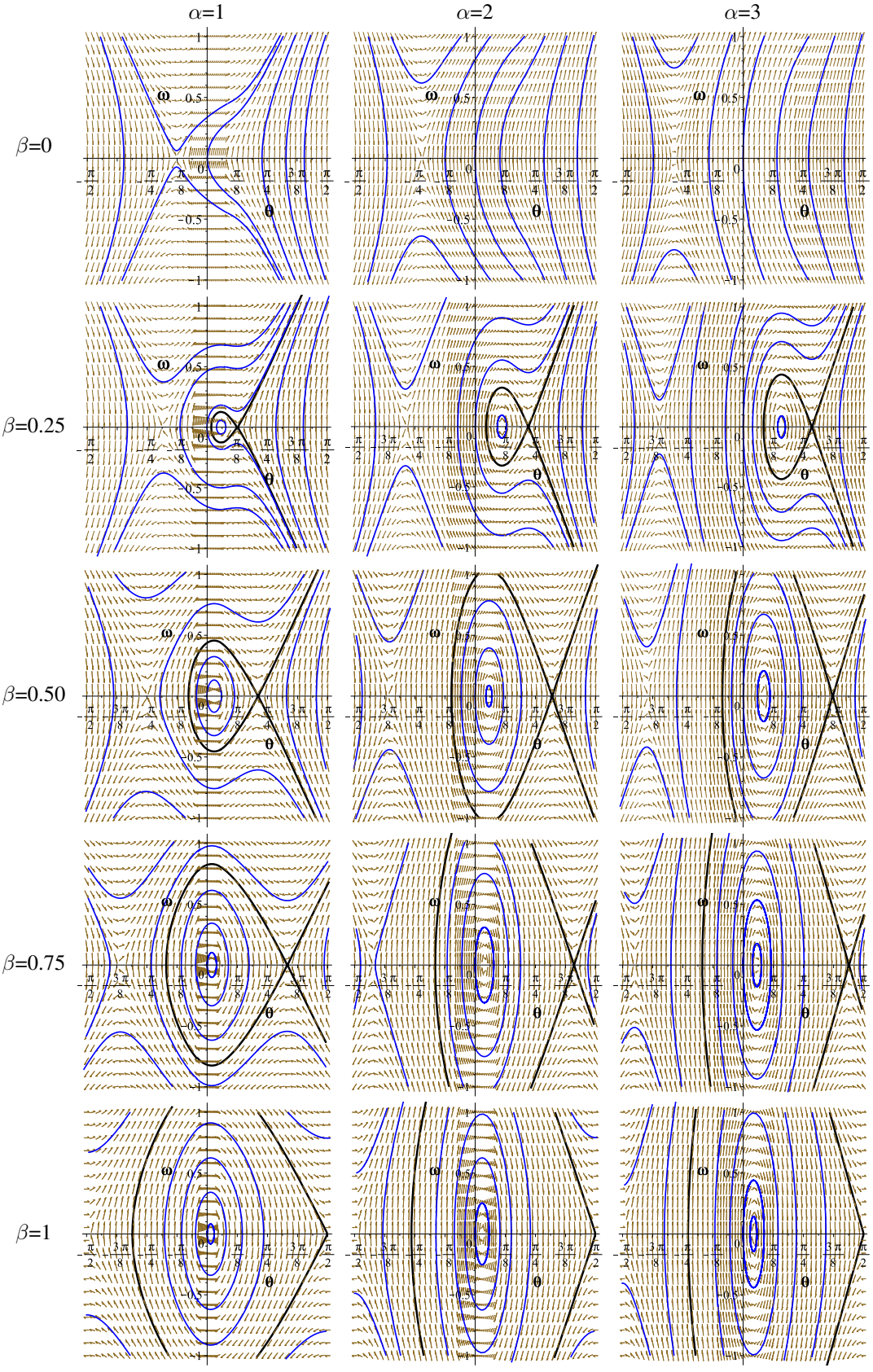

FIGURE 5.6: Phase portraits for constant ψ=1.20 and varying α and β. Horizontally, α takes values of 1.0, 2.0, and 3.0 from left to right. Vertically, β takes values of 0, 0.25, 0.50, 0.75, and 1 from top to bottom.

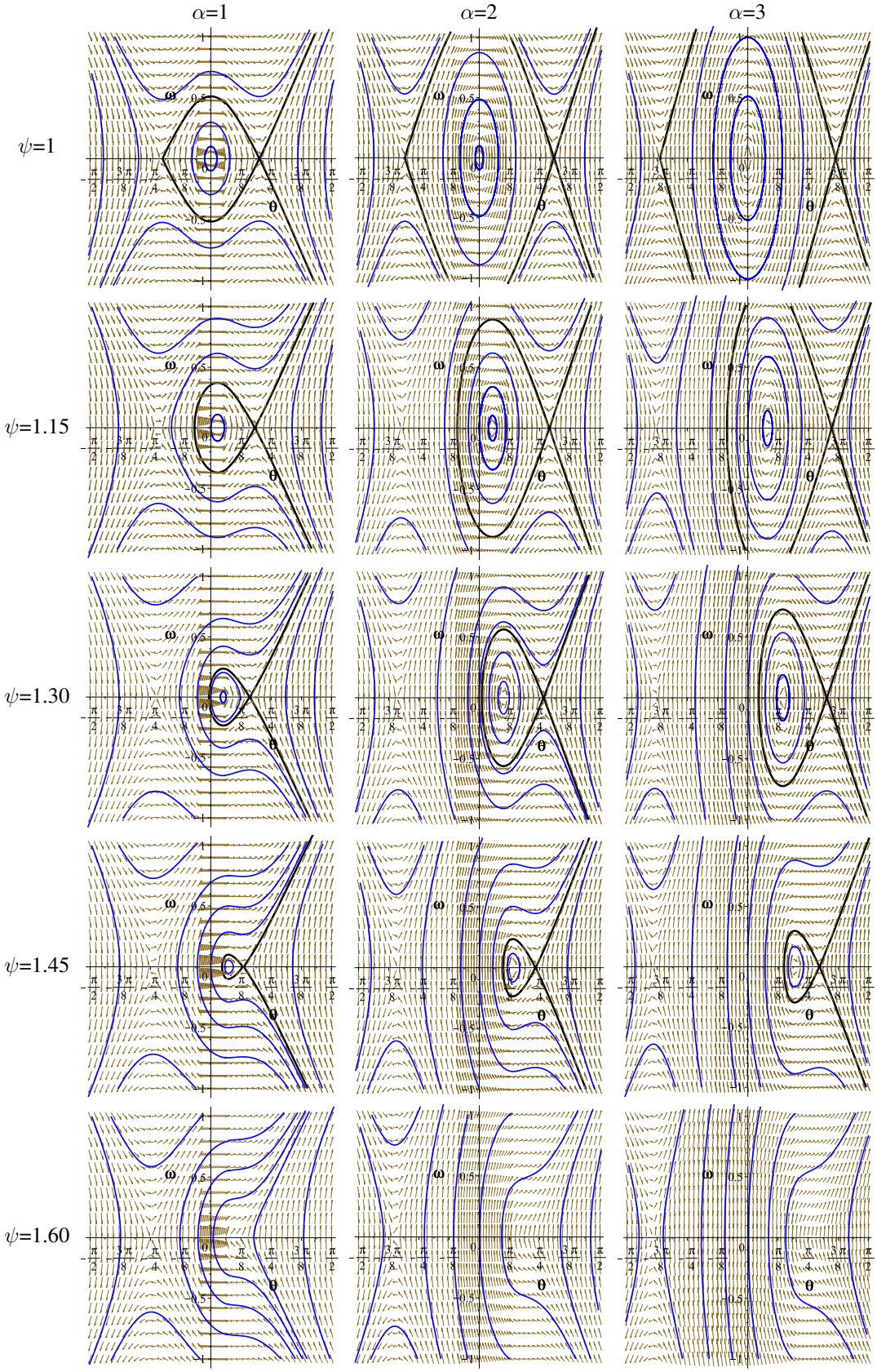

FIGURE 5.7: Phase portraits for constant β=0.40 and varying ψ and α. Horizontally, α takes values of 1, 2, and 3 from left to right. Vertically, ψ takes values of 1, 1.15, 1.30, 1.45, and 1.60 from top to bottom.

The second derivative of θ in (5.40) is also the first derivative of $\frac{d\theta}{dt}$; therefore, the term on the left-hand side (5.40) can be rearranged as

$$\frac{d\theta}{dt}\frac{d^2\theta}{dt^2} = \frac{1}{2}\frac{d}{dt}\left[\left(\frac{d\theta}{dt}\right)^2\right]. \tag{5.41}$$

Likewise, the right-hand side of (5.40) can be reformulated as:

$$\chi\frac{\psi+1}{\psi-1}\frac{d\theta}{dt}\cos^2\theta = \chi\frac{\psi+1}{\psi-1}\frac{d}{dt}\left(\frac{1}{2}\sin\theta\cos\theta + \frac{1}{2}\theta\right). \tag{5.42}$$

As a result, equation (5.40) can be rearranged using (5.41) and (5.42), which yields:

$$\frac{d}{dt}\left[\frac{1}{2}\left(\frac{d\theta}{dt}\right)^2 - \chi\frac{\psi+1}{\psi-1}\left(\frac{1}{2}\sin\theta\cos\theta + \frac{1}{2}\theta\right)\right] = 0. \tag{5.43}$$

Equation (5.43) is true only if the term within square brackets is a constant, namely C_1; hence:

$$\frac{1}{2}\left(\frac{d\theta}{dt}\right)^2 - \chi\frac{\psi+1}{\psi-1}\left(\frac{1}{2}\sin\theta\cos\theta + \frac{1}{2}\theta\right) = C_1. \tag{5.44}$$

The constant C_1 can be determined by providing initial conditions. Assuming that at the time t=0 the jam is not tilted and at rest - i.e. $\theta\,(t=0)$=0 and $\frac{d\theta}{dt}\,(t=0)$=0 - the constant C_1 is null. As a result, (5.44) can be solved with respect to the angular velocity, which yields:

$$\frac{d\theta}{dt} = \sqrt{2\chi\frac{\psi+1}{\psi-1}\left(\frac{1}{2}\sin\theta\cos\theta + \frac{1}{2}\theta\right)}. \tag{5.45}$$

This represents the exact solution of the motion in the phase plane of a non-tailed jam in the domain $0{\leq}\theta{\leq}\theta_t^+$. Using the same approach adopted for the first part of the domain, the equation in (5.23) for $\theta_t^+{<}\theta{\leq}\pi/2$ may be solved as:

$$\frac{d}{dt}\left[\frac{1}{2}\left(\frac{d\theta}{dt}\right)^2 - \frac{1}{2}\frac{\chi}{(\psi+1)^4}\left(\frac{\gamma_1\zeta_1}{\alpha^2} + \gamma_2\zeta_2 + \frac{1}{16}\alpha^2\psi^4\gamma_3\right)\right] = 0, \tag{5.46}$$

where

$$\begin{aligned}
\gamma_1 &= -\frac{1}{2}\cos\theta\sin\theta + \frac{1}{2}\theta,\\
\gamma_2 &= \frac{1}{2}\cos\theta\sin\theta + \frac{1}{2}\theta,\\
\gamma_3 &= -\frac{\cos^3\theta}{\sin\theta} - 3\gamma_2,\\
\zeta_1 &= (\psi+1)^4,\\
\zeta_2 &= \frac{1}{2}\psi^4 + \psi^3 - \frac{1}{2}\psi^2 - 2\psi - 1.
\end{aligned}$$

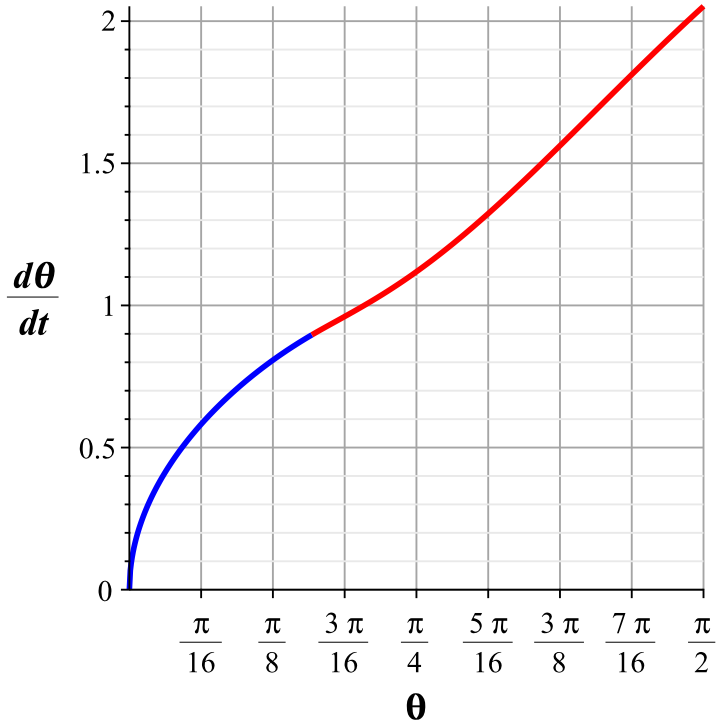

FIGURE 5.8: Exact solution for the motion on the phase plane of a non-tailed jam according to equations (5.48). Constant values used for this figure were: W=0.6 m, H=0.15 m, ψ=1.2, v=0.4 m/s, ρ=1000 kg/m^3, ρ_j=800 kg/m^3, C_D=1.5, α=2, and β=0. The blue curve is for $0 \leq \theta \leq \theta_t^+$, whereas the red curve is for $\theta_t^+ < \theta \leq \pi/2$.

Even for this situation, the content within square brackets must be a constant value C_2. Nevertheless, unlike C_1 this constant C_2 cannot be null, since at t=t_t^+, θ=θ_t^+ and the angular velocity is $\frac{d\theta}{dt}$=$\sqrt{\chi \frac{\psi-1}{\psi+1} \left(\sin\theta_t^+ \cos\theta_t^+ + \theta_t^+\right)}$. Thus:

$$C_2 = \frac{\chi}{2}\left[\frac{\psi-1}{\psi+1}\left(\sin\theta_t^+ \cos\theta_t^+ + \theta_t^+\right) - \frac{1}{(\psi+1)^4}\left(\frac{\gamma_{1t}\zeta_1}{\alpha^2} + \gamma_{2t}\zeta_2 + \frac{1}{16}\alpha^2\psi^4\gamma_{3t}\right)\right], \quad (5.47)$$

where γ_{1t}, γ_{2t}, and γ_{3t} are respectively γ_1, γ_2, and γ_3 at θ=θ_t^+. As a result, the motion of an idealised woody debris jam in the phase plane is described by:

$$\begin{aligned}
\frac{d\theta}{dt} &= \sqrt{\chi\frac{\psi-1}{\psi+1}\left(\sin\theta\cos\theta+\theta\right)}, && \text{for } 0\leq\theta\leq\theta_t^+ \\
\frac{d\theta}{dt} &= \sqrt{\frac{2\chi}{(\psi+1)^4}\left(\frac{\gamma_1\beta_1}{\alpha^2}+\gamma_2\beta_2+\frac{1}{16}\alpha^2\psi^4\gamma_3\right)+2C_2}. && \text{for } \theta_t^+<\theta\leq\pi/2
\end{aligned} \quad (5.48)$$

Figure 5.8 shows the angular velocity of an idealised jam in the phase plane for both $0 \leq \theta \leq \theta_t^+$ (blue curve) and $\theta_t^+ < \theta \leq \pi/2$ (red curve) domains.

5.4.2 Tailed Accumulation

For the tailed accumulation scenario, the approach for the exact solution of the motion of a jam is the same as for the non-tailed case. All terms in (5.22) are multiplied by $\frac{d\theta}{dt}$, which for $0{\leq}\theta{\leq}\theta_t^+$ yields:

$$\frac{d}{dt}\left[\frac{1}{2}\left(\frac{d\theta}{dt}\right)^2-\frac{\chi t}{2\left(\psi+1\right)^2}\left(\psi^2\frac{\cos\left(\theta+\delta\right)\sin\left(\theta+\delta\right)+\theta+\delta}{\cos^2\delta}-\frac{\cos\left(\theta-\tau\right)\sin\left(\theta-\tau\right)+\theta-\tau}{\cos^2\tau}\right)\right]=0. \tag{5.49}$$

Once again, the content within square brackets in (5.49) must be a constant C_3. For initial conditions $\theta(0)$=0 and $\frac{d\theta}{dt}(0)$=0, this constant is

$$C_3=-\frac{1}{12}\frac{\chi}{\left(\psi+1\right)^2}\left(\psi^2\frac{\cos\delta\sin\delta+\delta}{\cos^2\delta}+\frac{\cos\tau\sin\tau+\tau}{\cos^2\tau}\right). \tag{5.50}$$

Therefore, the angular velocity is found as:

$$\frac{d\theta}{dt}=\sqrt{\frac{\chi}{6\left(\psi+1\right)^2}\left(\psi^2\frac{\cos\left(\theta+\delta\right)\sin\left(\theta+\delta\right)+\theta+\delta}{\cos^2\delta}-\frac{\cos\left(\theta-\tau\right)\sin\left(\theta-\tau\right)+\theta-\tau}{\cos^2\tau}\right)+2C_3}. \tag{5.51}$$

Similarly, for $\theta_t^+{<}\theta{\leq}\pi/2$ the above approach yields:

$$\frac{d}{dt}\left[\frac{1}{2}\left(\frac{d\theta}{dt}\right)^2-\frac{\chi}{12\left(1+\psi\right)^2}\left(2\gamma_1\alpha^2\left(\psi+1\right)^2-\gamma_\tau+\frac{\psi^2\gamma_2}{1+\beta}+\frac{\alpha^2\psi^4}{\left(1+\beta\right)^2}\gamma_4\right)\right]=0, \tag{5.52}$$

where γ_1 and γ_3 are as defined for the non-tailed case, whilst $\gamma_\tau{=}\frac{\cos(\theta-\tau)\sin(\theta-\tau)+\theta-\tau}{\cos^2(\tau)}$ and $\gamma_4{=}\frac{\cos^3(\theta)-3\theta\sin(\theta)-3\cos(\theta)}{16\sin(\theta)}$.

The terms within square brackets must be equal to a constant value C_4. This is calculated for both θ and $\frac{d\theta}{dt}$ at $\theta{=}\theta_t^+$ (expression of C_4 is omitted for length of calculation).

Figure 5.9 shows two plots of the exact solution for a tailed debris accumulation in the phase plane in which respectively a failure and a stable orbit occur, only by changing the value of β (i.e. 0.3 and 0.4 respectively). For the former, it can be observed that the trajectory is open (hence, a jam failure) and that after a slow down in angular velocity, this is accelerated again. For the latter, the trajectory is closed, indicating a stable situation, in which there is no failure of the woody debris jam.

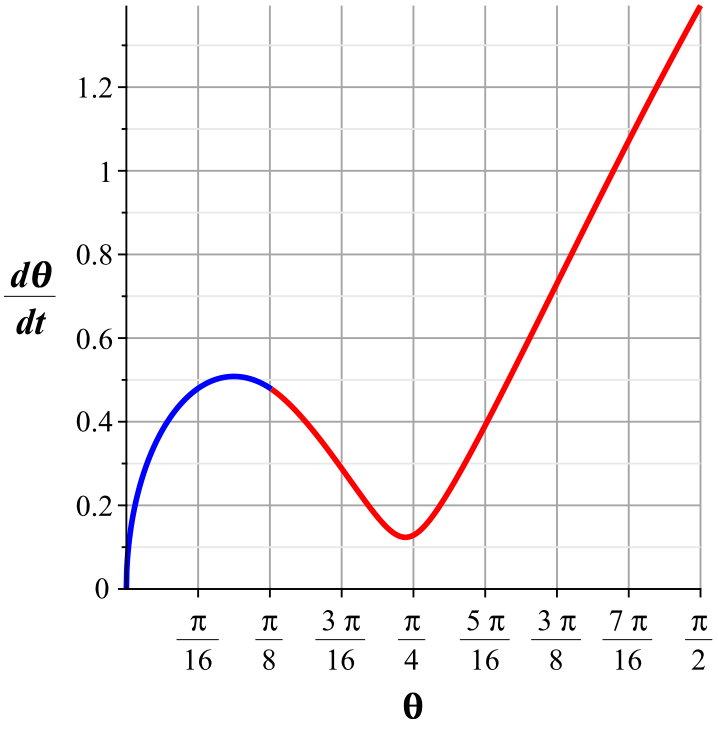

(A)

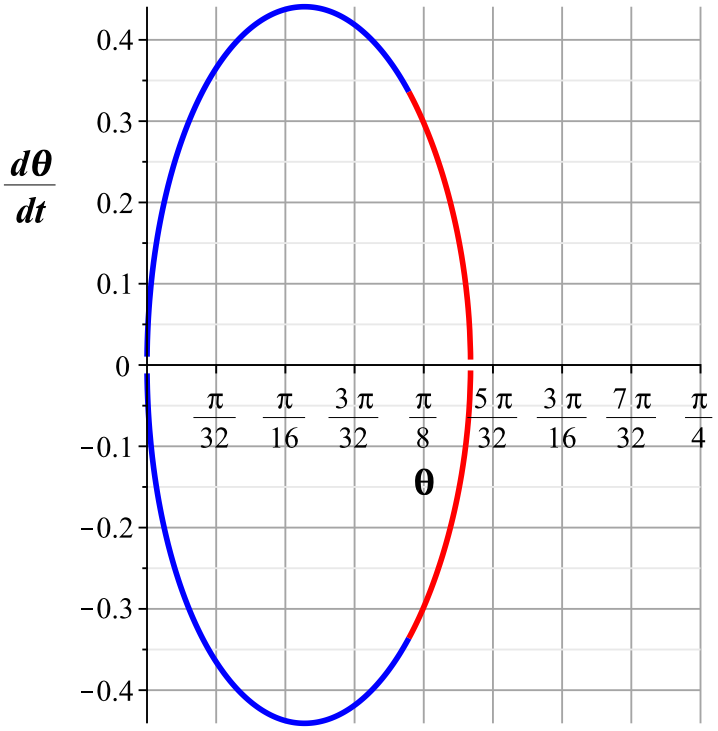

(B)

FIGURE 5.9: Exact solution for the motion on the phase plane of a tailed jam according to equations (5.48). Constant values used for this figure were: W=0.6 m, H=0.15 m, ψ=1.2, v=0.4 m/s, ρ=1000 kg/m^3, ρ_j=800 kg/m^3, C_D=1.5, α=2, and β=0.3 (5.9a) and 0.4 (5.9b). The blue curve is for $0 \leq \theta \leq \theta_t^+$, whereas the red curve is for $\theta_t^+ < \theta \leq \pi/2$.

5.5 Comparison Against Experimental Observations

In this section the models ability to capture different patterns of the formation, growth, and failure of debris accumulations that were observed during previous laboratory tests is analysed. The following subsections relate some of the key observations extracted from the experiments to the predictions provided by the theoretical model described in the previous sections.

5.5.1 Impossibility of Formation of Non-Tailed Accumulations

It is first tested the ability of the proposed model to capture the impossibility of an accumulation to form a non-tailed accumulation. During the experiments in chapter 4, such a shape was never observed, neither during a stable nor a critical (i.e. immediately prior to failure) condition. The results of the analysis presented in section 5.2.1 confirms that the model agrees with these laboratory observations. Namely, no fixed points are possible in the positive domain of the phase plane. The only fixed point occurs for negative values of θ and is a saddle node. While in theory stability occurs along the stable manifold of the saddle, in the real-world any small disturbance from this state - e.g. induced by turbulence - would result in open trajectories. Therefore, in practical terms, such a system is always unstable, and any small perturbation (i.e. planar asymmetry $\psi \neq 1$) would result in large rotations ultimately leading to the removal of the jam from the pier. In this case, the force exerted by drag would neither establish a rotation that is periodical nor tend to a static equilibrium. Thus, non-tailed accumulations are impossible to form since they would be intrinsically unstable and would inevitably lead to the rotation and removal of the debris jam.

5.5.2 Shape Characteristics of Stable Accumulations

Experimental data-sets provide the opportunity to compare the shape characteristics (i.e. α, β, and ψ) of debris accumulations formed in the laboratory against the model's predictions. Figure 5.10 shows the values of ψ and β observed during 105 different experiments, along with the curves defining the limits of existence of fixed points (as previously defined in figure 5.5). In this figure, the blue circles represent values of β and ψ at time T immediately before the failure of the accumulation (that is the elapsed time between the first piece of debris is entrapped and the beginning of the dislodgement of the whole debris jam), whereas the red squares represent the same values measured at $T/3$, when the body can be assumed stable (i.e. when very small or negligible periodical rotations were observed). The figure shows a clear distinction between the two groups. Stable jams are observed on the right-side of the graph, where the model predicts that both θ_1 and θ_6 exist and θ_1 (i.e. the neutrally stable centre) is closer to the origin of the phase plane, which translates into high stability. On the other hand, *unstable* jams are found on the left of the graph, very close to the boundaries that define the existence of θ_1 and θ_5 and

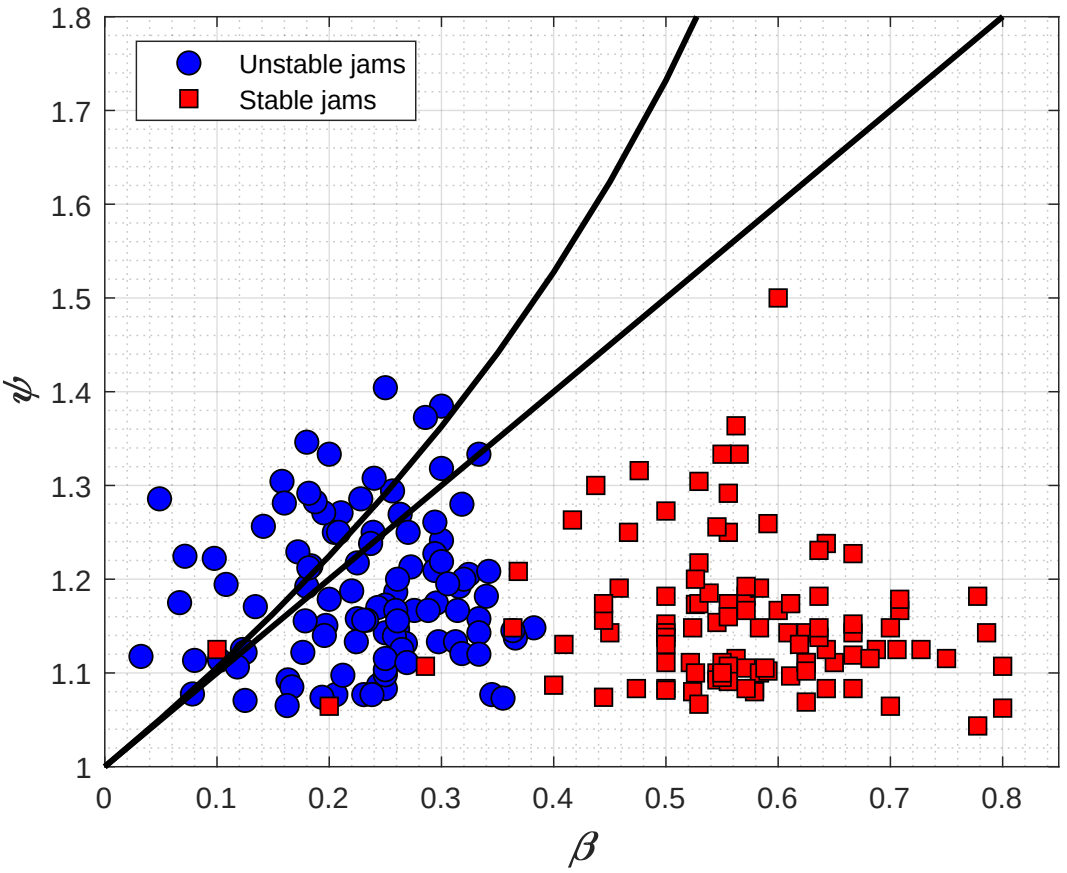

FIGURE 5.10: Region of existence of fixed points according to figure 5.5 overlapped to experimental data.

in many instances above the upper boundary, in which case no fixed points are found and only open trajectories are possible.

5.5.3 Repeatability of Observed Dimensions at Failure

The experiments in chapter 4 showed that all debris piles, formed by the successive accumulation of individual logs, fail upon reaching maximum values of W, K, and H. In addition, repeated experiments conducted under the same flow conditions showed that the dimensions at failure display a relatively small variation. At first, this last observation is somewhat puzzling, since the process of collection of debris elements is inherently stochastic. It is here argued that such a behaviour can be explained based on the proposed model, as follows.

Section 5.3 has shown that the model predicts increasing stability with increasing values of α and β. This is in agreement with the process of accumulation of debris pieces observed in the laboratory. Shortly after the first mesh of debris is formed, only a few debris elements are collected on the upstream side of the pier. The orientation of these elements is such that the initial

values of ΔK and W are large compared to the longitudinal dimension K, resulting in the maximum values for α and β. Under these conditions, the model predicts a debris jam that is very stable, and experimental observations show that indeed no failure is observed during these initial stages. As other debris elements accumulate upstream, the growth rate of K is faster than the corresponding growth of W and ΔK, thus both α and β gradually decrease. Eventually, when the values of α and β are very low the jam is removed from the pier. The model predicts that low values of α and β result in a significant reduction of the stable region of the phase plane, thus increasing the probability of failure. This indicates that the condition in which failure occurs, while influenced by processes that are inherently stochastic, also has a strong deterministic component, which agrees with the repeatability of dimensions observed in various experiments.

5.5.4 Direction of Failure

The phase portraits presented in §5.3 show that open trajectories leading to a rotation towards the negative direction can be observed in the phase-plane. For the body to follow this open trajectory, it must rotate by a certain negative value of θ that depends on α, β, and ψ (i.e. $\theta<\theta_t^-$). However, if the body is to reach these trajectories, it must first pass through a region of the domain filled with open positive trajectories, which would lead to a positive failure. In other words, failure by a rotation towards the side of the lowest semi-width is, in practice, virtually impossible. This agrees with the observations in chapter 4, which show that all failures observed in 732 experiments occurred through a rotation towards the positive (i.e. widest side) direction.

5.6 Conclusions

The analysis developed in this chapter provides the description of rotational and oscillatory motion of a woody debris jam at a bridge pier, idealised by an asymmetric solid having half-conical shape with extended tails immersed in a fluid and left free to rotate about a pivot. The model was developed on simplified hydrodynamic actions and a second-order polynomial geometry, which included an asymmetric shape typically observed in debris jams.

The main geometrical variables of the model - width W, length K, and tail extension ΔK - are rearranged in terms of three dimensionless variables, i.e. α=W/K, β=$\Delta K/K$, and the already defined asymmetry factor ψ. Applying the principle of angular momentum conservation, a second order ODE system is developed, in which for simplification only the moment originated by the drag force is considered.

The equations resulting from the interaction between the idealised geometry and the drag force exerted by the flow were analysed on the phase plane. For a tailed, asymmetric solid, two fixed points can be observed in the system, that typically show the alternation between a neutrally stable centre node (the first fixed point) and a saddle (the second fixed point). The dimensionless

variables previously defined play key roles for the stability of the system, that is the periodic rotation around the first fixed point. First, the tail factor β is crucial in order to provide stability: in a non-tailed situation (i.e. β=0), a jam is unstable at any conditions, leading to open trajectories (i.e. a failure) even with very small asymmetry in place. On the other hand, a non-null β yields the appearance of a fixed point. Increasing values of β produce a higher degree of stability, shifting the neutrally stable node towards the origin (thus strengthening the orbits around the fixed point) and the saddle towards higher values of θ reducing its potential attraction. The asymmetry factor ψ is also necessary to assess the overall stability: at the limit case of ψ=1 (i.e. a symmetric solid), the neutrally stable node lies on the origin, there are no oscillations, and only a very large perturbation could lead to a failure. On the other hand, if ψ is greater than a threshold value (depending on β), the system is unstable for any conditions.

A further analysis on the ratio α/β provides important insights into the solid motion and the condition for which open trajectories can be observed. An analysis of varying α and β but keeping constant α/β, displays that the motion of the solid is very stable for high α, while its decrease (and, consequently, the decrease of β) yields instability, which could eventually lead to non-periodical oscillations of the solid. This final analysis is helpful in providing a deterministic explanation to the experimental observation of a jam failure, which occurred only to fully developed jams, i.e. after that α and β decreased by several factors.

In conclusion, factors influencing the stability of porous asymmetrical bodies immersed in fluids (i.e. woody debris jams) are various. Tails (intended as protrusions downstream of the pivot point line) provide stability and this increases with increasing tail extensions. Planar asymmetry plays a vital role in the stability of the solid since no motion occurs without its occurrence and instability increases with increasing asymmetry. On the other hand, the combined effect of α and β is key to determine the conditions for which a solid could be moving either in a neutrally stable orbit or in open trajectories. The relationship between these two variables highlighted that a jam becomes unstable not only for large asymmetries, but also when a relatively small tail and large upstream extension occur together.

Chapter 6

Conclusions

Understanding the phenomenon of the formation and growth of woody debris jams at bridge piers is of primary importance for assessing the risk of bridge collapse and flooding, as well as for the design of new bridges. This doctoral thesis provides a detailed experimental analysis of the whole life of debris accumulations at bridge piers including their formation, growth, and failure. In addition, a theoretical model of the jam final failure has been developed based on the experimental observations, which captures the most important aspects of the behaviours of debris jams observed in the laboratory. In this chapter, a comparison with the state-of-the-art is shown and a summary of the main conclusions drawn from the analysis of the experiments and theoretical model are presented.

6.1 Comparison Between this Thesis and the State-of-the-Art

In the context of the current state-of-the-art, the results from this thesis showed that it is possible to provide an estimation of the maximum size that debris accumulations may reach at a single bridge pier. Currently, other research provided useful information for estimating scour at single piers or increase of upstream afflux, that can be used for scour and flood risk assessments. However, these applications would need input data that is relative to the assessment flow and the size and features of the obstruction. The ability to estimate the size of debris accumulations and the drag coefficient at single piers would provide key parameters (e.g. the frontal area of the accumulation) for this type of analysis.

Furthermore, previous research focused mostly on the probability of entrapment of single debris elements at piers, with little consideration of the processes that follow this initial stage. The results presented in this thesis provide a comprehensive description of the accumulation of large woody debris at a bridge pier and the factors influencing the jam formation and growth. In addition, key-phenomena that were observed (e.g. the failure at the end of the jam life) are

also presented and discussed. Thus, the results of this doctoral thesis further develop and substantially increase our understanding of the interactions between woody debris and piers, and provide practical methods that can be applied in engineering practice.

6.2 Observations on the Time-Evolution of Debris Accumulations at Bridge Piers

Experimental observations unveiled three distinct phases that are conceptually classified as *unstable*, *stable*, and *critical* conditions. The unstable phase occurs at the initial stage of the accumulation process. The debris pile grows at a rapid pace and a framework of debris pieces is formed. During this phase, individual elements can be easily mobilised and disengaged from the jam, resulting in frequent size variations. This stage is followed by a slower but more stable growth phase. Only moderate changes can be observed and the jam assumes the typical half-cone shape that characterises all debris jams experimentally observed. Finally, at the critical phase an oscillatory rotational movement about the pier occurs, which eventually results in the dislodgement of the jam from the pier. In the large majority of the experiments, the maximum size of the debris jams was observed at the onset of this stage.

6.3 Factors Affecting Debris Jams

The experimental analysis conducted in this work included several factors that were tested in the lab, that are the length and diameter of individual debris elements, the size of the bridge pier, the flow velocity, the water depth, the density of debris elements, the shape of debris elements, the shape of the bridge pier. Three maximum dimensions have been defined and used to characterise the geometry of debris accumulations immediately prior to failure in this thesis (i.e. width W^c, height H^c, and length K^c, and the respective variables made dimensionless with the length of debris element ω^c, η^c, and κ^c). The influence of a number of parameters on the geometry of debris jams has been analysed through a set of 732 experiments.

Results have shown a strong correlation between the jam size and the debris Froude number $Fr_L = v/\sqrt{gL}$. Typically, at low values of Fr_L, the dimensionless height η^c is at its minimum, whereas ω^c and κ^c reach their maximum values. With increasing Fr_L, the values of ω^c and κ^c decrease, while η^c displays the opposite trend. An important difference was observed between debris jams formed with uniform and non-uniform distributions of the length of individual debris elements. Debris piles of the former are significantly wider than those formed by the latter (the length of the elements of which follows a log-normal distribution). As a result, jams in the real-world (that are arguably more likely to be formed by elements of mixed size) might be

overestimated if modelled by idealised jams formed of single-size debris pieces. A functional relationship based on a regression of the experimental data is proposed in this thesis, in which the maximum size of a debris jam can be predicted based on the length of the debris elements L and the velocity v at the pier section. This function can be used for bridge design and afflux estimation purposes, and may also inform further research on the topic of LWD accumulations.

Under the experimental conditions studied in this thesis, the diameter of the circular piers was observed to have negligible influence on the values of ω^c, η^c, and κ^c. In a similar way, the dimensionless debris diameter d/L, the dimensionless water depth h/L, and the shape of the pier displayed no notable effects on the maximum size reached by an accumulation within the studied range. The same conclusions can be drawn for the relative debris density ρ_L/ρ but only with respect to the width ω^c and length κ^c of an accumulation. This was not the case for the dimensionless height η^c, for which the experiments performed with the highest value of ρ_L/ρ resulted in an accumulation that was up to 30% deeper than debris jams with lower densities.

The comparison of the dimensions of debris jams formed by individual elements of different shapes - namely, dowels, natural unbranched sticks, and branched sticks - has revealed substantial differences. Debris jams formed by dowels (i.e. perfectly cylindrical debris) displayed dimensions similar to those obtained in experiments with natural sticks for the lowest range of Fr_L. Nevertheless, for increasing values of Fr_L the size reached by dowel jams decreased significantly, up to 40% for ω^c with respect to natural sticks. In addition to the above, it was not possible to form these jams for Fr_L>0.40, since elements were removed from the pier by the flow under any condition. On the other hand, experiments with branched debris elements displayed a different formation process with respect to non-branched sticks. The accumulations formed by branched elements were highly unstable, in which early failures were frequent and elements were constantly accumulated and removed. In all instances, a size substantially smaller than natural sticks was observed for jams formed by branched debris, especially at the lowest range of Fr_L tested.

6.4 Theoretical Analysis

In this thesis it is proposed a modelling framework to analyse the interactions between flow and a debris jam that is free to rotate about a bridge pier. The model was built upon the assumption that the motion of the jam is primarily driven by dynamic changes of the point where drag force is applied, which in addition is assumed to depend on the geometry of the body and its orientation only. The geometry employed in the model was defined as an asymmetric half-cone with extensions that are referred to as *tails*.

The main geometrical variables of the model, namely the jam width W, length K, and tail extension ΔK, defined two dimensionless shape parameters α=W/K and β=$\Delta K/K$, which along with the asymmetry factor ψ were found to govern much of the observed behaviour. A non-linear system of ODEs resulted from the application of conservation of angular momentum of the jam subject to the moment of the drag force. The system was analysed on the phase plane. For a tailed, asymmetric solid, three fixed points can be observed in the phase plane, which typically show the alternation between a neutrally stable centre node and a saddle, that is the alternation between a region of periodic oscillations (i.e. stable rotations) and open trajectories (i.e. unstable rotation of the jam). The dimensionless variables previously defined play key roles in the stability of the system (that is the periodic rotation around the first fixed point). First, the tail factor β is crucial in order to provide stability. The model predicts that a non-tailed body (i.e. β=0) is inherently unstable, leading to open trajectories (i.e. a failure) even if it is almost perfectly symmetric. On the other hand, increasing values of β produce more stable conditions by shifting the neutrally stable node towards the origin and the saddle towards higher values of θ (thus increases the area of the phase plane corresponding to closed orbits). The asymmetry factor ψ is also key to the stability of the system. For symmetric bodies (i.e. ψ=1), the neutrally stable node lies on the origin and only a very large perturbation could lead to a failure. On the other hand, if ψ is greater than a threshold value (which also depends on β), the system is unconditionally unstable.

A comparison between experimental observations and model predictions confirmed the ability of the proposed model to capture the main characteristics of the motion of debris jams observed in the laboratory. This includes *i*) the model's prediction of the impossibility of the formation of a non-tailed body (which, as a confirm, was never observed to form during the experiments); *ii*) its ability to capture key differences in the shape of stable and unstable jams related to the values of α, β and ψ; *iii*) an explanation for the repeatability of debris jam dimensions at failure; and *iv*) the model's prediction of the direction towards which the rotational motion leading to failure should occur, which agrees with all experimental data available.

Chapter 7

Limitations and Further Research

This chapter provides an overview of the limitations that have been encountered during the experimental and theoretical analysis and therefore an indication of those elements that should be considered with caution. Moreover, further research is advised in the following section, indicating the main topics that should be further studied based on the findings of this thesis.

7.1 Limitations

Despite all efforts that were made to obtain the most accurate and detailed analysis resulting from this research, some limitations were unavoidable and are therefore reported here. These should be taken into account when results in this thesis are being used.

7.1.1 Range and Stochasticity of the Variables Studied and Transferability

The experimental tests covered a wide number of variables, as well as their widest possible range in consideration of the available time and resources. Nonetheless, the analysis resulting from the experiments should include some caveats.

The analysis reported in chapter 4 is only applicable to the observed range for each variable studied. It is unclear whether the experimental observations reported in this work would be valid outside of this range. Moreover, despite the relative low dispersion of the results of the jam size the phenomena of debris supply, transport, and accumulation are inherently stochastic. A set of repeated experiments was carried out to shed a light on the variability that the jam size may reach and showed that data scattering was limited, but this was studied for only one particular condition and may not be representative of the entire data set.

The experimental results at laboratory scale can be transferred to full-scale analyses by the dimensional analysis conducted in this study. However, only Froude similarity could be provided, whereas Reynolds invariance was assumed, despite the flow conditions at laboratory scale were not fully turbulent. It is unclear under this assumption whether Reynolds scale effects could be significant. The experiments were also carried out under idealised conditions, including a fixed bed and a constant flow. At full scale, scour may occur at the pier base and flows can vary significantly in short periods. These dynamic changes may have important effects on the debris jam formation and failure, and should be considered for further developments of this research.

7.1.2 Uncertainties in Measurements

Limitations due to instruments sampling accuracy or to the methodologies adopted need to be considered. In general, instruments had high accuracy that can be relied with confidence. Cross-checks between instruments were made to calibrate and test the suitability of these instrument (for example, the ultrasonic probes with a point gauge). However, in some cases measurements were made combining the data from two instruments (e.g. velocity at the pier section was measured by using the discharge, measured by the IQ, and the water depth, measured by the ultrasonic probe), the combined accuracy of which may be lower than a single instrument would provide.

On the other hand, some inaccuracies could be possible for the measurements of the jams size. In this case, the size of the reference grid was 10 mm (top camera) and 12.7 mm (side and submerged cameras). The visual measurement of the jam size was conducted up to half the size of a cell. Therefore, errors up to a quarter of a cell, respectively 2.5 mm and 3.2 mm, were possible. Another source of uncertainty was the definition of the exact boundaries of a jam. For example, some elements out of the water were visible from the top camera but not effectively contributing to the hydraulics of the jam-pier interaction. The use of multiple cameras provided practical and substantial help in matching sizes and minimising uncertainty, although this could not be excluded in its entirety.

Caution should also be adopted when considering the values of the drag coefficient obtained from this work. For this particular case, sources of uncertainty are more marked than for other variables. First, the drag coefficient was computed assuming triangular cross-sections. While this is an accurate approximation for many of the observed accumulations, it may not properly represent some of the jams that were formed. Another factor that might have limited the accuracy of the computed drag coefficient was the flow velocity used to discount the drag exerted by the flow on the pier section under the debris accumulation. In fact, the actual velocity at the pier with a debris pile is likely to be different from the undisturbed situation. All of these reasons may explain the scattering observed for the drag coefficient, which is not negligible. A more

accurate computation of the drag coefficient would require experiments specifically designed for this purpose, which were out of the scope of this thesis.

7.1.3 Theoretical Model Approximations

The theoretical model developed in chapter 5 provides a description in the phase plane of the rotation of a jam and the dependency on dimensionless factors. However, the model is a simplified version of the actual phenomenon. The shape of the jam is idealised and although there is a good match between the polynomial function used and the actual shape observed, this is still an approximation. Another limitation is represented by the intervening forces adopted in the model. Drag is arguably the most important force acting on the jam-pier system, but other factors may affect the motion too, such as the pier-jam friction, viscous forces, lift forces, the drag force induced by the rotation of the jam. A further simplification is the assumption that the jam porosity is uniform across the jam structure and that the drag force is applied at the centroid of the debris jam. Despite the simplifications adopted in the formulation, the model provided a reasonable approximation of the actual phenomenon that provides the identification of key-processes observed experimentally, but a more accurate description might require the inclusion of forces and factors that have been neglected in this work.

7.2 Recommendations for Further Research

The research shown in this thesis represents a first step forward a robust assessment of woody debris accumulations at bridge piers. Despite the extensive experimental observations and the mechanistic analysis provided, there are still many aspects that will need to be developed with further research.

7.2.1 Scour, Flood Risk, and Mitigation Measures

Localised scour around a bridge pier is one of the main effects of the flow alteration induced by the pier-jam obstruction. While experimental research was conducted in the past to estimate the scour at a pier under debris accumulations, they adopted arbitrary shapes and sizes of debris accumulations. In fact, the size and shape of LWD accumulations can have a significant contribution in exacerbating the scour hole at the pier (Melville and Dongol, 1992; Pagliara and Carnacina, 2011a). Outputs from the research shown in this thesis will inform future experiments, allowing the introduction of the jam dimensions as new variables in the scour assessment.

Another key-factor to be considered for further research is the impact on flood risk. For example, blockage scenarios are typically included in Flood Risk Assessments; predicting the size that woody debris blockage may reach at bridge piers could be a significant improvement for

the accuracy of the models. However, current modelling approaches may not be representative of the actual increase in water level, e.g. adopting arbitrary energy losses. Further research should focus on how to estimate the afflux from both LWD blockage at a single pier and flow conditions, including also the dependency of the former on the latter.

Further research should also be focused on the mitigation measures that might be developed in order to reduce the risk of debris accumulations or limiting their effects. The experimental analysis and the theoretical model showed the processes that govern a debris accumulation formation. This can inform future studies on the development of measures aimed at minimising the size that a jam can reach (for example, considering those factors that are key for the stability of the jam).

7.2.2 Non-Isolated Piers

The main aim of this thesis was to study the accumulation of woody debris at single piers. Nevertheless, in many instances the isolated pier condition (i.e. the growth of a debris jam is not limited in any direction) is not possible. For example, this could be the case when adjacent piers are bridged by a debris, or when two or more jams (formed independently) are then bridged by additional debris elements. In other situations debris may interact with the boundaries of the channel, i.e. $W/B \approx 1$ and $H/h \approx 1$, in which further complexity is possible with a mobile bed. It is unclear how the formation and failure processes would change under these conditions, therefore additional research is needed in order to provide a wider and more comprehensive understanding of the accumulation of large woody debris at piers.

Appendix A

Further Dimensional Analysis

Section 3.1 described the dimensional analysis of the phenomenon of woody debris accumulations at bridge piers. The resulting functional relationship (3.2) is only one of the possible combinations of dimensionless groups that can be formed, since application of the Buckingham π-theorem allows a broad combination of dimensionless groups depending on the repeated groups chosen. Once a group is obtained, it can still be multiplied or divided by any of the other groups and forming a new group. Thus, any combination with a certain repeated group could be re-obtained with a different set of repeated variables with simple manipulations. The expected functional relationships will be in a form like

$$g\left(\pi_1, \pi_2, \pi_3, \pi_4, \pi_5, \pi_6, \pi_7, \pi_8, \pi_9\right) = 0.$$

The next section presents a list of many possible combinations of π-groups - depending on the repeated group used - that may provide additional insights and inform further research on the phenomena of debris accumulations at bridge piers.

A.1 Water Density ρ, Velocity v, and Debris Length L

This first combination of repeated quantities corresponds to those adopted in section 3.1.

The dimensionless group relatively to viscosity μ yields:

$$\pi_1 = \frac{\mu}{\rho v L},$$

that is the inverse of the Reynolds number having characteristic length the debris length L. The second group is the dimensionless form of g. This is

$$\pi_2 = \frac{gL}{v^2}.$$

The group π_2 corresponds to the inverse of the squared Froude number. It is interesting to observe that the first two π-groups are the most important dimensionless groups for fluid mechanics problems.
Groups with respect to h, d, D, W, H and K are all simple ratios with the debris length L (e.g. π_3=h/L). Similarly, the dimensionless group of debris density ρ_L is the ratio with the water density, i.e. π_6=ρ_L/ρ. Therefore, the functional relationship is

$$g\left(\frac{\mu}{\rho v L}, \frac{gL}{v^2}, \frac{h}{L}, \frac{d}{L}, \frac{D}{L}, \frac{\rho_L}{\rho}, \frac{W}{L}, \frac{H}{L}, \frac{K}{L}\right) = 0. \tag{A.1}$$

A.2 Viscosity μ, Gravity g, and Pier Width D

Group π_1 is relative to density ρ and yields

$$\pi_1 = \frac{\rho^2 D^3 g}{\mu^2},$$

that is the Galilei number Ga, the ratio between viscous and gravity forces. Likewise, the same group is obtained for ρ_L. The second relevant group is relative to velocity v. Once again, this is the squared Froude number having the pier width D as characteristic length, i.e. $\pi_2 = \frac{v^2}{gD}$. All the other variables are in a simple ratio with the pier width D. It is finally obtained

$$g\left(\frac{\rho^2 D^3 g}{\mu^2}, \frac{v^2}{gD}, \frac{h}{D}, \frac{d}{D}, \frac{L}{D}, \frac{\rho_L^2 D^3 g}{\mu^2}, \frac{W}{D}, \frac{H}{D}, \frac{K}{D}\right) = 0.$$

A.3 Water Density ρ, Gravity g, and Velocity v

The first π-group relates the repeated group with viscosity μ. As a result,

$$\pi_1 = \frac{\mu g}{\rho v^3},$$

that is the inverse of the product between Reynolds and squared Froude numbers. For all remaining terms with a length dimension, groups formed are the inverse of Froude numbers squared (e.g. $\pi_2 = \frac{hg}{v^2}$). For ρ_L, the resulting dimensionless group is the ratio with the water density, i.e. ρ/ρ_L. Therefore, the functional relationship becomes

$$g\left(\frac{\mu g}{\rho v^3}, \frac{gh}{v^2}, \frac{gD}{v^2}, \frac{gd}{v^2}, \frac{gL}{v^2}, \frac{\rho_L}{\rho}, \frac{gW}{v^2}, \frac{gH}{v^2}, \frac{gK}{v^2}\right) = 0.$$

A.4 Other Sets

The same approach is used for other repeated groups, which yields other sets of dimensionless groups. Table A.1 displays the first three sets with additional sets. Any other repeated group chosen outside of those shown in Table A.1 will have shown similar resulting groups.

Repeating group	π_1	π_2	π_3	π_4	π_5	π_6	π_7	π_8	π_9
$\rho\ v\ L$	$\frac{\mu}{\rho L v}$	$\frac{h}{L}$	$\frac{gL}{v^2}$	$\frac{D}{L}$	$\frac{d}{L}$	$\frac{\rho_L}{\rho}$	$\frac{W}{L}$	$\frac{H}{L}$	$\frac{K}{L}$
$\mu\ g\ D$	$\frac{\rho^2 D^3 g}{\mu^2}$	$\frac{v^2}{gD}$	$\frac{h}{D}$	$\frac{L}{D}$	$\frac{d}{D}$	$\frac{\rho_L^2 D^3 g}{\mu^2}$	$\frac{W}{D}$	$\frac{H}{D}$	$\frac{K}{D}$
$\rho\ g\ v$	$\frac{\mu g}{\rho v^3}$	$\frac{hg}{v^2}$	$\frac{Dg}{v^2}$	$\frac{Lg}{v^2}$	$\frac{dg}{v^2}$	$\frac{\rho_L}{\rho}$	$\frac{Wg}{v^2}$	$\frac{Hg}{v^2}$	$\frac{Kg}{v^2}$
$\rho\ g\ d$	$\frac{\mu^2}{\rho^2 g d^3}$	$\frac{v^2}{gd}$	$\frac{h}{d}$	$\frac{D}{d}$	$\frac{L}{d}$	$\frac{\rho_L}{\rho}$	$\frac{W}{d}$	$\frac{H}{d}$	$\frac{K}{d}$
$\rho\ \mu\ L$	$\frac{v\rho L}{\mu}$	$\frac{h}{L}$	$\frac{g\rho^2 L^3}{\mu^2}$	$\frac{D}{L}$	$\frac{d}{L}$	$\frac{\rho_L}{\rho}$	$\frac{W}{L}$	$\frac{H}{L}$	$\frac{K}{L}$
$\rho\ \mu\ v$	$\frac{h\rho v}{\mu}$	$\frac{g\mu}{\rho v^3}$	$\frac{D\rho v}{\mu}$	$\frac{L\rho v}{\mu}$	$\frac{d\rho v}{\mu}$	$\frac{\rho_L}{\rho}$	$\frac{W\rho v}{\mu}$	$\frac{H\rho v}{\mu}$	$\frac{K\rho v}{\mu}$
$\mu\ v\ L$	$\frac{\rho v L}{\mu}$	$\frac{h}{L}$	$\frac{gL}{v^2}$	$\frac{D}{L}$	$\frac{d}{L}$	$\frac{\rho_L}{\rho}$	$\frac{W}{L}$	$\frac{H}{L}$	$\frac{K}{L}$
$\mu\ g\ \rho$	$\frac{v^3 \rho}{\mu g}$	$\frac{h^3 \rho^2 g}{\mu^2}$	$\frac{D^3 \rho^2 g}{\mu^2}$	$\frac{L^3 \rho^2 g}{\mu^2}$	$\frac{d^3 \rho^2 g}{\mu^2}$	$\frac{\rho_L}{\rho}$	$\frac{W^3 \rho^2 g}{\mu^2}$	$\frac{H^3 \rho^2 g}{\mu^2}$	$\frac{K^3 \rho^2 g}{\mu^2}$

TABLE A.1: Dimensionless parameters for different repeating groups.

Appendix B

Calibrations

B.1 Mesh

The measurement of the jam size using the video recordings was possible by employing a reference mesh for each camera. For the top camera, a mesh with a ruled paper (10x10 mm squared) glued to a wooden board was used and photos captured at different heights at a distance of approximately 5 cm. This was necessary to take into account variations of the water depth (an example is shown in Figure B.1). For the lateral and submerged cameras the mesh was adapted by a wired net with a squared mesh of $^1/_2$ inches (12.7 mm) placed at the pier location (Figure B.2). These recorded pictures showing the mesh were then post-processed with a CAD (Computer-aided design) software (i.e. AutoCAD), drawing a polyline mesh over the captured pictures (an example is shown in Figure B.3). Geometrical data of the debris jams was computed by superimposing snapshots of the video recordings onto the polyline grid and then measuring directly the geometrical variables (Figure B.4 shows an actual example for measuring width W and length K). When water depth was not at the exact height as any of the top camera meshes, a linear interpolation was applied using the two closest mesh heights.

B.2 Ultrasonic Sensors

Ultrasonic sensors were calibrated comparing the recorded data with a point gauge for the range of flow levels used for the experiments. An example of these results (for the US4 sensor, the closest to the pier) is shown in Figure B.5. For each ultrasonic sensor a linear function was derived at each experimental campaign.

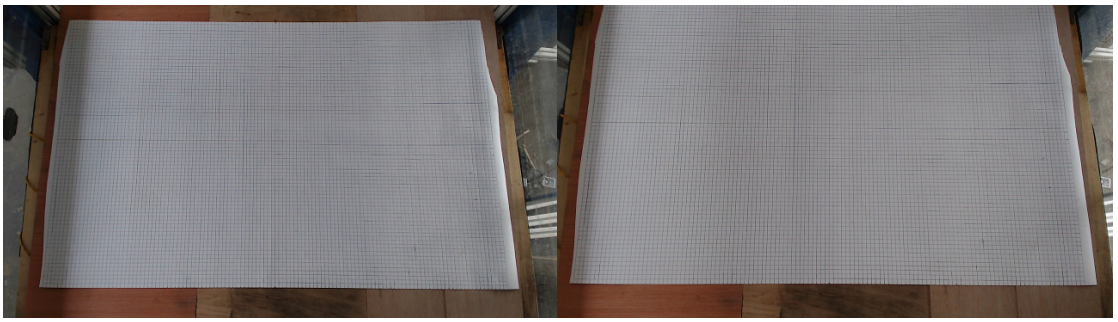

(A) h=31 cm (B) h=41 cm

FIGURE B.1: Ruled paper used as mesh at two different water depths captured by the top camera. Mesh size 10 mm.

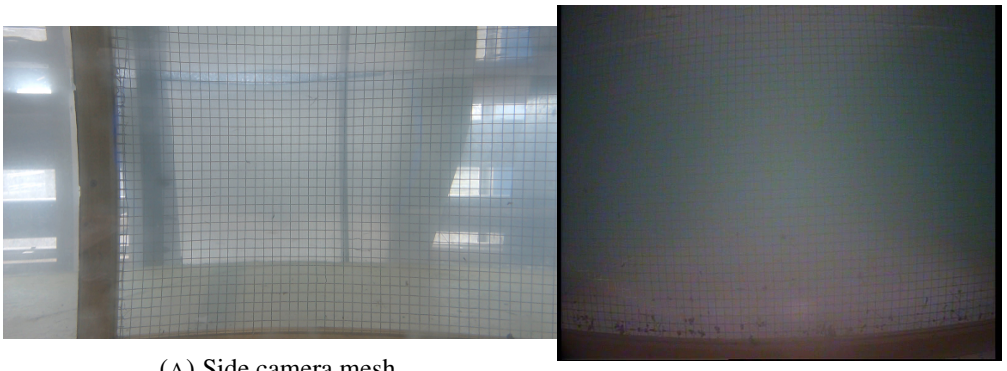

(A) Side camera mesh. (B) Underwater camera mesh.

FIGURE B.2: Meshes used for side (B.2a) and underwater (B.2b) camera.

B.3 Load Cell and Drag Force

The load cell was calibrated comparing measured data with a series of known weights attached to one end of the cell, i.e. weights were hung to the load cell and measured. Results of the calibration are shown in Figure B.6 and a linear relationship was derived.

In order to provide an accurate estimation of the drag coefficient, previous studies have partitioned the force exerted on the pier into drag and static components. The latter results from the difference in the hydrostatic forces induced by the drop in the free surface from upstream to downstream. Parola et al. (2000) estimated this static component as the hydrostatic force that would be exerted on a solid block with the same dimensions as the debris accumulation. For simplicity, this static force component was assumed negligible and the measured force was assumed to represent the drag force only. In order to understand the effects of debris on loadings, the total drag force measured by the load cell F_{Dt} must be decomposed into the drag force exerted on the debris F_{Dd} plus the drag exerted on the part of the pier that is below the accumulation F_{Dp}:

$$F_{Dt} = F_{Dd} + F_{Dp}.$$

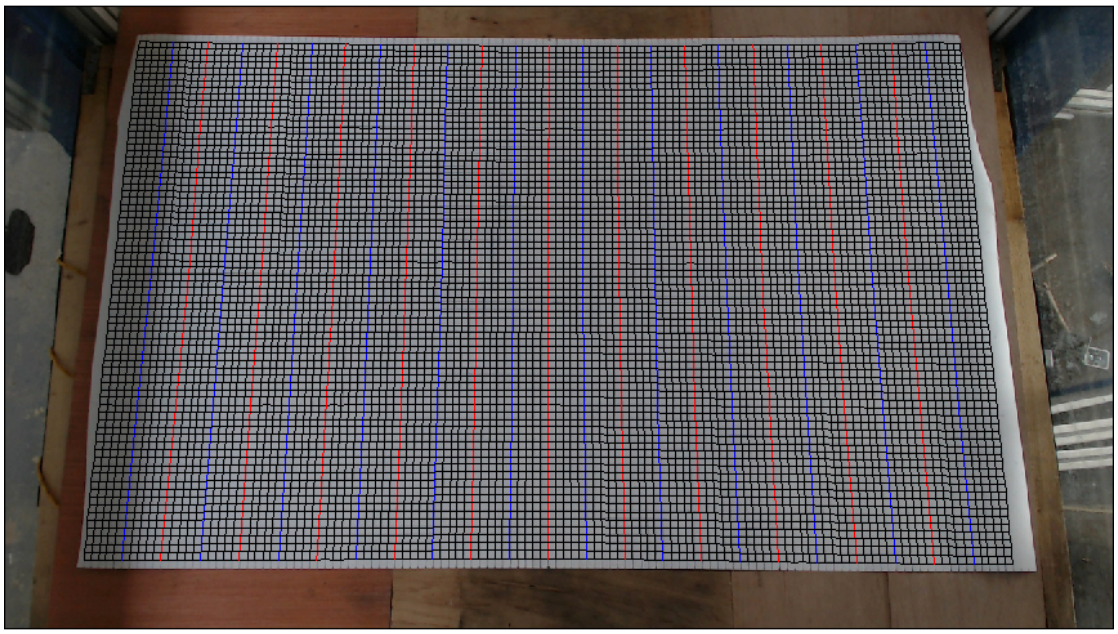

FIGURE B.3: Polylines drawn over the mesh snapshot at 31 cm height. Blue and red lines are placed at a distance of 5 cm for ease of understanding during data analysis.

The term F_{Dp} was estimated for each experiment using Reynolds dependent values of the drag coefficient for cylindrical bodies from the literature (Tritton, 1988) and the approach flow average velocity v_{ap}, i.e. the cross-section averaged velocity upstream of the debris jam in undisturbed conditions. This simplified approach (also adopted by Parola et al. (2000); Hygelund and Manga (2003); Manners et al. (2007)) is, however, only an approximation, as the flow field under the debris jam is complex (Pagliara and Carnacina, 2013). Nevertheless, measurements of velocity close to the pier by intrusive methods available were not possible as they would have disturbed the flow and influenced the process of growth of the jam. The estimated values of F_{Dd} thus obtained were used to determine the drag coefficient of the debris:

$$C_{Dd} = \frac{4F_{Dd}}{\rho W H v_{ap}^2}.$$

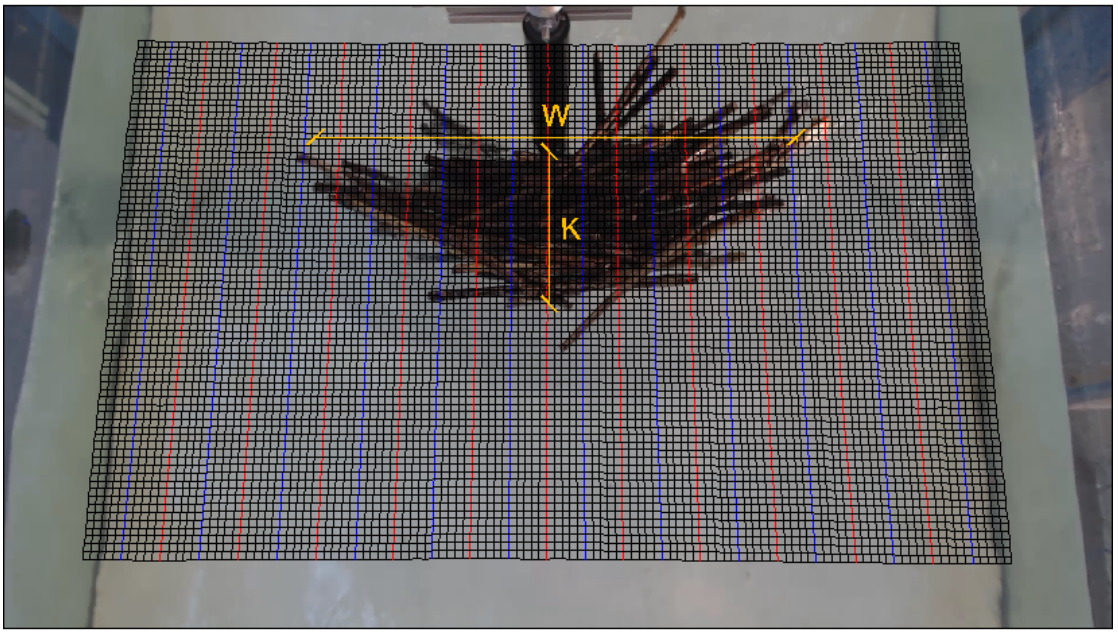

FIGURE B.4: An example of superimposition of the polyline mesh with a top camera snapshot. It is also shown the measured width W and length K.

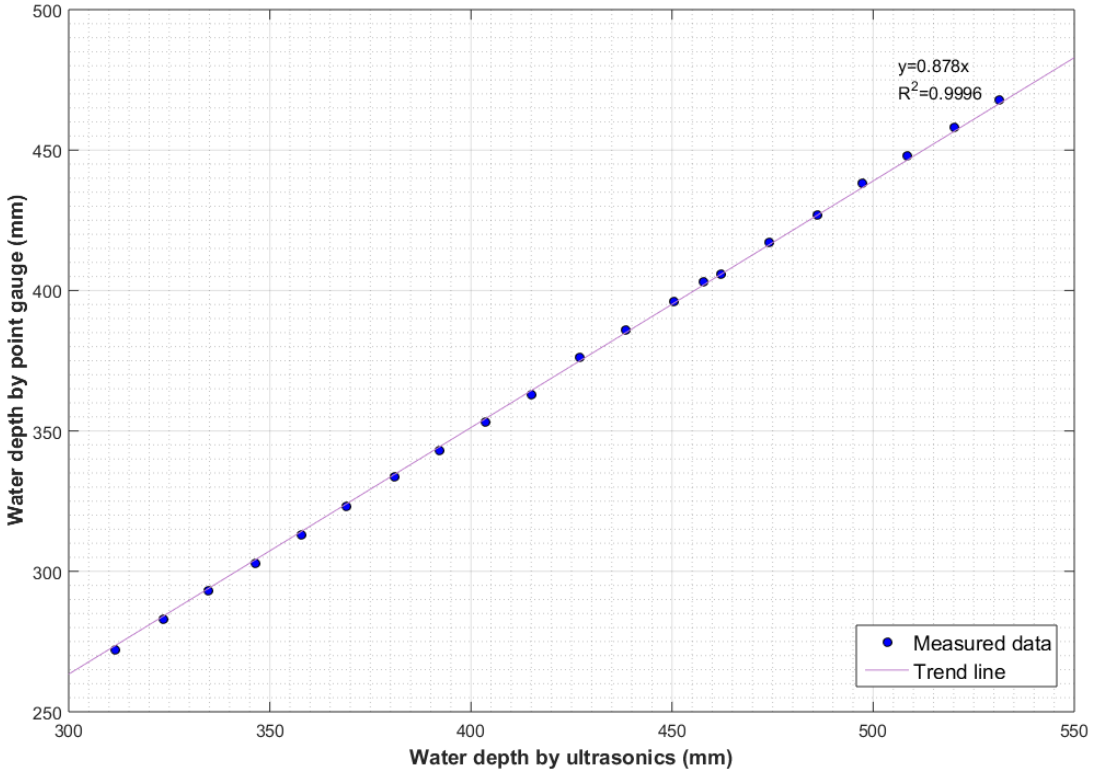

FIGURE B.5: Calibration data between water depth measured by ultrasonics (for the US4 sensor) and point gauge with the interpolating linear function.

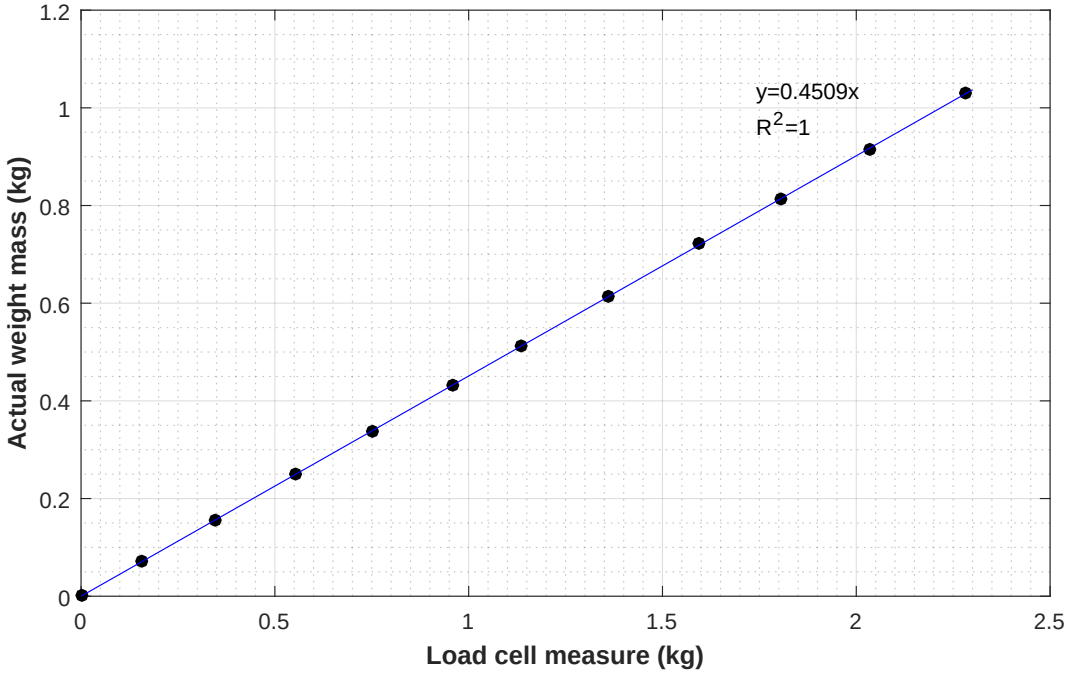

FIGURE B.6: Calibration data between weight mass measured by the load cell and the actual mass weighed.

Appendix C

Dimensional Results

Experimental results reported in chapter 4 are shown in the main text as dimensionless variables, derived by the dimensional analysis in (3.3). Nevertheless, the dimensional results may provide additional insights into the process of woody debris accumulations. In this appendix, dimensional values are shown for groups U1 to U5 and N1 to N13. All the other groups have been excluded since the debris length L is always the same (i.e. L=0.375 m) and therefore values on the vertical and horizontal axes are scaled by the same factor for all conditions.

Figure C.1 shows the dimensional results for W^c, H^c, and K^c on the vertical axis and the flow velocity v on the horizontal axis for groups U1 to U5. Unlike results in chapter 4, in which data points are clustered within a narrow band and that suggest no visible differences among groups, dimensional values are clearly distinguishable based on the length of the debris elements L for each group.

Figure C.2 depicts dimensional results for experimental groups N1 to N13, for which the element lengths are non-uniformly distributed. Similarly to uniform length debris, there is a clear and distinct pattern among experimental groups, which depends on the length of the debris key-element L, that is not observable when made dimensionless.

Some small gaps can be observed in the two figures (e.g. for $0.31 \leq v \leq 0.33$). These occurred when a switch between pumps was necessary (e.g. from one single pump to two pumps), but the minimum discharge delivered by individual pumps could not be reduced in order to cover the small gap. Nevertheless, these gaps are limited and showed no differences on the dimensionless variable Fr_L.

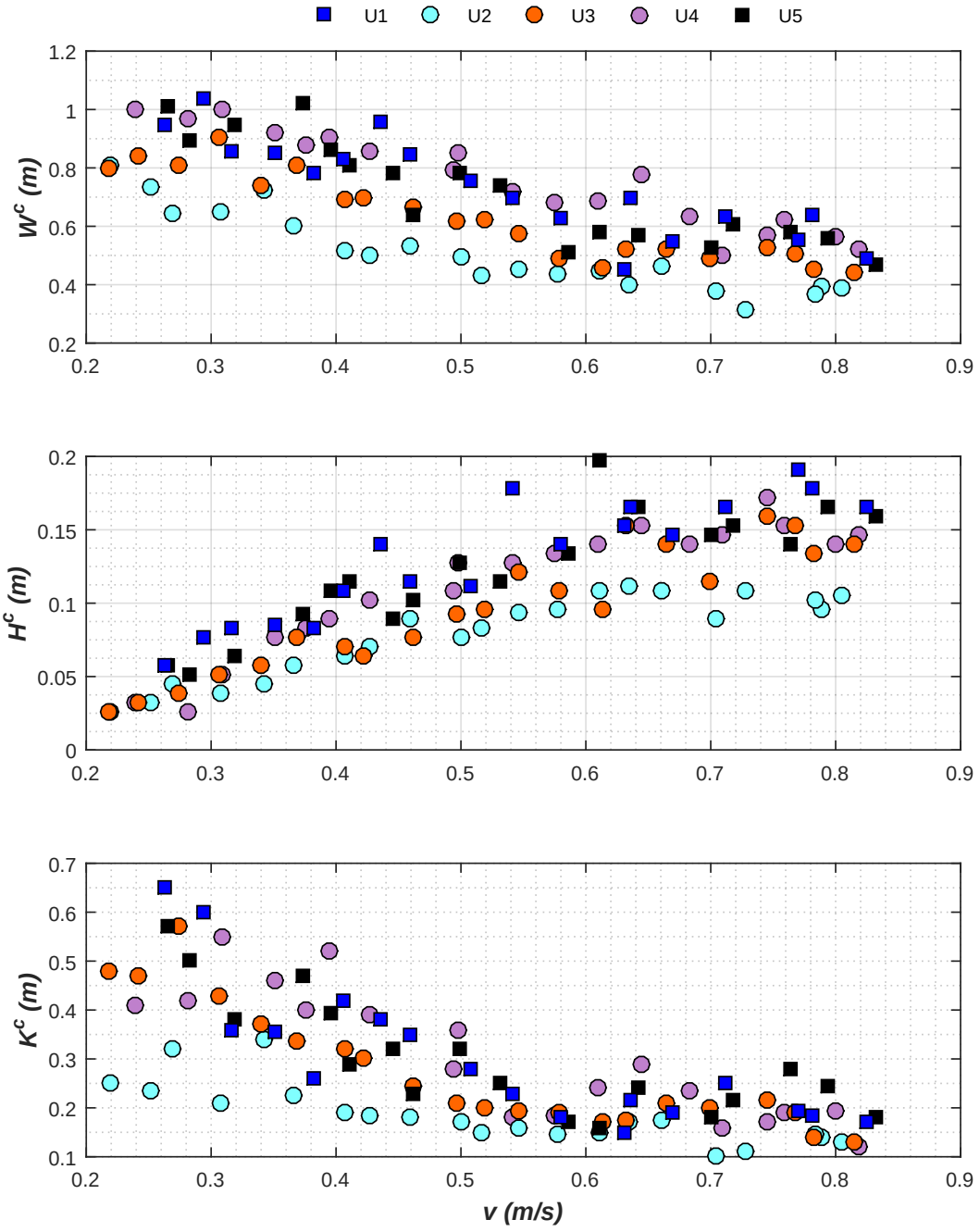

FIGURE C.1: Graph of dimensional results for experimental groups U1 to U5.

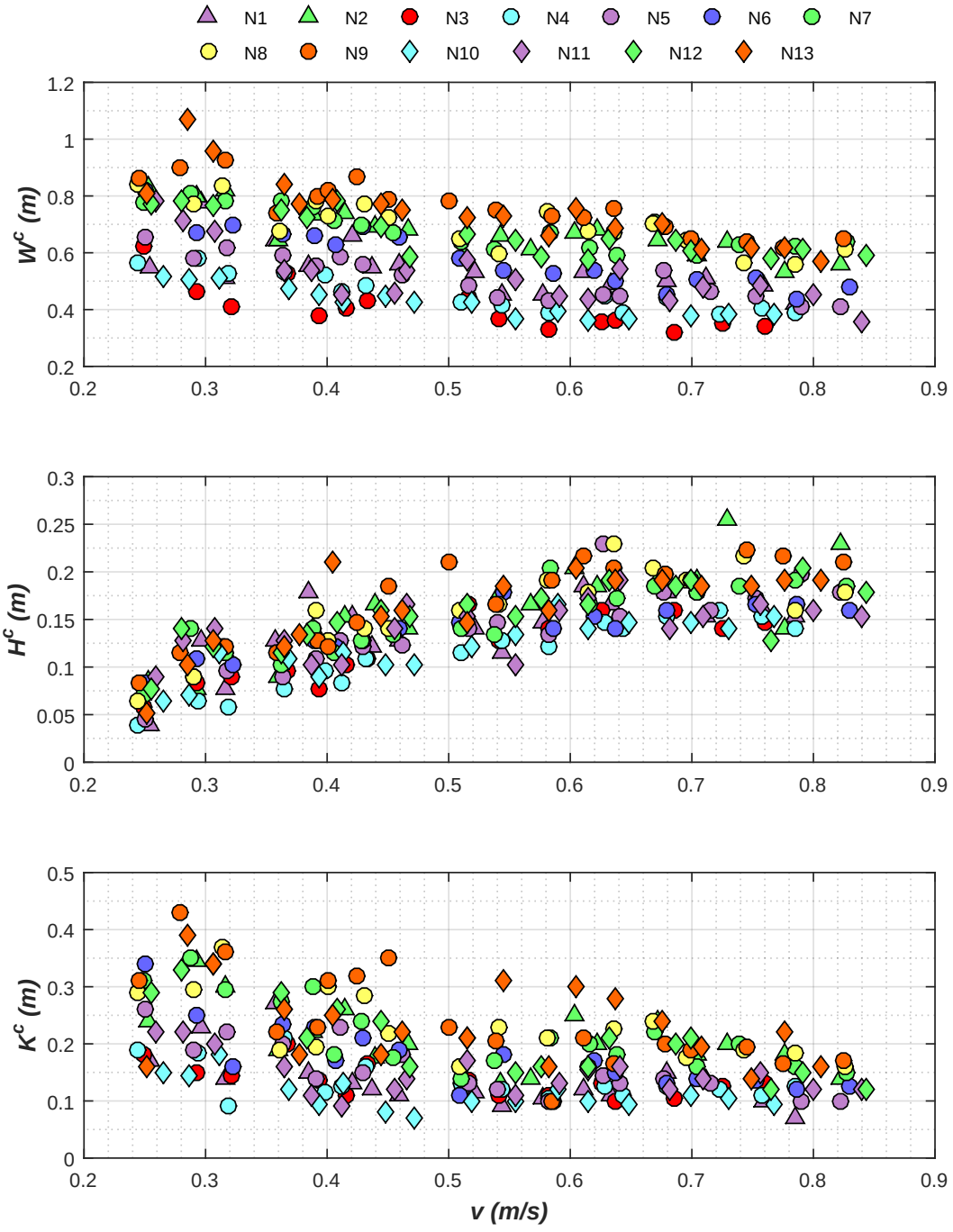

FIGURE C.2: Graph of dimensional results for experimental groups N1 to N13. Data markers with the same colour indicate same debris key-element length L.

Appendix D

Practical Application to the Case of Charles' Bridge in Prague

Woody debris accumulations at bridge piers were found to produce the failures of many bridges around the world. An emblematic example is the failure of Charles' Bridge in Prague during the 1890 flood, which is shown in Figure 1.1. On the night between 4th and 5th September 1890 during a severe flooding (the peak of which was characterised by a maximum discharge of 3970 m^3/s (Munzar, 1998; Müller and Kakos, 2003; Březina et al., 2014; Elleder, 2015) and water depth at the bridge section 506 cm (Brázdil et al., 2005)), three arches and two piers of the bridge collapsed (Munzar, 1998; Zeman et al., 2008) after being obstructed by a vast accumulation of large woody debris collected from rafts and construction timber in the upstream areas (Munzar, 1998; Brázdil et al., 2005). This large amount of wood significantly reduced the free flow surface and exerted additional loads to the pier, as well as exacerbating local scour and causing flow velocity acceleration Munzar (1998). The bridge destruction was regarded as a national disaster (Brázdil et al., 2005). There were severe disruptions to the main transport routes to the city, but most importantly one of the symbols of Prague was destroyed, which shook and profoundly disconcerted the Bohemian population of that time (Neruda, 1890; Munzar, 1998; Brázdil et al., 2005). The anthropic activities in the riverine areas upstream of the city favoured the mobilisation of a significant amount of logs, most of which showed uniform size. Could this event be avoided, or at least mitigated? In this study, the woody debris jams that had formed at Charles' bridge piers during the 1890 event are reproduced, with particular emphasis on the likelihood of bridging between adjacent accumulations. Then the resulting jam is compared with the accumulations that could have formed in a non-anthropised environment. The resulting method is a pioneering approach to assess the risk of large and extended blockages and will be potentially applied to any other bridge believed to suffer of heavy accumulations, significantly improving the ability to predict (and thus, prevent or mitigate) such catastrophic events.

The dimensionless width of debris accumulations in (4.2) and (4.3) can be written as

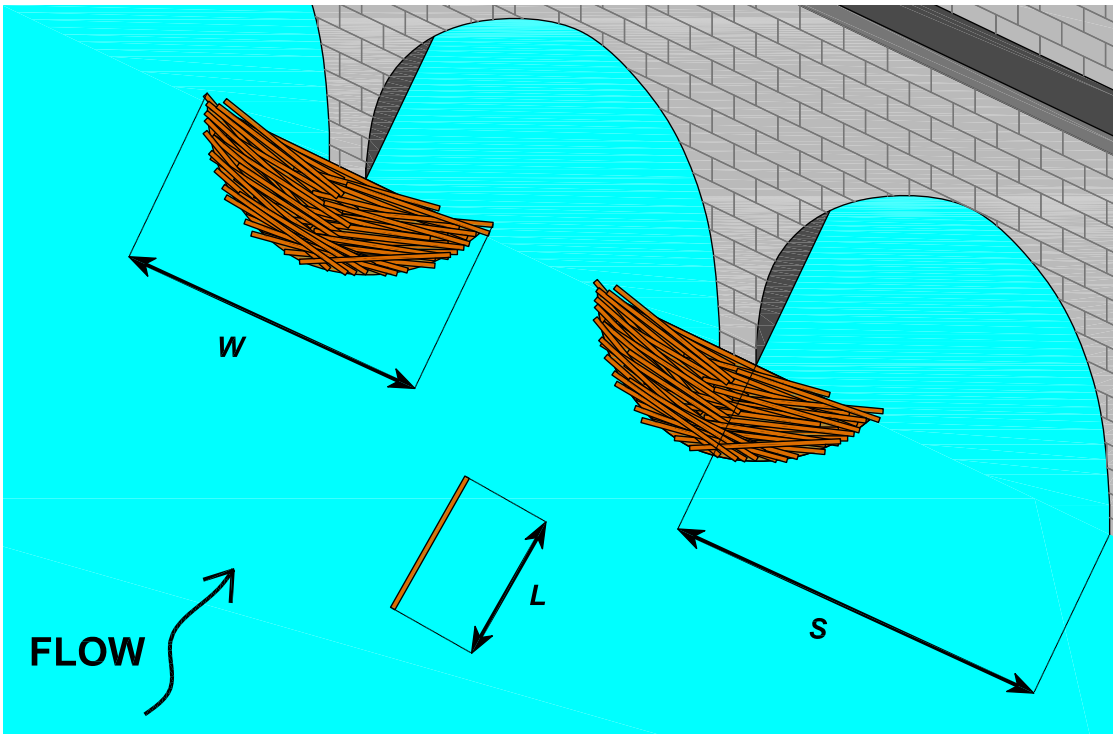

FIGURE D.1: Sketch of two bridge openings with debris accumulations at each pier. Debris width W, span width S, and debris length L are indicated.

$$\omega^c = a + be^{-cFr_L} \tag{D.1}$$

in which a, b, and c are regression parameters and differ between debris having uniform and non-uniform length. Equation (D.1) is referred to the idealised case in which an accumulation occurs to a single isolated pier. However, to obstruct an entire bridge opening a more complex process may occur. Figure D.1 shows a sketch of single pier accumulations at a bridge and the distance between two jams both reaching their maximum size. The likelihood that two jams at adjacent piers can be bridged by an oncoming debris depends on the width of the debris jam W, the span width S, and the length of an individual debris element L. It is here defined a span capacity factor σ:

$$\sigma = \frac{S - W}{L} = \frac{S}{L} - \omega, \tag{D.2}$$

whereby the probability of bridging (P_B) two adjacent debris jams can be assumed as:

$$P_B = \begin{cases} 0.0 & \text{for } \sigma > 1 \\ 0.0 < P_B < 1 & \text{for } 0 < \sigma \leq 1 \\ 1.0 & \text{for } \sigma = 0 \end{cases}$$

Combining together equations (D.1) and (D.2) for ω=ω^c, the span capacity σ is found as a function of approach velocity v and debris length L if the span length S is known. This means

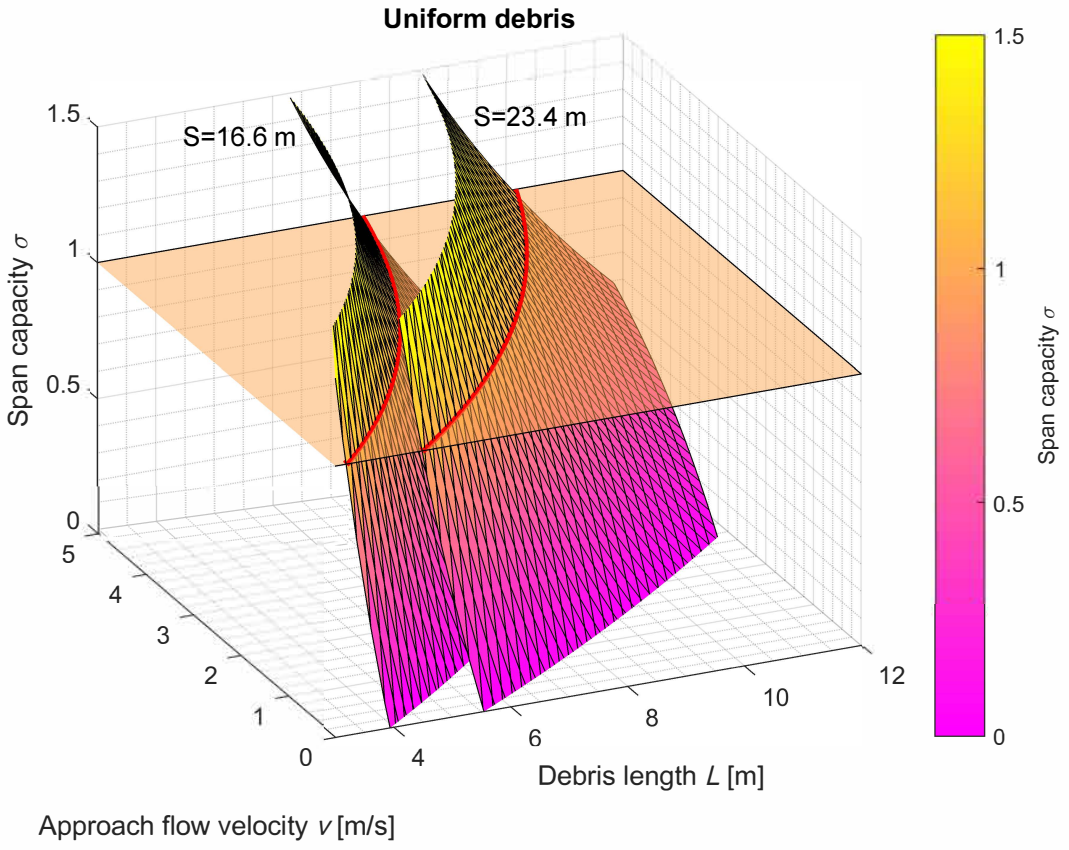

FIGURE D.2: Span capacity factor σ mapping for any given approach velocity v and debris elements length L in the uniform length debris case. The maps are referred to the smallest (16.6 m) and largest (23.4 m) spans lengths of Charles' bridge. The red curves represent the intersection between the map and the planes.

that σ can be mapped for any values of v and L, depending only on the parameters of equation (D.1). Figures D.2 and D.3 show the 3-dimensional mapping of the span capacity σ for uniform and non-uniform length debris for varying velocity and debris length under the two span widths of Charles' bridge, that are 16.6 m and 23.4 m respectively. To assess whether the span blockage of a bridge is likely, the interception between the 3D map and a plane for σ=1 defines two areas where, respectively, bridging between jams is unlikely (i.e. $\sigma>1$) and span blockage is likely (i.e. $\sigma\leq1$). The projection of this intersection onto the L-v plane defines the same limits for values of approach velocity and debris length. A limit function can be obtained from equation (D.2): at the limit value for which a bridging is considered likely (i.e. σ=1) and employing the debris length as independent variable and approach velocity as dependent variable (only for analytical purposes), yields

$$v = -\frac{\sqrt{gL}}{c} \ln\left[\frac{\frac{S}{L} - (a+1)}{b}\right]. \tag{D.3}$$

Figures D.5 and D.6 show the projection on the length-velocity plane of the span capacity for respectively the smallest and largest bridge spans of the Charles' bridge for both uniform and

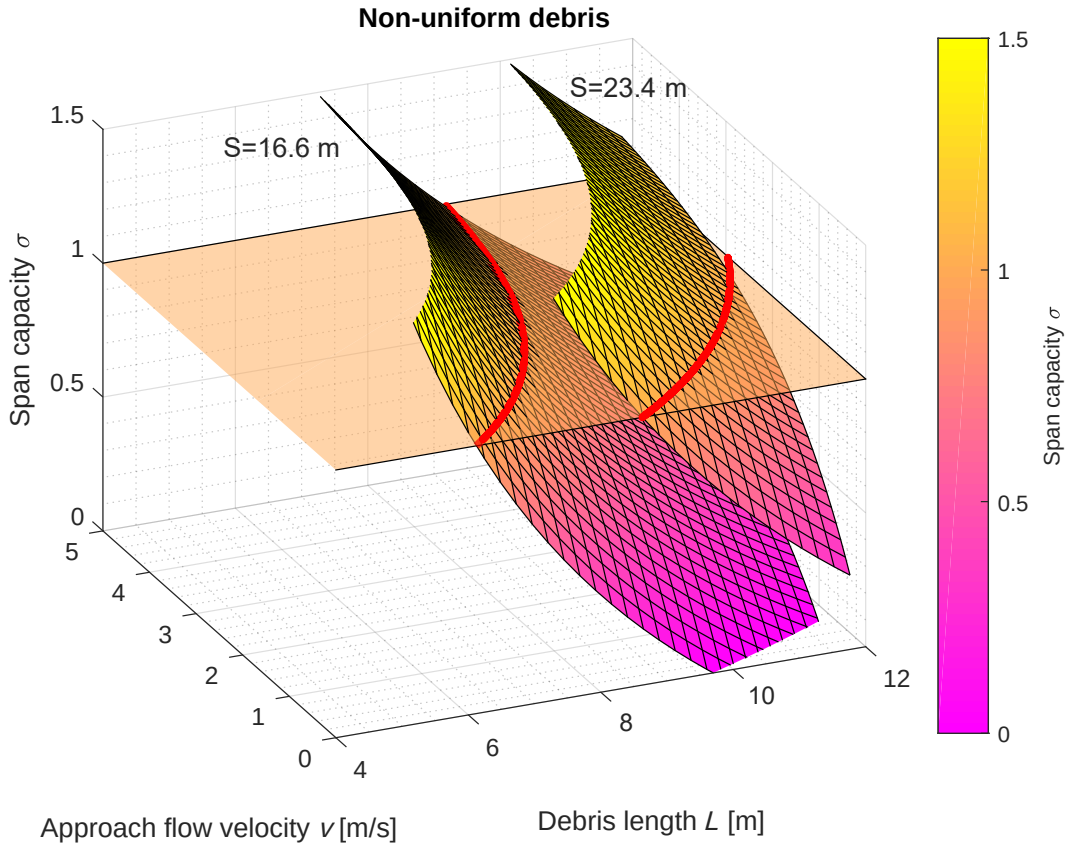

FIGURE D.3: Span capacity factor σ mapping for any given approach velocity v and debris elements length L in the non-uniform length debris case. The maps are referred to the smallest (16.6 m) and largest (23.4 m) spans lengths of Charles' bridge. The red curves represent the intersection between the map and the planes.

non-uniform length debris. The interpretation of these figure is as follows: any accumulations formed under values of approach velocity v and debris length L on the left of each curve would result in a bridge span length that is unlikely to result in a bridging effect - i.e. $\sigma>1$. On the other hand, if an accumulation were to form with v and L values on the right of the curve, the maximum expected accumulations at two adjacent piers might result in a bridging effect since $\sigma\leq1$ and a bridging between adjacent debris jams is likely; hence, a large and potentially significantly more destructive woody debris accumulation can form. The figures also highlight that accumulations formed by uniform length debris are substantially more prone to span blockage than those formed by non-uniform length elements.

In these figures, Charles' bridge data is represented by the green shaded area. The flow velocity approaching the bridge is estimated through the hydrological data available for the event. Being discharge and flow depth known, the river width (and assuming a rectangular cross-section) would give the average velocity. Although the total bridge length is 516 m, part of it is used by the old town mills, which reduces the overall available area. The approach velocity at the

flood peak can then be assumed to be within the interval of 1.32 (full bridge width) to 2.27 (partial bridge width) m/s. These velocity values are lower than those reconstructed at the bridge approach cross-section for the epochal European flooding in 2002 (Zeman et al., 2008) which is reasonably consistent with the different discharges between the two events, since the return period of the 1890 event was 100 years, whereas for the 2002 event was 500 years (peak discharge of 5250 m^3/s). On the other hand, the data relatively to the debris length was obtained through scaling of the photos taken after the event during the debris removal (an example is provided in Figure D.4), in which the height of the men at the debris removal work can be used as a reference. The average height of a man in central Europe at the end of the 19th century was estimated as between 1.66 m and 1.70 m (Hatton and Bray, 2010), thus the length of the accumulated logs were likely to be in the interval between 7.10 and 8.80 m.

The area highlighted in figures D.5 and D.6 represents the range of velocity and debris lengths that presumably occurred during the 1890 flooding. Consistently with the actual event, the smallest span (16.6 m opening) was beyond the span capacity limit with uniform debris. The largest span (23.4 m opening) shows a better performance, although the vast majority of the plausible data area lies beyond the span capacity (i.e. potential blockage), which is what occurred during the actual event. Nevertheless, the results are totally different when considering non-uniform debris. For the smallest span, the condition $\sigma>1$ is satisfied for the majority of possible combinations, while a minority part would be more likely of bridging accumulations. Therefore, it is reasonable to assume that the likelihood of the bridging between two adjacent accumulations was low. The situation is clearly different for the largest span: here it can be observed that span blockage is unlikely and only a dramatic increase of the debris length may yield a more likely blockage.

Considerations about the aforementioned results are twofold: first, if the upstream section of the Vltava river would have been kept clear of anthropic woody debris (e.g. rafts and logging), it is unlikely that large accumulations could have formed, potentially avoiding the bridge failure. In fact, the widest spans corresponded to those that collapsed during the event, while the analysis here proposed clearly indicates that a span blockage was unlikely with non-uniform length debris. Second, the method adopted for this study is applicable to any existing bridge which is at risk of debris accumulations and in which two or more adjacent piers can form debris jams, since equation (D.1) is valid for any conditions (the only constraint of which is the debris Froude number Fr_L) and the limit function is used to assess the risk that a bridge has to get completely clogged or that only a single pier accumulation develops.

In conclusion, the large and potentially destructive woody debris accumulation that occurred to Charles' bridge in Prague during the September 1890 event could have been avoided. Simple restrictive measures regarding the use of rafts and timber wood could have significantly changed the outcome of such a destructive event. Furthermore, the analysis carried out in this study paves

FIGURE D.4: Accumulated debris at Charles' Bridge during the 1890 flood. The photo shows the relatively uniform length logs and the people working on the debris removal. Source: Museum of Prague.

the way to scientists and engineers for a totally new approach regarding this underestimated hazard from the anthropic use of the territory. Logging or systematic reintroduction of large woody debris in streams should be limited only to biodiversity purposes and when not possible otherwise, adequate countermeasures should be in place.

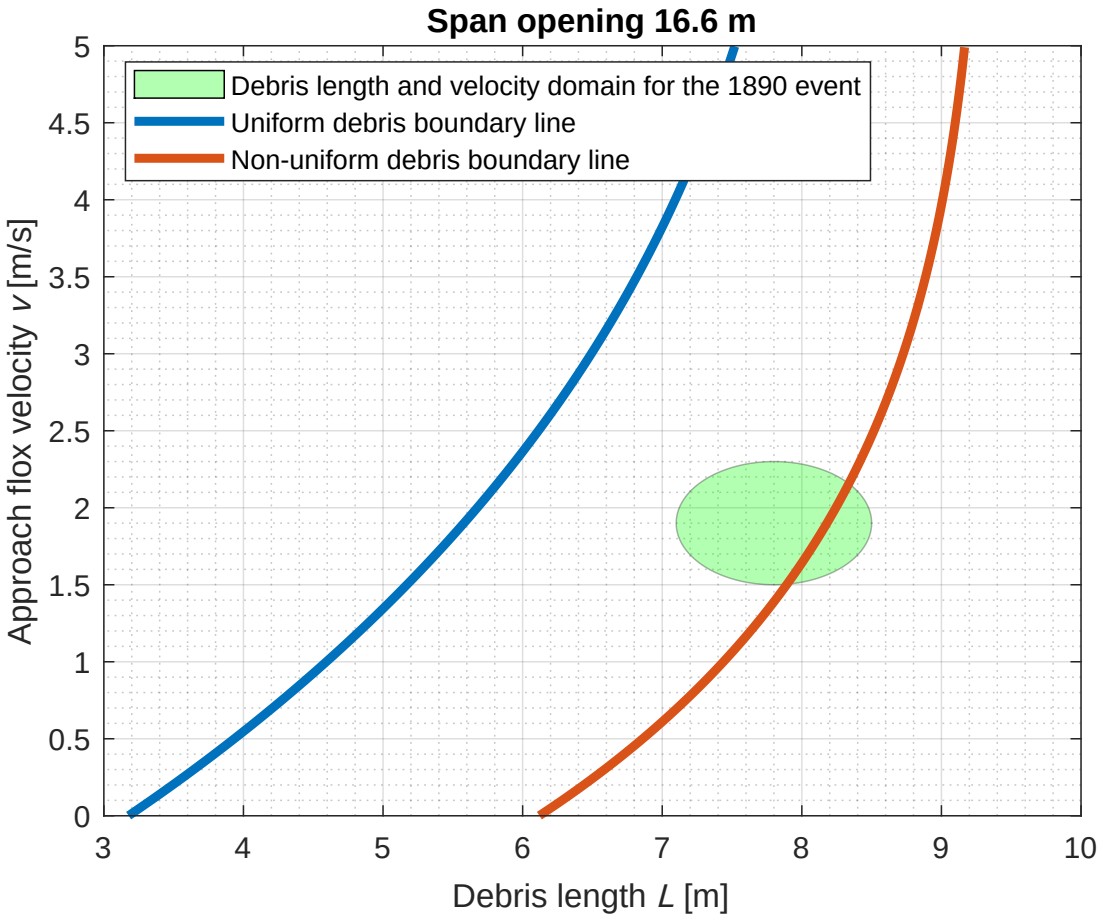

FIGURE D.5: Boundary function according to equation (D.3) for the span opening of 16.6 m. Accumulation resulting from approach velocity v and debris element length L on the left-hand side of each curve would result in the likelihood of a single pier accumulation, while those on the right-hand side would be likely to cause a bridging effect between adjacent piers.

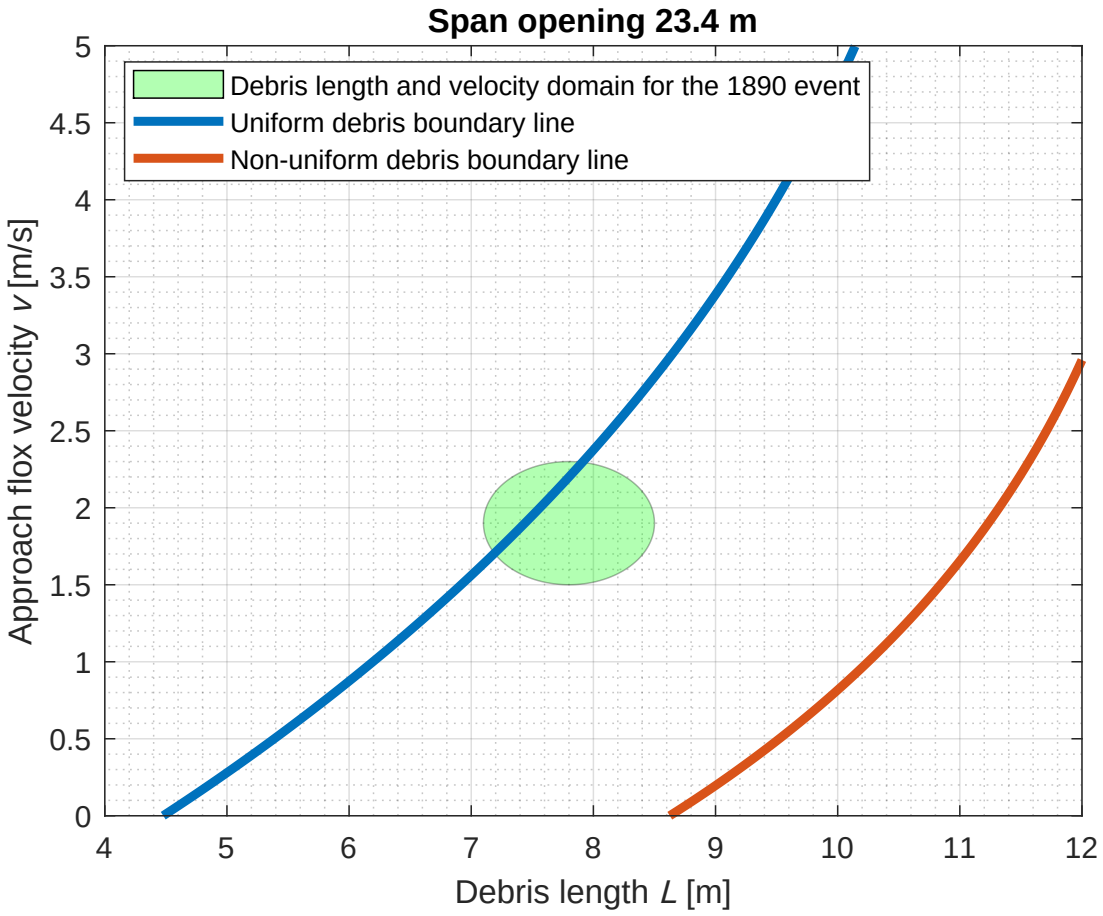

FIGURE D.6: Boundary function according to equation (D.3) for the span opening of 23.4 m. Accumulation resulting from approach velocity v and debris element length L on the left-hand side of each curve would result in the likelihood of a single pier accumulation, while those on the right-hand side would be likely to cause a bridging effect between adjacent piers.

Bibliography

Abbe, T. and Montgomery, D. (1996). Large woody debris jams, channel hydraulics and habitat formation in large rivers. *Regulated rivers: research and management*, 12:201–221.

Abbe, T. and Montgomery, D. (2003). Patterns and processes of wood debris accumulation in the Queets river basin, Washington. *Geomorphology*, 51:81–107.

Ahmed, F. and Rajaratnam, N. (1998). Flow around bridge piers. *Journal of Hydraulic Engineering*, 124:288–300.

Balachandar, R. and Patel, V. C. (2002). Rough wall boundary layer on plates in open channels. *Journal of Hydraulic Engineering*, 128:947–951.

Benn, J. (2013). Railway bridge failure during flooding in the uk and ireland. *Proceedings of the Institution of Civil Engineers*, 166:163–170.

Blersch, C. and Kangas, P. (2014). Signature of self-assembly in size distributions of 544 wood members in dam structures of *Castor canadiensis*. *Global Ecology and Conservation*, 2:204–213.

Bocchiola, D., Rulli, M., and Rosso, R. (2006). Transport of large woody debris in the presence of obstacles. *Geomorphology*, 76:166–178.

Bocchiola, D., Rulli, M., and Rosso, R. (2008). A flume experiment on the formation of wood jams in rivers. *Water Resources Research*, 44.

Bradley, J., Richards, D., and Bahner, C. (2005). Debris control structures evaluation and countermeasures. Report, Federal Highway Administration.

Braudrick, C. A. and Grant, G. E. (2000). When do logs move in rivers? *Water Resources Research*, 36(2):571–583.

Braudrick, C. A., Grant, G. E., Ishikawa, Y., and Ikeda, H. (1997). Dynamics of wood transport in streams: A flume experiment. *Earth surface processes and landforms*, 22:669–683.

Brázdil, R., Dobrovolný, P., Elleder, L., Kakos, V., Kotyza, O., Květoň, V., Macková, J., Müller, M., Štekl, J., Tolasz, R., and Valášek, H. (2005). Historical and recent floods in czech republic, history of weather and climate in the czech land, volume vii. Report, Masaryk University in Brno - Czech Hydrometeorological Institute in Prague, Brno.

Březina, K., Čekal, R., Drbola, L., Chroumal, J., Juráň, S., Kladivo, J., Kříž, T., Kubát, J., Petr, J., Polách, D., Roll, M., Sandev, M., Střeštík, J., Šercl, P., Šikula, J., Štěpánková, P., Tanajewski, M., and Vaňková, Z. (2014). Floods in the czech republic in june 2013. Report, Czech Hydrometeorological Institute.

Cadol, D. and Wohl, E. (2010). Wood retention and transport in tropical, headwater streams, La Selva Biological Station, Costa Rica. *Geomorphology*, 123:61–73.

Crosato, A., Rajbhandari, N., Comiti, F., Cherradi, X., and Uijttewaal, W. (2013). Flume experiments on entrainment of large wood in low-land rivers. *Journal of Hydraulic Research*, 51(5):581–588.

Curran, J. (2010). Mobility of large woody debris (LWD) jams in a low gradient channel. *Geomorphology*, 116:320329.

Da Deppo, L., Datei, C., and Salandin, P. (2004). *Sistemazione dei corsi d'acqua*. Cortina, Padua.

Daniels, M. and Rhoads, B. (2004). Effect of LWD configuration on spatial patterns of three-dimensional flow in two low-energy meander bends at varying stages. *Water Resources Research*, 40(11).

Dargahi, B. (1989). The turbulent flow field around a circular cylinder. *Experiments in fluids*, 8:1–12.

Dargahi, B. (1990). Controlling mechanism of local scouring. *Journal of Hydraulic Engineering*, 116(10):1197–1214.

De Cicco, N., Paris, E., and Solari, L. (2016). Wood accumulation at bridges: Laboratory experiments on the effect of pier shape. In *River Flow 2016*.

Dey, S. and Raikar, R. (2007). Characteristics of horseshoe vortex in developing scour holes at piers. *Journal of Hydraulic Engineering*, 133:399–413.

Diehl, T. H. (1997). Potential drift accumulation at bridges. Report, U.S. Department of Transportation Federal Highway Administration.

Elleder, L. (2015). Historical changes in frequency of extreme floods in prague. *Hydrology and Earth System Sciences*, 19:4307–4315.

Elliot, C. R., Froehlich, D. C., and MacArthur, R. C. (2012). Calculating the potential effects of large woody debris accumulations on backwater, scour, and hydrodinamic loads. In *World Environmental and Water Resources Congress 2012*, pages 1213–1222.

Environment Agency (2009). Flooding in England: A national assessment of flood risk. Report, Environment Agency.

Fulford, J. and Kimball, S. (2015). Hydraulic laboratory testing of SonTek-IQ Plus. Report, U.S. Geological Survey.

Gippel, C., Finlayson, B., and O'Neill, I. (1996a). Distribution and hydraulic significance of large woody debris in a lowland Australian river. *Hydrobiologia*, 318:179–194.

Gippel, C., O'Neill, I., Finlayson, B., and Schnatz, I. (1996b). Hydraulics guidelines for the reintroduction and management of large woody debris in lowland rivers. *Regulated rivers: research and management*, 12:223–236.

Gregory, K., Davis, R., and Tooth, S. (1993). Spatial distribution of coarse woody debris dams in the Lymington Basin, Hampshire, UK. *Geomorphology*, 6:207–224.

Gschnitzer, T., Gems, B., Mazzorana, M., and Aufleger, M. (2017). Towards a robust assessment of bridge clogging processes in flood risk management. *Geomorphology*, 279:128–140.

Gurnell, A., Piégay, H., Swanson, F., and Gregory, S. (2002). Large wood and fluvial processes. *Freshwater Biology*, 47:601–619.

Hatton, T. and Bray, B. (2010). Long run trends in the heights of european men, 19th-20th centuries. *Economics and Human Biology*, 8:405–413.

Heller, V. (2011). Scale effects in physical hydraulic engineering models. *Journal of Hydraulic Research*, 49:293–306.

Heller, V. (2017). Self-similarity and reynolds number invariance in froude modelling. *Journal of Hydraulic Research*, 55:293–309.

Hess, J. (2007). Distribution and residence times of Large Woody Debris along South River, Shenandoah Valley, Virginia. Master's thesis, University of Delaware.

Hygelund, B. and Manga, M. (2003). Field measurements of drag coefficients for model large woody debris. *Geomorphology*, 51:175–185.

Johnson, K. R. and King, F. C. K. (2003). Measurements of water surface profile and velocity field at a circular pier. *Journal of Engineering Mechanics*, 129:502–513.

Lagasse, P., Colopper, P., Zevenbergen, L., Spitz, W., and Girard, L. (2010). Effects of debris on bridge pier scour. Report, Transportation Research Board.

Lassettre, N. S. and Kondolf, G. M. (2012). Large woody debris in urban stream channels: redefining the problem. *River research and applications*, 28:1477–1487.

Linstead, C. and Gurnell, A. (1999). Large wood debris in British headwater rivers. Report, Environment Agency.

Lucía, A., Comiti, F., Borga, M., Cavalli, M., and Marchi, L. (2015). Dynamics of large wood during flash flood in two mountain catchments. *Natural Hazards and Earth System Sciences*, 15:1741–1755.

Lyn, D., Cooper, T., Condon, C., and Gan, L. (2007). Factors in debris accumulation at bridge piers. Report, Federal Highway Administration.

Lyn, D., Cooper, T., Yi, Y., Sinha, R., and Rao, A. (2003). Debris accumulation at bridge crossing: Laboratory and field studies. Report, Federal Highway Administration.

Máčka, Z., Krejčí, L., Loučková, B., and Peterková, L. (2011). A critical review of field techniques employed in the survey of large woody debris in river corridors: a central European perspective. *Environmental Monitoring and Assessing*, 181:291–316.

MacVicar, B. and Piégay, H. (2012). Implementation and validation of video monitoring for wood budgeting in a wandering piedmont river, the Ain River (France). *Earth Surface Processes and Landforms,*, 37:1272–1289.

Manners, R. B. and Doyle, M. W. (2008). A mechanistic model of woody debris jam evolution and its application to wood-based restoration and management. *River Research and Applications*, 24:1104–1123.

Manners, R. B., Doyle, M. W., and Small, M. J. (2007). Structure and hydraulics of natural woody debris jams. *Water Resources Research*, 43.

Melville, B. W. (2008). The physics of local scour at bridge piers. In *Fourth International Conference on Scour and Erosion*.

Melville, B. W. and Dongol, D. (1992). Bridge pier scour with debris accumulation. *Journal of Hydraulic Engineering*, 118:1306–1310.

Melville, B. W. and Sutherland, A. (1988). Design method for local scour at bridge piers. *Journal of Hydraulic Engineering*, 114(10):1210–1226.

Müller, M. and Kakos, V. (2003). Hydrometeorogické srovnání povodní v srpnu 2002 s vybranými historickými případy dešťových povodní na vltavě v praze [hydrometeorogical comparison between the floods in august 2002 and selected historical rain floods on the vltava river]. *Metereologické zprávy*, 56:129–136.

Munzar, J. (1998). Města a nebezpečné hydrometeorologické jevy [cities and hazardous hydrometeorological effects]. *Documenta Pragensia*, XVI:287–303.

Muzzammil, M., Gangadharaiah, T., and Gupta, A. (2004). An experimental investigation of a horseshoe vortex induced by a bridge pier. *Water Management*, 157:109–119.

Myers, L., Shah, K., and Galloway, P. (2013). Design, commissioning and performance of a device to vary the turbulence in a recirculating flume. In *EWTEC*.

Neruda, J. (1890). Fejeton ze 6. září 1890 [notes from 6th september 1890]. Report, Národní listy 7. září 1890.

Pagliara, S. and Carnacina, I. (2010). Temporal scour evolution at bridge piers: effect of wood debris roughness and porosity. *Journal of Hydraulic Research*, 48(1):3–13.

Pagliara, S. and Carnacina, I. (2011a). Influence of large woody debris on sediment scour at bridge piers. *International Journal of Sediment Research*, 26(2):121–135.

Pagliara, S. and Carnacina, I. (2011b). Influence of wood debris accumulation on bridge pier scour. *Journal of Hydraulic Engineering*, 137:254–261.

Pagliara, S. and Carnacina, I. (2013). Bridge pier flow field in the presence of debris accumulation. *Proceedings of the Institution of Civil Engineers*, 166(WM4):187–198.

Panici, D. and de Almeida, G. A. (2017). Understanding the formation of woody debris jams at bridge piers. In *IAHR 37th World Congress*.

Panici, D. and de Almeida, G. A. (2018). Formation, growth, and failure of debris jams at bridge piers. *Water Resources Research*, 54:6226–6241.

Panici, D. and de Almeida, G. A. (2019). The importance of debris shape in experiments on woody debris accumulations at bridge piers. In *IAHR 38th World Congress*.

Parola, A. C., Apelt, C. J., and Jempson, M. A. (2000). Debris forces on highway bridges. Report, NCHRP.

Pert, G. (2013). *Introductory Fluid Mechanics for Physicists and Mathematicians*. Wiley, Chichester (UK).

Pfister, M., Capobianco, D., Tullis, B., and Schleiss, A. (2013). Debris-blocking sensitivity of piano key weirs under reservoir-type approach flow. *Journal of Hydraulic Engineering*, 139:1134–1141.

Robison, E. G. and Beschta, R. L. (1990). Identifying trees in riparian areas that can provide coarse woody debris to streams. *Forest Science*, 36(3):790–801.

Ruiz-Villanueva, V., Bladé-Castellet, E., Díez-Herrero, A., Bodoque, J., and Sánchez-Juny, M. (2014). Two-dimensional modelling of large wood transport during flash floods. *Earth surface processes and landforms*, 39:438–449.

Ruiz-Villanueva, V., Bodoque, J., Díez-Herrero, A., Eguibar, M., and Pardo-Igúzquiza, E. (2013). Reconstruction of a flash flood with large wood transport and its influence on hazard patterns in an ungauged mountain basin. *Hydrological processes*, 27:34243437.

Rusyda, M., Hashimoto, H., and Ikematsu, S. (2014). Log jam formation by an obstruction in a river. In *River Flow 2014*.

Sayers, P., Horritt, M., Penning-Rowsell, E., and McKenzie, A. (2016). Climate Change Risk Assessment 2017 - Projections of future flood risk in the UK. Report, Committee on Climate Change, UK.

Schalko, I., Schmocker, L., Weitbrecht, V., and Boes, R. (2018). Backwater rise due to large wood accumulations. *Journal of Hydraulic Engineering*, 144.

Schmocker, L. and Hager, W. H. (2011). Probability of drift blockage at bridge decks. *Journal of Hydraulic Engineering*, 137.

Schmocker, L. and Weitbrecht, V. (2013). Driftwood: Risk analysis and engineering measures. *Journal of Hydraulic Engineering*, 139:683–695.

Sedell, J., Bisson, P., F.J., S., and Gregory, S. (1988). *From the forest to the sea: a story of fallen trees. Chapter 3. What we know about large trees that fall into streams and rivers*. U.S. Department of Agriculture, Forest Service, Pacific Northwest Research Station; U.S. Department of the Interior, Bureau of Land Management, Portland, OR (US).

Sheeder, S. and Johnson, P. (2008). Controlling debris at pennsylvania bridges. Report, Pennsylvania Department of Transportation.

Stockstill, R. L., Daly, S. F., and Hopkins, M. A. (2009). Modeling floating objects at river structures. *Journal of Hydraulic Engineering*, 135.

Strogatz, S. H. (2015). *Nonlinear dynamics and chaos*. Westview Press, Boulder, CO, USA.

Tritton, D. J. (1988). *Physical fluid dynamics*. Oxford University Press, Oxford, England.

Van Sickle, J. and Gregory, S. (1990). Modeling inputs of large woody debris to streams from falling trees. *Canadian Journal of Forest Research*, 20:1593–1601.

Wallerstein, N., Alonso, C., Bennett, S., and Thorne, C. (2001). Distorted Froude-scaled flume analysis of large woody debris. *Earth Surface Processes and Landforms*, 26:1265–1283.

Wilcox, A. and Wohl, E. (2006). Flow resistance dynamics in step-pool stream channels: 1. large woody debris and controls on total resistance. *Water Resources Research*, 42.

Wu, T., Wang, H., Chiou, J., Hsieh, S., Chen, C., Wang, C., and Chuang, M. (2014). Forensic diagnosis on flood-induced bridge failure. ii: Framework of quantitative assessment. *Journal of Performance of Constructed Facilities*, 28:85–95.

Young, W. J. (1991). Flume study of the hydraulic effects of large woody debris in lowland rivers. *Regulated rivers: research and management*, 6:203–211.

Zeman, J., Novák, J., Šejnoha, M., and Šejnoha, J. (2008). Pragmatic multi-scale and multi-physics analysis of charles bridge in prague. *Engineering Structures*, 30:3365–3376.